An Implementation and Configuration of Ground Based Synthetic Aperture Radar for Environmental Monitoring

	KARUNATHILAKE Amila Thilanka
	Tohoku University
	11301　17797
URL	http://hdl.handle.net/10097/00121912

PhD Dissertation

An Implementation and Configuration of Ground Based Synthetic Aperture Radar for Environmental Monitoring

（環境モニタリングのための地表設置型合成開口レーダの構成と設置）

Submitted to
Graduate School of Environmental Studies
Tohoku University
2017

by

Amila Thilanka Karunathilake

Supervised by
Prof. Dr. Motoyuki Sato

Dissertation Committee
Prof. Dr. Motoyuki Sato
Prof. Dr. Hiroshi Takahashi
Prof. Dr. Shunichi Koshimura
(International Research Institute of Disaster Science)
Prof. Dr. Masahiko Nishimoto
(Kumamoto University)

Abstract

Radar remote sensing technique gives accurate information for environmental monitoring. Unlike space born and air born remote sensing techniques, the Ground-Based Synthetic Aperture Radar (GB-SAR) can be identified as most sophisticated remote sensing technique which can deploy with higher spatial and temporal resolution. However, prior to the deployment of such remote sensing technique to monitor the terrain displacement phenomena, the technical feasibility assessment used as a prognosticate tool to uncover the strengths of the proposed technique by objectively and rationally. In this thesis, the applicability of GB-SAR as an early-warning system for landslide detection was informatively discussed. The effectiveness of Differential Interferometric SAR (DInSAR) technique used in GB-SAR has a higher correlation with the geography of the monitoring location. Therefore the system compatibility assessment gives the highly considerable result to select the most appropriate remote monitoring method and its realm, before any hardware deployment. In the preliminary context, a 3D model was created using LiDAR survey and expected locations for GB-SAR installation were testified. The 3D simulation was carried out to estimate the expected illumination from each of the proposed locations. Then the hardware configuration parameters such as platform height, radar LOS direction and view angle were estimated for the best-reflected power and the optimum ground illumination.

Unlike on flat terrain, the GB-SAR deployment in a mountainous area become challenging task due to continuous change of meteorological parameters such as atmospheric temperature, pressure and relative humidity. In this study, a new atmospheric phase compensation method was proposed based on the spatial modelling of the GB-SAR observation area. The proposed Two-Stage Semi-empirical algorithm (TSSA) for atmospheric artifacts removal is based on the statistical method, and no atmospheric pressure, temperature or humidity data were required for interferometric phase correction. Therefore TSSA can be used to enhance the applicability of GB-SAR system with a minimum number of background data and the real time monitoring. The system can be used to work as a stranded alone system for remote monitoring in a highly dynamic environment. Furthermore, the concept of coherence scatters estimation is one of the main topics in DInSAR monitoring process. It will guarantee the

reliability of displacement measurements estimated by the GB-SAR system. The coherent scatter selection in a complicated urban environment, such as construction site which highly correlated with random movements of man and unmanned vehicle is challenging task. In this study, the new criteria for CS estimation was proposed based on eigenvector and eigenvalue analysis of 3 x 3 coherency T3 matrix. The eigenvector of coherency matrix accounts the basis invariant description of the scatterer with a specific scattering process and the eigenvalue used to estimate their relative magnitudes. They are further parameterized by pseudo-probabilities to estimate polarimetric entropy and alpha angle. The CS points were selected by the most stable scatter characteristics presented in a minimum number of data acquisitions.

The GB-SAR operation for real time monitoring becomes newly growing technique which can be used as an early warning system for stability estimation, in order to prevent landslide disasters. In this study, automatic landslide monitoring system and early warning system was developed and tested during the recent 6 months of period. The experimental site was located 3 km distance from the Aso volcanic mountain. The above-developed models and systems were validated by the real campaign in the mountainous environment of road reconstruction site in Minami-Aso, Kumamoto, Japan where the large scale landslide triggered after the Kumamoto earthquake in 2016.

Contents

List of Figures

11

13

List of Abbreviations

AOI	Area of interest
APS	Atmospheric phase screen
CS	Coherent scatters
DInSAR	Differential interferometric synthetic aperture radar
FMCW	Frequency modulated continuous wave
GB-SAR	Ground based synthetic aperture radar
GIS	Geographical information system
LiDAR	Light detection and ranging
LOS	Line of Site
PRF	Pulse repletion frequency
PRI	Pulse repletion interval
PS	Persistent scatters
RAR	Real aperture radar
RCS	Radar cross section
SAR	Synthetic aperture radar

Chapter 1 Introduction and Motivation

1.1 Background

1.11 Radar remote sensing for Environmental monitoring

Radar remote sensing is an active remote sensing technique which gives accurate information for environmental monitoring. The electromagnetics signal emitted by the radar sensor provides a different and unique view of the target by its physical properties [1]. In 1951, Carl Wiley of Goodyear Aerospace proposed the concept of synthetic aperture radar (SAR) that can provide higher-spatial resolution 2D radar images of the terrestrial surface [2]. These characteristics tend to widely spread the radar remote sensing technique as an environmental monitoring tool in varies scientific application. According to the sensor operation platforms, the remote sensing method can be categorized into Space-born, Air-borne [3] and ground-based [4]. The space-borne sensors and air-born sensors could potentially be a very powerful monitoring tool, able to observe very large area. However, due to limitations in spatial resolution, long revisit time, geometrical artifacts, and lack of coherence between two passages of the satellite sensor tend to develop a more sophisticate remote sensing technique for environmental monitoring [3][5]-[7].

1.12 Ground based SAR

GB-SAR is a relatively new remote sensing technique which has been developed extensively as a potential method of environmental monitoring [4][8]-[21]. The first GB-SAR systems were operated by VNA based [8][11] and later enhance as a complete stand-alone system for field operation. Unlike space born and air born remote sensing techniques, ground based synthetic aperture radar (GB-SAR) system become more popular due to the following limitations discuss in the literature,

- Acquisition geometry: the typical incidence angle and the orbital trajectory allow an acceptable sensitivity to vertical and across-azimuth (approximately east–west) displacement components only;
- Geometrical distortions: SAR images are intrinsically affected by perspective deformations (foreshortening, layover, shadowing) strongly limiting the observation of landslides on steep slopes or into narrow valleys; these limitations can only be partially removed by processing both ascending and descending data acquisitions;
- Spatial resolution: the resolutions of available satellites now higher compare to the GB-SAR; in any case, these resolutions are suitable only for large-scale slope movements;

➢ Temporal decorrelation: changes in the observed area usually degrade the quality of the interferogram and can prevent the application of the technique. This is usually the case of densely vegetated areas where sliding phenomena often occur; in general, the loss of coherence is related to the time span between the acquisitions. But GB-SAR can complete a single scan less than 10s, in order to have high interferometric coherence;

➢ Flexibility for quick deployment: The system can deploy according to user specified location and estimated parameters, in order to have better illumination from the AOI

Essentially, GB-SAR operates in the same manner as air- and space- borne microwave remote sensing, i.e., the synthetic aperture is obtained by scanning the antenna along a horizontal rail, placed orthogonally with respect to the line of sight direction. The obtained images have both amplitude and phase information. The complex product point-by-point, of a pair of images taken at different moments in time, give interferograms. A phased shift of a pixel in the interferograms is related to a displacement of the imaged point. This complete measuring process takes much less time than do other techniques to conduct measurements over a widespread area at a higher spatial resolution. Furthermore, the interferometric technique can be applied by repeatedly performing the scanning in order to detect very small changes in the rage of visibility. The GB-SAR technique has reportedly been successfully applied to a large number of fields in order to demonstrate its effectiveness. The displacement monitoring such as glacier [12], landslide [13]-[15], Volcano [16], Open-pit quarries [17], Mine-walls [18], Post-disaster area [19], Urban area [20], vibration monitoring [21][22] are few of them. The monitoring of landslide [4][9]-[15] is one of the most popular application in GB-SAR. Generally, ground surface monitoring techniques provide information on a determined number of points within the landslide area, both in the cases of geotechnical monitoring (clinometers, extensometers, etc.) and of GPS or conventional topographic survey [27]. Even if single-point data are accurate and taken particularly in significant areas (landslide crown, depletion zone, accumulation zone, etc.), they cannot be considered inferable to the whole landslide area. This is particularly important in large-size landslides or complex slope movements, which are characterized by different movement patterns. To get rid of such a strongly limiting characteristic, the topographic and/or instrumental measurements are usually carried out on extensive and complex monitoring networks. Nevertheless, these conventional monitoring techniques cannot give a detailed spatially extensive information and cannot be employed for those landslide sectors which are at high risk or not accessible. In GB-SAR system can render 2D wide area displacement map within a short period of time with sub-millimeter level accuracy. Therefore it can be identified as most appropriate remote sensing technique in the field of landslide monitoring. Moreover, the detection of the displacement in large stretchers such as dams

[22][23], dyke failures [24], bridges [25][24], or building in an urban and suburban environment [28][29] show realistic information which highly required for many civil engineering applications. In the natural environment, GB-SAR has also been used to monitor snow cover, snow avalanches, and glaciers as well as volcanic defamation. In addition, by using cross-track interferometry and polarimetric technique, the compatibility of the technique has been illustrated to create digital terrain maps (DTMs) [30]-[32], to map soil moisture distribution, and to monitor vegetation [3].

The use of a ground-based radar allows us to overcome most of the limits linked to space borne interferometry to overcome and provide the necessary flexibility in order to accomplish the extreme variability, in terms of size, a movement mechanism, displacement rate, state and distribution of activity, which intrinsically characterizes slope processes. In fact, such an approach makes possible to change the observation parameters in order to adapt them to every particular case. On the other hand, a ground-based system suffers from different limitations, such as the possibility to cover only areas of limited extension and the necessity of a location having a suitable visibility of the area under test. This will adversely affect the received data quality and efficiency of the equipment.

1.2 Research objective

As we have reviewed in above, GB-SAR has shown necessary flexibility to overcome most of the limits linked to other remote sensing techniques which have been used for environmental monitoring. However, due to the topographical irregularities of installation location, the system cannot measures obligatory area as expected. It will adversely affect the received data quality and efficiency of the equipment. Currently, there are not so many researchers that focus on optimization of sensor performance by considering terrestrial information in order to overcome those critical problems and limitations in GB-SAR monitoring. In this research work, we mainly focus on most realistic methodologies and model based approaches to overcome above practical limitations of GB-SAR system in order to find the most appropriate solution to improve the applicability of GB-SAR for environmental monitoring. It will fill the gap between the theoretical explanation of the EM wave propagation and experimental results obtain from the practical deployment.

Prior to the deployment of any remote monitoring technique for the terrain displacement phenomena, technical feasibility assessment methods can be used as a prognosticate tool to uncover the strengths of the proposed technique by objectively and rationally. So far, most of the GB-SAR monitoring experiment was carried out by universities and institution which highly specialized in the field of electrical engineering and so on. There is no literature can be found in any repositories which combined this highly technical experiment with the geospatial information for illumination estimation which

enhance the GB-SAR monitoring process. One of our goal is to combine those two research fields in an appropriate way to conduct successful GB-SAR monitoring campaign in future.

Secondly, the reliability of displacement measurement by DInSAR techniques is highly correlated with amplitude and the phase information of reflected EM wave and homogeneity of the propagation medium. There are many research work carried out since 1950, to model the atmospheric delay during the wave propagation. These models based on the assumption of atmospheric homogeneity and derived from the ideal gas equation, so that meteorological parameters are mandatory, can use for post-processing for DInSAR. But practically, the homogeneity of the propagation medium is no longer preserve due to extreme weather condition, especially in GB-SAR observation in a mountainous area. The investigation of appropriate atmospheric correction method for real time GB-SAR monitoring process is one of our goal to be achieved.

Coherent scatter (CS) estimation is another main subject in GB-SAR displacement monitoring processes. It will guaranty the reliability of displacement measurements. There are many CS estimation method proposed in the past, but necessary to have a large number of datasets, not so accurate for the suburban environment, unstable in far field observation due to loss of energy in EM signal. Today, most of the latest GB-SAR sensors facilitated obtained fully polarimetric data sets in single scanning period. This can further utilize to estimate the CS locations in a complicated urban environment such as construction site which highly correlated with random movements.

GB-SAR shows a wide range of application, but those experimental results and discussion become limited among scientist and engineers who already have preliminary knowledge and experience in the field of their specialities. This will not be sufficient enough to overcome the future challenges in disaster prevention and mitigation. Therefore, we hope the establishment of an understandable and user-friendly monitoring system for GB-SAR data interpretation will complete the total environmental monitoring process for disaster prevention in future.

1.3 Thesis structure

```
┌─────────────────────────────┐
│         Chapter 1:          │
│   Introduction and Motivation │
└─────────────────────────────┘
              │
              ▼
┌─────────────────────────────┐
│ Chapter 2: Polarimetric calibration │
│          for GB-SAR          │
└─────────────────────────────┘
```

Chapter 3	Chapter 5
3D GIS model design for GB-SAR illumination	Eigenvector and Eigenvalue based method for coherent scatter (CS) selection using radar polarimetry

```
                          ┌─────────────────────────────┐
                          │          Chapter 4          │
                          │ Development of empirical model │
                          │  for atmospheric phase screen  │
                          │          reduction           │
                          └─────────────────────────────┘
```

┌───┐
│   Chapter 6   │
│   GB-SAR configuration for near real-time   │
│ landslide monitoring and early warning system │
└───┘

┌───┐
│   Chapter 7   │
│   Feasibility study of   │
│   GB-SAR implementation in Sri Lanka   │
└───┘

┌───┐
│   Chapter 8   │
│   Conclusion and Perspective   │
└───┘

Figure 1.1 Structure of the thesis

1.4 References

[1] F. T. Ulaby et al., Microwave radar and radiometric remote sensing, The University of Michigan Press, 2014.

[2] I. G. Cumming and F. H. Wong, *Digital Processing of Synthetic Aperture Radar Data: Algorithms and Implementation*, Artech House, Boston, London, 2005.

[3] J. S. Lee and E. Pottier, Polarimetric Radar Imaging: From Basics to Applications, Boca Raton, US: CRC Press, 2009.

[4] M. Pieraccini, N. Casagli, G. Luzi, D. Tarchi, D. Mecatti, L. Noferini and C. Atzeni (2003) Landslide monitoring by ground-based radar interferometry: A field test in Valdarno (Italy), International Journal of Remote Sensing, 24:6, 1385-1391, DOI: 10.1080/0143116021000044869

[5] L. Ferro-Famil, A. Reigber, E. Pottier and W. M. Boerner, "Scene characterization using subapetur polarimetric SAR data," IEEE Trans. Geosci. Remote Sens., vol. 41, no. 10, pp 2264-2276, May 2003.

[6] J.S. Lee, D.L. Schuler and T. L. Ainworth, "Polarimetric SAR data compensation for terrain azimuth slope variation," IEEE Trans. Geosci. Remote Sens., vol. 38, no. 5, pp 2153-2163, September 2000.

[7] R. Sabry, "Terrain and surface modeling using polarimatric SAR data features," IEEE Trans. Geosci. Remote Sens., vol. 54, no. 02, pp 1170-1184, February 2016.

[8] Zheng-Shu Zhou and Motoyuki Sato, "Ground-based polarimetric SAR systems for environment studies," IEEE Antennas and Propagation Society International Symposium. Digest. Held in conjunction with: USNC/CNC/URSI North American Radio Sci. Meeting (Cat. No.03CH37450), Columbus, OH, USA, 2003, pp. 202-205 vol.1.

[9] G. Antonello, N. Casagli, P. Farina, G.Nico, A.J. Sieber and D. Tarchi, "Ground-based SAR interferometry for monitoring mass movement," Springer-Verlag, Landslides 1:21-28, February 2004

[10] G. Luzi, M. Pieraccini, D. Mecatti, L. Noferini, G. Guidi, F. Moia and Carlo Atzeni, "Ground-based radar interferometry for landslides monitoring: Atmospheric and instrumental decorrelation source on experimental data," IEEE Trans. Geosci. Remote Sens., vol. 42, no. 11, pp 2454-2466, November 2004.

[11] M. Sato, Z.S. Zhou, T. Hamasaki, and W.M. Boerner, "Development of a ground-based synthetic aperture radar (GB-SAR) system and its application to environmental monitoring and disaster prevention," Proc. of the POLinSAR 2005 Workshop, 17-21 January 2005, ESRIN, Frascati, Italy, ESA SP-586, May 2005

[12] G. Luzi et al., "Monitoring of an Alpine Glacier by Means of Ground-Based SAR Interferometry," in IEEE Geoscience and Remote Sensing Letters, vol. 4, no. 3, pp. 495-499, July 2007.

[13] L. Noferini, M. Pieraccini, D. Mecatti, G. Macaluso, C. Atzeni, M. Mantovani, G. Marcato, A. Pasuto, S. Silvano, F. Tagliavini, Using GB-SAR technique to monitor slow moving landslide, Engineering Geology, Volume 95, Issue 3, 2007, Pages 88-98, ISSN 0013-7952,

[14] M. Matsumoto, K. Takahashi and M. Sato, "Long-term landslide monitoring by GB-SAR interferometry in Kurihara, Japan," Conference Proceedings of 2013 Asia-Pacific Conference on Synthetic Aperture Radar (APSAR), Tsukuba, 2013, pp. 529-532.

[15] L. Zou, K. Takahashi and M. Sato, "Displacement measurement and monitoring with ground-based SAR; case study at Aratozawa," 2014 Asia-Pacific Microwave Conference, Sendai, Japan, 2014, pp. 1022-1024.

[16] L. Noferini, D. Mecatti, G. Macaluso, M. Pieraccini, C. Atzeni and M. Ripepe, "A high speed microwave interferometer used for monitoring Stromboli volcano," 2009 IEEE International Geoscience and Remote Sensing Symposium, Cape Town, 2009, pp. I-124-I-127.

[17] D. Mecatti, G. Macaluso, A. Barucci, L. Noferini, M. Pieraccini and C. Atzeni, "Monitoring open-pit quarries by interferometric radar for safety purposes," The 7th European Radar Conference, Paris, 2010, pp. 37-40.

[18] P. Farina, N. Coli, R. Yön, G. Eken and H. Ketizmen, "Efficient real time stability monitoring of mine walls: The Çöllolar Mine case study," 23rd Int. Mining Congr. Exhib. Turkey, 2013

[19] K. Takahashi, M. Matsumoto and M. Sato, "Continuous Observation of Natural-Disaster-Affected Areas Using Ground-Based SAR Interferometry," in IEEE Journal of Selected Topics in Applied Earth Observations and Remote Sensing, vol. 6, no. 3, pp. 1286-1294, June 2013.

[20] L. Pipia, X. Fabregas, A. Aguasca, S. Duque, J. J. Mallorqui and C. Lopez-Martinez, "Polarimetric Deformation Maps Retrieval of Urban Areas using Ground-Based SAR Acquisitions," IGARSS 2008 - 2008 IEEE International Geoscience and Remote Sensing Symposium, Boston, MA, 2008, pp. IV - 327-IV - 330.

[21] Y. Liu et al., "Ground-based synthetic aperture radar for vibration and deformation monitoring in China," IET International Radar Conference 2015, Hangzhou, 2015, pp. 1-5.

[22] M. Voege, R. Frauenfelder and Y. Larsen, "Displacement monitoring at Svartevatn dam with interferometric SAR," 2012 IEEE International Geoscience and Remote Sensing Symposium, Munich, 2012, pp. 3895-3898,

[23] Y. Liu, C. Lee, H. Yong, L. Jia, W. Youshi, S. Placidi, S. Roedelsperger, "FastGBSAR case studies in China: Monitoring of a dam and instable slope," 2015 IEEE 5th Asia-Pacific Conference on Synthetic Aperture Radar (APSAR), Singapore, 2015, pp. 849-852.

[24] S. Roedelsperger, A. Coccia, D. Vicente, C. Trampuz and A. Meta, "The novel FastGBSAR sensor: Deformation monitoring for dike failure prediction," Conference Proceedings of 2013 Asia-Pacific Conference on Synthetic Aperture Radar (APSAR), Tsukuba, 2013, pp. 420-423.

[25] M. Pieraccini, M. Fratini, F. Parrini and C. Atzeni, "Dynamic Monitoring of Bridges Using a High-Speed Coherent Radar," in IEEE Transactions on Geoscience and Remote Sensing, vol. 44, no. 11, pp. 3284-3288, Nov. 2006.

[26] S. Placidi, A. Meta, L. Testa and S. Rödelsperger, "Monitoring structures with FastGBSAR," 2015 IEEE Radar Conference, Johannesburg, 2015, pp. 435-439.

[27] J. Gunathilake, Y. Iwao and T. Yamasaki, "Relationship of the faulting to the creep movement of Iwakura landslide in Saga, Japan," Landslides- Journel of Japan Landslide Society., vol.39, no. 2, pp 212-223, 2002.

[28] S. Roedelsperger, M. Becker, C. Gerstenecker and G. Laeufer, "Near real-time monitoring of displacements with the ground based sar ibis-l," Proc. Fringe 2009 Workshop, Frascati, Italy, 30 November-4 December 2009 (ESA SP-677, March 2010),

[29] E. Yigit *et al*., "Millimeter-wave ground based synthetic aperture radar measurements," *2011 URSI General Assembly and Scientific Symposium*, Istanbul, 2011, pp. 1-4.

[30] G. Nico, D. Leva, G. Antonello and D. Tarchi, "Ground-based SAR interferometry for terrain mapping: theory and sensitivity analysis," in IEEE Transactions on Geoscience and Remote Sensing, vol. 42, no. 6, pp. 1344-1350, June 2004.

[31] L. Noferini, M. Pieraccini, D. Mecatti, G. Macaluso, G. Luzi and C. Atzeni, "DEM by Ground-Based SAR Interferometry," in IEEE Geoscience and Remote Sensing Letters, vol. 4, no. 4, pp. 659-663, Oct. 2007.

[32] M. Pieraccini, L. Noferini, D. Mecatti, G. Macaluso, G. Luzi and C. Atzeni, "Digital elevation models by a GBSAR interferometer for monitoring glaciers: the case study of Belvedere Glacier," IGARSS 2008 - 2008 IEEE International Geoscience and Remote Sensing Symposium, Boston, MA, 2008, pp. IV - 1061-IV - 1064.

Chapter 2 Polarimetric calibration for GB-SAR

In a fully polarimetric measurement, systematic errors can arise in a transmitter and a receiver antenna due to misalignment of the antenna. These errors make additional constant values to the expected scattering matrix for a stranded target. Therefore we need a fully polarimetric calibration in order to acquire the stranded scattering matrix. This chapter describes the GB-SAR technical parameter specification and operating principal, liner polarimetric SAR, complete system calibration and the validation done in Tohoku University, Kawauchi campus, outdoor environment.

2.1 Principals of GB-SAR

2.1.1 System principle
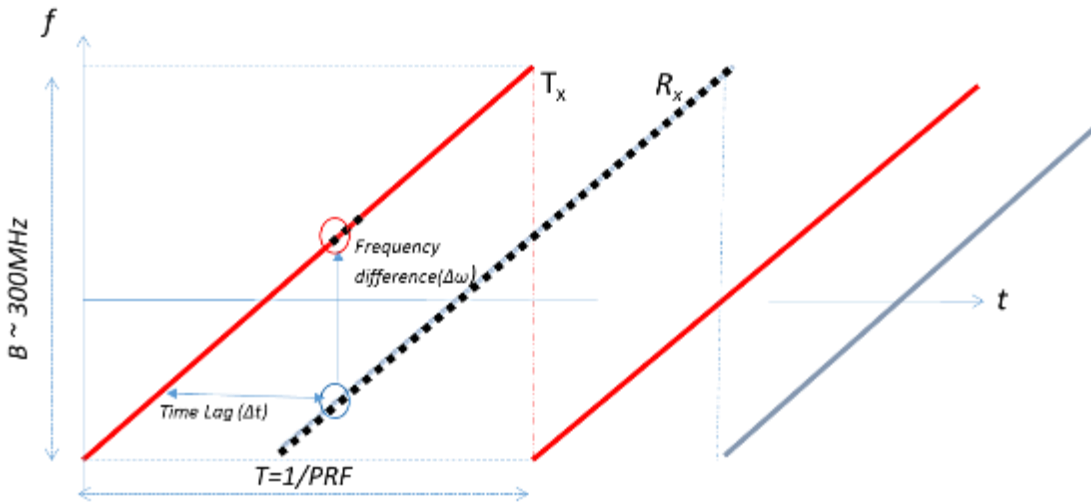
Figure 2.2 FMCW chirp signal

The long range detection and fine range resolution are the main conspicuous challenges in a radar system which developed for environmental monitoring. But there are practical limits on the level of peak power. In order to obtain long detection ranges at pulse repletion frequency (PRF) low enough for pulse delay ranging, fairly wide pulses must be transmitted. One of the solution for this predicament pulse compression. That is, transmit internally modulated pulses of sufficient width to provide the necessary average power at a reasonable level of peak power; then, compress the received echoes by decoding their modulation [1].

The linear frequency modulation is one of common method resolve above challenge. Since this action is parallel to the chirping of a bird, this method of coding was called "chirp" by its inventors. In this method, the radio frequency of each transmitted pulse is increased at a constant rate though its bandwidth. So that the every echo, naturally has the same increase in frequency. Each successive transmitted pulse thus has a slightly higher radio frequency. The linear modulation is continued for a

period at least several times as long as the round-trip transit time for the most distant target of significance. Over the course of this period, the instantaneous difference between the frequency of the received echoes and the frequency of the transmitter is measured. The transmitter is then returned to the starting frequency, and the cycle is repeated. This operational radar name as frequency modulated continuous wave (FMCW). The radar sensor of the GB-SAR system subjected in this thesis operates in this principle [2][3].

2.1.2 System parameters

The radar unit of the GB-SAR system operates as FMCW radar. The system constant parameters are listed in below table 1.

<div align="center">TABLE 1. GB-SAR TECHNICAL PARAMETERS</div>

System Parameters	Symbol	Magnitude
Center Frequency	f_c	17.2 GHz
Sampling Frequency	f_s	1 MHz
Bandwidth	B_{max}	300 MHz
Rail length	L	1.8 m
Maximum rail velocity	v_{max}	0.5 m/s
Maximum range	Ru_{max}	4 km
Speed of light	c	299 792 458 m/s

The radar unit transmits a frequency modulated signal with center frequency f_c and bandwidth B. The center wavelength λ_c of the signal is derived by,

$$\lambda_c = {}^c\!/_{f_c} \tag{2.1}$$

This signal is reflected at an object, received by the radar antenna and mixed with the originally transmitted signal [4] to obtain the beat signal (Figure 2.2). The frequency f_b of the beat signal is proportional to the delay τ of transmitted and received signal and therefor proportional to the range r between radar unit and object,

$$f_b = q\tau = {}^{2q}\!/_c \cdot r \tag{2.2}$$

where q is the ratio of transmitted bandwidth B_{max} to the duration of the sweep PRI,

$$q = {}^{B_{max}}\!/_{PRI} \tag{2.3}$$

2.1.3 System operation mode

Real Aperture Radar (RAR)
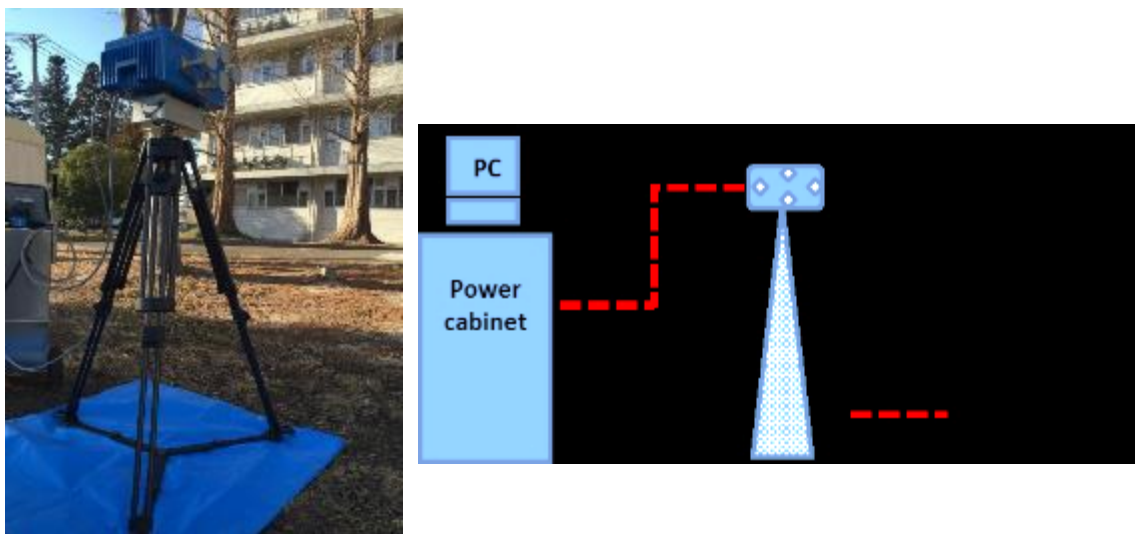
Figure 2.3 GB-SAR in Real Aperture Radar mode

Synth Aperture Radar (RAR)
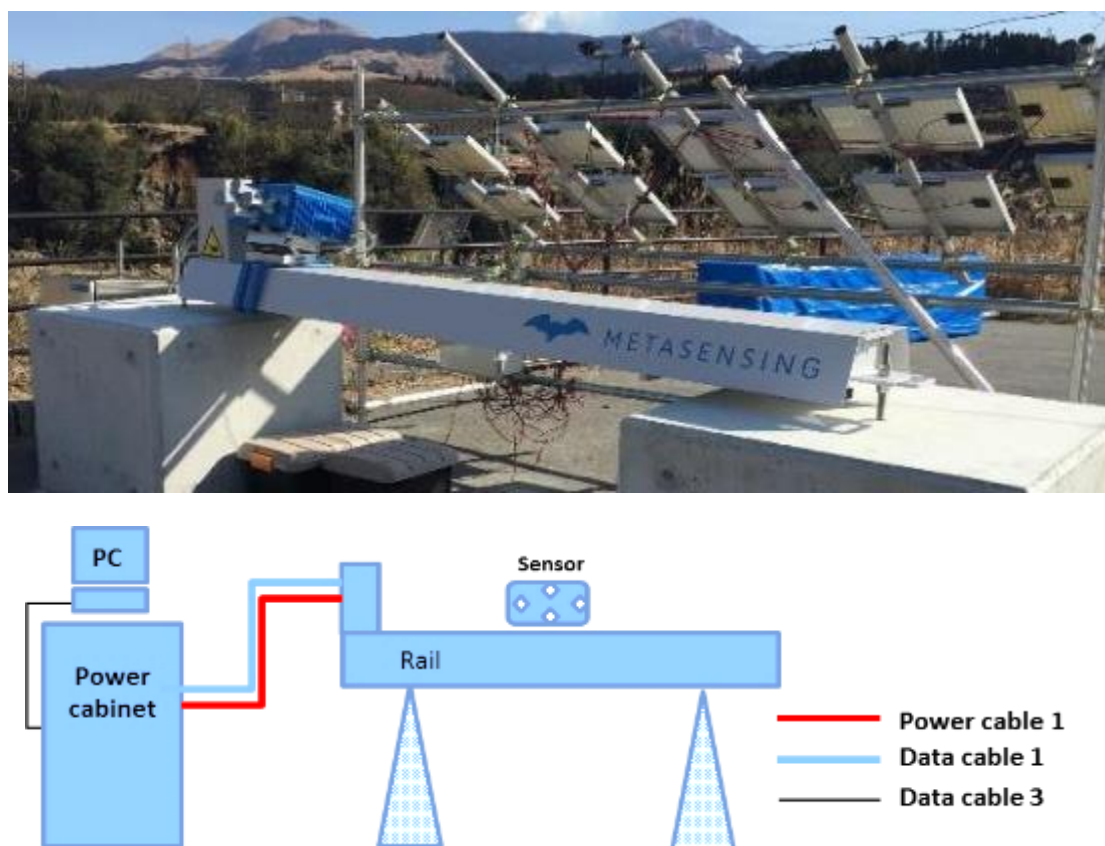
Figure 2.4 GB-SAR in Synth Aperture Radar mode

2.2 SAR polarimetry

In polarimetric SAR systems are designed to transmit microwave radiation of orthogonal polarization pairs, for example, that is either horizontally polarized (H) or vertically polarized (V). A transmitted wave of either polarization can generate a backscattered wave with a variety of polarizations. It is the analysis of these pairs of orthogonal transmitting and receiving polarization combinations that constitute the science of radar polarimetry [5].

Any polarization on either transmission or reception can be synthesized by using H and V components with a well-defined relationship between them shown in Figure 2.5. For reasons based on the design of polarization switches, and so on, systems that transmit and receive both of these linear polarizations are commonly used. With these radars, there can be four combinations of transmitting and receive polarizations:

(a) HH – for horizontal transmit and horizontal receive,

(b) VV – for vertical transmit and vertical receive,

(c) HV – for vertical transmit and horizontal receive,

(d) VH – for horizontal transmit and vertical receive.

The first two polarization combinations are referred as "co-polarized" because the transmitting and receiving polarizations are the same. The last two combinations are referred as "cross-polarized" because the transmitting and receiving polarizations are orthogonal signal to one another [6].
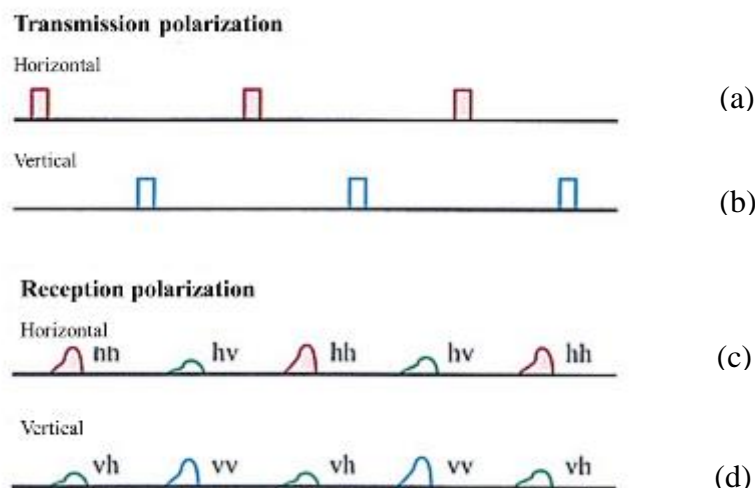
Figure 2.5 Transmit and recevved signal clasification in radar polarimetry (a) H (b) V transmit , (c) and (d) are received signal [6]

29

In the model explained in Figure 2.5 (a) and (b), the H and V polarized orthogonal signal was transmitted by the GB-SAR sensor and Figure (c) and (d) depict the back scatted signal with four (quad) polarimetric combinations. The preliminary description of how a radar target or surface feature scatters electromagnetic energy can be expressed in term of the scattering matrix. A polarimetric GB-SAR can be used to determine the target response or scattering matrix using this two orthogonal polarizations, typically linear H and linear V, which generally represent as X polarization and Y polarization on each of transmitter and receiver, respectively [5].

In a monostatic backscattering model, where the transmitting and receiving antenna area placed at the same location, the incident and scattered Jones vectors are expressed in the same orthogonal basis. By defining a local Cartesian basis $(\hat{x}, \hat{y})$ and for understanding, the unit vector $\hat{u}_H$ a horizontal unit vector with $\hat{u}_H = \hat{x}$ and the unit vector $\hat{u}_V$ a vertical unit vector with $\hat{u}_V = \hat{y}$. In the Cartesian $(\hat{x}, \hat{y})$ basis or in the horizontal-vertical $(\hat{u}_H, \hat{u}_V)$ basis, the 2 x 2 complex backscattering S matrix can be expressed as,

$$S_{(\hat{x},\hat{y})} = \begin{bmatrix} S_{XX} & S_{XY} \\ S_{YX} & S_{YY} \end{bmatrix} = S_{(\hat{u}_H,\hat{u}_V)} = \begin{bmatrix} S_{HH} & S_{HV} \\ S_{VH} & S_{VV} \end{bmatrix} \tag{2.4}$$

The element S_{HH} and S_{VV} produce the power return in the co-polarized channel and the element S_{HV} and S_{VH} produce the power return in the cross-polarized channels. If the role of the transmitting and the receiving antennas are interchanged, the reciprocity can apply for simplification. Then backscattering matrix be symmetric, with $S_{HV} = S_{VH}$ and the scattering matrix can be written as,

$$S_{(\hat{x},\hat{y})} = S_{(\hat{u}_H,\hat{u}_V)} = \begin{bmatrix} |S_{HH}|e^{j\varphi_{HH}} & |S_{HV}|e^{j\varphi_{HV}} \\ |S_{HV}|e^{j\varphi_{HV}} & |S_{VV}|e^{j\varphi_{VV}} \end{bmatrix} \tag{2.5}$$
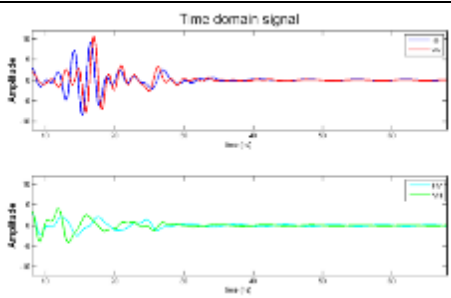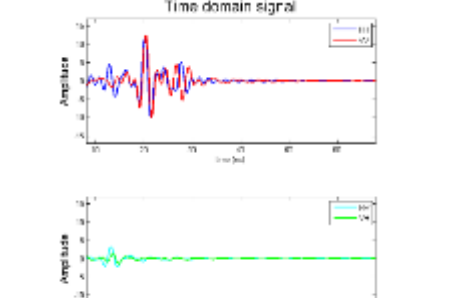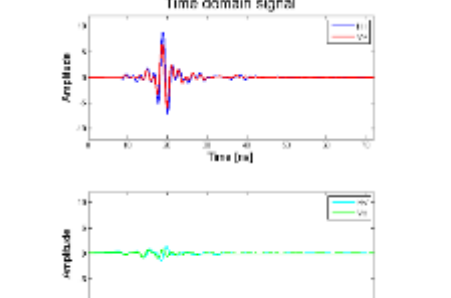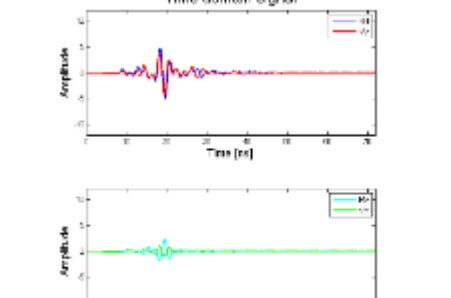
$$S_{(\hat{x},\hat{y})} = e^{j\varphi_{HH}} \begin{bmatrix} |S_{HH}| & |S_{HV}|e^{j(\varphi_{HV}-\varphi_{HH})} \\ |S_{HV}|e^{j(\varphi_{HV}-\varphi_{HH})} & |S_{VV}|e^{j(\varphi_{VV}-\varphi_{HH})} \end{bmatrix}$$

Absolute
phase term

Relative scattering matrix

$$\tag{2.6}$$

2.3 System calibration

2.3.1 Stranded reflectors and scattering observation

The scattering responds from the deterministic object always present a complex scattering response as a consequence of its complex geometrical structure [5][7]. In the other hand, this scattering respond will vary with the reflectivity properties of the target surface.

Table 2 Fully polarimatric Scattering respond observation for canonical target (Experiment in anechotic chamber, Tohoku university)		
Target	Image	Quad pol respond
Metal sphere $S = \begin{bmatrix} 1 & 0 \\ 0 & 1 \end{bmatrix}$		
Flat metal plate $S = \begin{bmatrix} 1 & 0 \\ 0 & 1 \end{bmatrix}$		
Dihedral corner reflector $S = \begin{bmatrix} \cos 2\varphi & \sin 2\varphi \\ \sin 2\varphi & -\cos 2\varphi 1 \end{bmatrix}$		
Metal wire $S = \begin{bmatrix} \cos^2\varphi & 1/2 \sin 2\varphi \\ 1/2 \sin 2\varphi & \sin^2\varphi \end{bmatrix}$		

2.3.2   Backscattering Model

In measuring a target scattering matrix, the received signals are determined not only by the desired target scattering matrix but also by the transmission and reception properties of the measurement system. A monostatic backscatter model is shown in Figure 2.6.
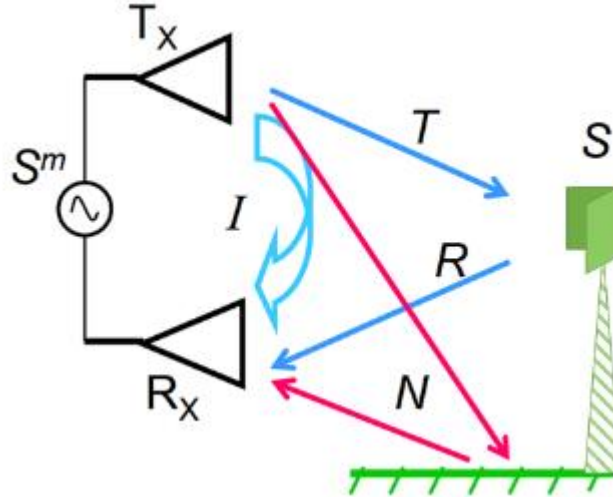
Figure 2.6 Backscattering model used for system calibration

Generally, the RCS of a target is polarization dependent [7]. For linear polarizations, a 2 x 2 scattering matrix is employed for full polarimetric description. Thereby the radar polarimetry backscattering matrix equation is given by,

$$S_M = [I] + [N] + Ae^{j\phi}[R][S][T] \tag{2.7}$$

$S_M - defined\ the\ measured\ data$

$[I] - transmitter\ and\ receiver\ antenna\ coupling$

$[N] - background\ noice\ and\ ground\ clutter$

$Ae^{j\varphi} - complex\ coefficient$

$[R] - normalized\ receiving\ channel\ factor$

$[S] - target\ theoretical\ scatering\ matrix$

$[T] - normalized\ transmitting\ factor$

An altered polarimetric RCS calibration technique using two orientations of the dihedral corner reflectors as calibration targets were used. This method is valid for any monostatic or quasi-monostatic radar system [8]. In this experiment, the scattering measurement of two orientations of calibration dihedral corner reflectors are considered. The frequency responses of four measurement channels are modelled as mutually independent and thus, no special care has to be taken for signal paths and nonreciprocal properties in a measurement system, the calibration procedure is simplified by taking advantage of small cross-polarized terms.

For monostatic back scattering case, $[M] = Ae^{j\varphi}[R][S][T]$

$$[S_M] = [S_T] \tag{2.8}$$

$$[S_M] - [I] - [N] = [M] \tag{2.9}$$

$$[M] = Ae^{j\varphi}[R][S][T] \tag{2.10}$$

Here, the M indicates the matrix after subtracting background noise and ground clutter. The direct coupling was removed by time gating. Further, an increase of the distance between ground to the sensor and distance between sensor to the target found as favorable factors for above assumptions. By considering the reciprocity due to monostatic case,

$$[R] = [T]^T \tag{2.11}$$

$$[R] = \begin{bmatrix} 1 & \Delta y \\ \Delta x & 1 \end{bmatrix} \text{ and } [T] = \begin{bmatrix} 1 & \Delta x \\ \Delta y & 1 \end{bmatrix} \tag{2.12}$$

Where Δx and Δy are the cross-calibration components, which account for the cross-polarization error in the target illumination. This matrix can be rewritten as,

$$\begin{bmatrix} M_{hh} & M_{hv} \\ M_{vh} & M_{vv} \end{bmatrix} = Ae^{j\varphi} \begin{bmatrix} 1 & \Delta y \\ \Delta x & 1 \end{bmatrix} \begin{bmatrix} S_{hh} & S_{hv} \\ S_{vh} & S_{vv} \end{bmatrix} \begin{bmatrix} 1 & \Delta x \\ \Delta y & 1 \end{bmatrix} \tag{2.13}$$

$$\begin{bmatrix} M_{hh}C_{hh} & M_{hv}C_{hv} \\ M_{vh}C_{vh} & M_{vv}C_{vv} \end{bmatrix} = \begin{bmatrix} 1 & \Delta y \\ \Delta x & 1 \end{bmatrix} \begin{bmatrix} S_{hh} & S_{hv} \\ S_{vh} & S_{vv} \end{bmatrix} \begin{bmatrix} 1 & \Delta x \\ \Delta y & 1 \end{bmatrix} \tag{2.14}$$

Where $[C]$ is reciprocal of $Ae^{j\varphi}$

$$M_{hh} = C_{hh}^{-1}\left(S_{hh} + \Delta y S_{vh} + S_{hv}\Delta y + \Delta y S_{vv}\Delta y\right) \tag{2.15}$$

$$M_{vh} = C_{vh}^{-1}\left(S_{hh} + \Delta y S_{vh} + S_{hv}\Delta y + \Delta y S_{vv}\Delta y\right) \tag{2.16}$$

$$M_{hv} = C_{hv}^{-1}\left(S_{hh} + \Delta y S_{vh} + S_{hv}\Delta y + \Delta y S_{vv}\Delta y\right) \tag{2.17}$$

$$M_{vv} = C_{vv}^{-1}\left(S_{hh} + \Delta y S_{vh} + S_{hv}\Delta y + \Delta y S_{vv}\Delta y\right) \tag{2.18}$$

The theoretical scattering matrices for dihedral corner reflector in 0 degrees and 45 degrees can be represented as,

$$\left[S^{(1)}\right] = \begin{bmatrix} S_{hh}^{(1)} & S_{hv}^{(1)} \\ S_{vh}^{(1)} & S_{vv}^{(1)} \end{bmatrix} \quad \text{for 0 degrees dihedral} \tag{2.19}$$

$$\left[S^{(2)}\right] = \begin{bmatrix} S_{hh}^{(2)} & S_{hv}^{(2)} \\ S_{vh}^{(2)} & S_{vv}^{(2)} \end{bmatrix} \quad \text{for 45 degrees dihedral} \tag{2.20}$$

By assumption of two delta terms neglected and of the reciprocity theorem for a monostatic system,

$$S_{hv}^{(1)} = S_{hv}^{(1)} = 0 \quad \text{and} \tag{2.21}$$

$$S_{hv}^{(1)} = S_{hv}^{(1)} = 0 \tag{2.22}$$

Substituting both of measured and theoretical values of the 0-degree dihedral,

$$C_{hh} = \frac{S_{hh}^{(1)}}{M_{hh}^{(1)}} \quad \text{and} \quad C_{vv} = \frac{S_{vv}^{(1)}}{M_{vv}^{(1)}} \tag{2.23}$$

$$C_{hh}M_{hh}^{(2)} = S_{hh}^{(2)} + \Delta y S_{hv}^{(2)} + \Delta y S_{vh}^{(2)} \tag{2.24}$$

$$C_{vv}M_{vv}^{(2)} = \Delta x S_{hv}^{(2)} + \Delta x S_{vh}^{(2)} + S_{vv}^{(2)} \tag{2.25}$$

Thereby cross calibration coefficients can be evaluated as,

$$\Delta y = \frac{C_{hh}M_{hh}^{(2)} - S_{hh}^{(2)}}{2S_{vh}^{(2)}} \quad \text{and} \quad \Delta x = \frac{C_{vv}M_{vv}^{(2)} - S_{vv}^{(2)}}{2S_{vh}^{(2)}} \tag{2.26}$$

$$C_{vh} = M_{vh}^{(2)^{-1}}\left(\Delta x S_{hh}^{(2)} + S_{vh}^{(2)} + \Delta y S_{vv}^{(2)}\right) \tag{2.28}$$

$$C_{vh} = M_{hv}^{(2)^{-1}}\left(\Delta x S_{hh}^{(2)} + S_{vh}^{(2)} + \Delta y S_{vv}^{(2)}\right) \tag{2.29}$$

Therefore, scattering matrix of an arbitrary target can be calculated by,

$$\begin{bmatrix} S_{hh} & S_{hv} \\ S_{vh} & S_{vv} \end{bmatrix} = \begin{bmatrix} 1 & \Delta y \\ \Delta x & 1 \end{bmatrix}^{-1} \begin{bmatrix} M_{hh}C_{hh} & M_{hv}C_{hv} \\ M_{vh}C_{vh} & M_{vv}C_{vv} \end{bmatrix} \begin{bmatrix} 1 & \Delta x \\ \Delta y & 1 \end{bmatrix}^{-1} \tag{2.30}$$

Calibration experiment

Figure 2.7 Experimental setup of GB-SAR calibration

The calibration experiment was carried out at Tohoku University, Kawauchi campus out door environment. The GB-SAR sensor was mounted in a very stable tripod with 1.5 m from the ground. The target was located 10 m distance from the sensor on completely flat terrain, in order to minimize unwanted reflection from the background and reduces the antenna coupling effect. The processing algorithms [9]-[15] were implemented in MATLAB [16]-[20] platform.
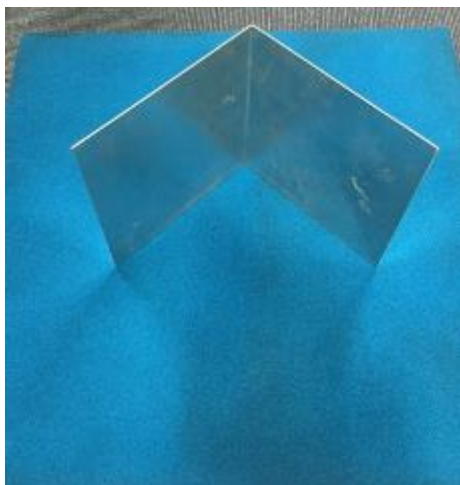
(a)
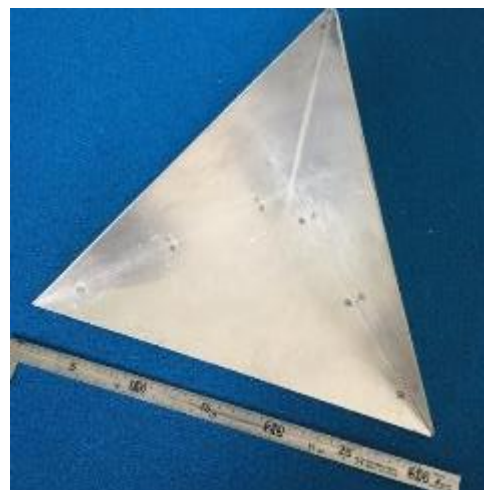
(b)

Figure 2.8 The calibration target (a) Metal dihedral corner reflector and target for experimental validation using (b) Metal Trihedral corner reflector

2.3.3 Calibration results

The Figure 2.9 depicts the raw beat signal obtained from the GB-SAR system.

(a)   (b)
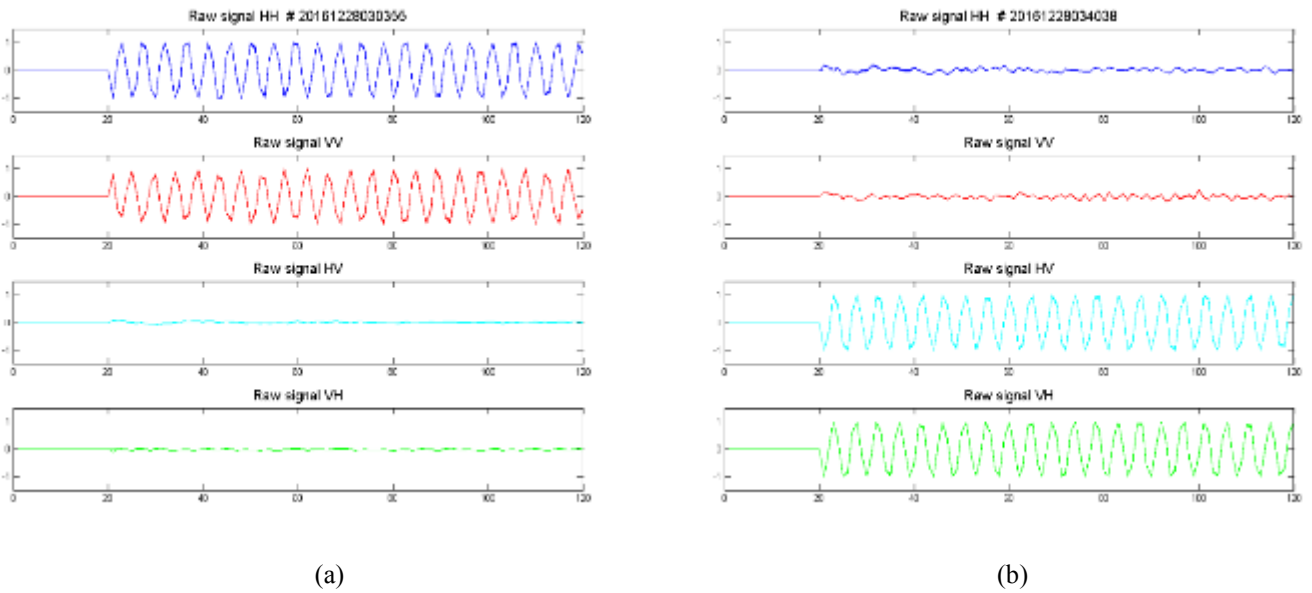
Figure 2.9 Beat signal received from (a) 0 degree dihedral corner reflector (b) 45 degree rotated dihedral corner reflector

After the Fourier transformation, time domain wave form was obtained and depicted in Figure 2.10,

(a)   (b)
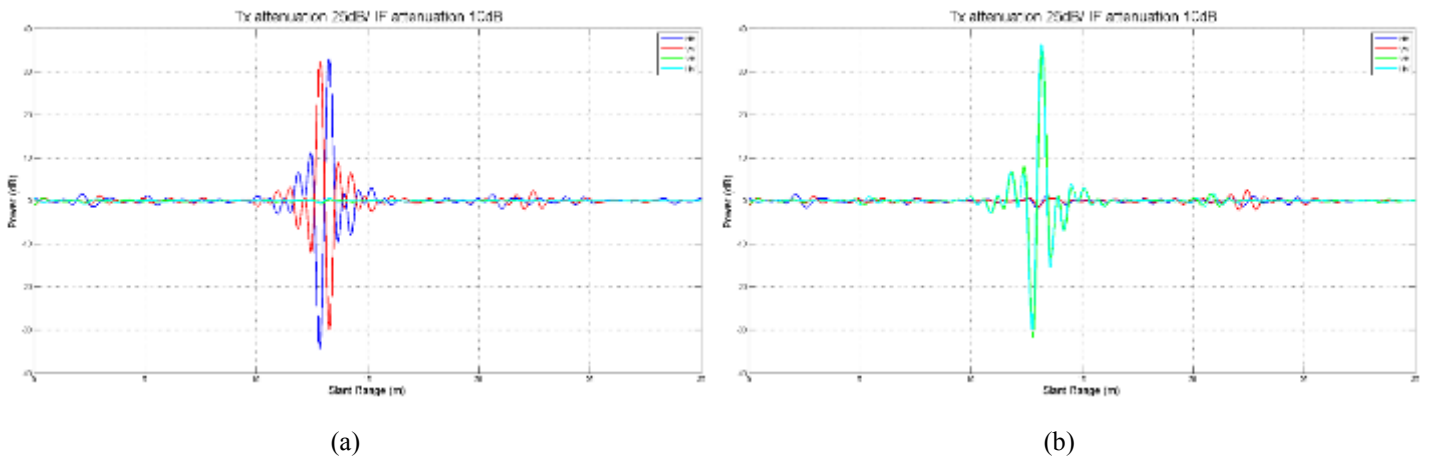
Figure 2.10 Signal wave from for (a) 0 degree dihedral corner reflector (b) 45 degree rotated dihedral corner reflector

We apply rectangular windowing function for time gate the time domain signal. The signal after time gating was depicted in Figure 2.11,

(a)   (b)
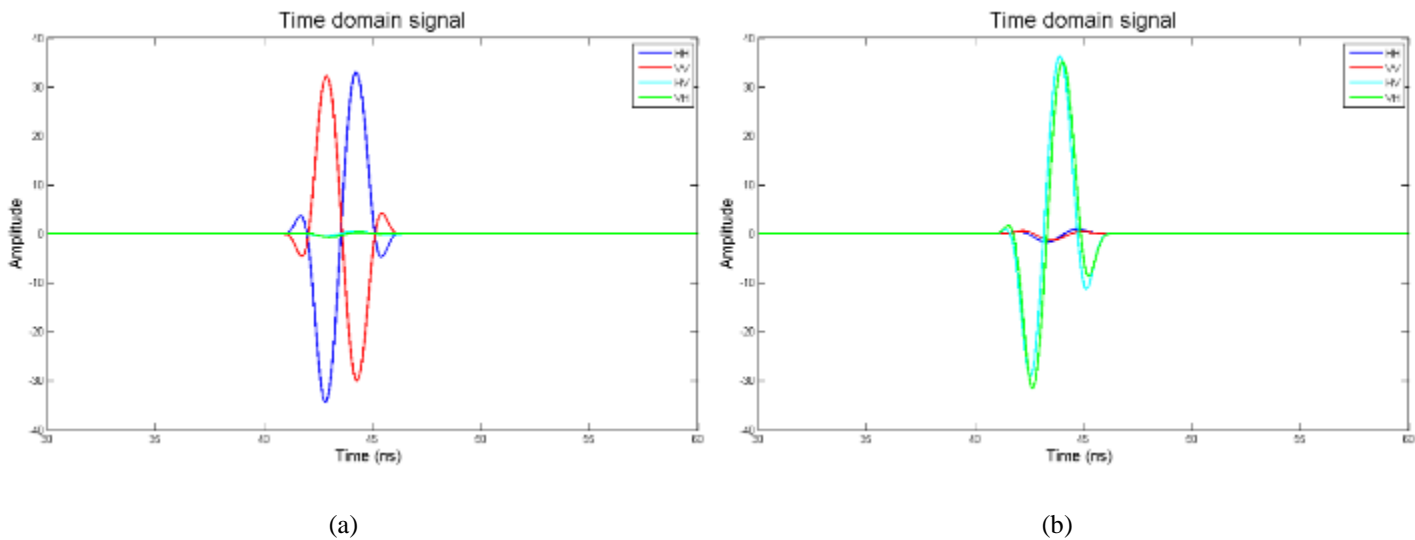
Figure 2.11 Time gated signal wave form (a) 0 degree dihedral corner reflector (b) 45 degree dihedral corner reflector

Then the resultant time domain signal was transformed into frequency domain and depicted in the Figure 2.12,

(a)   (b)
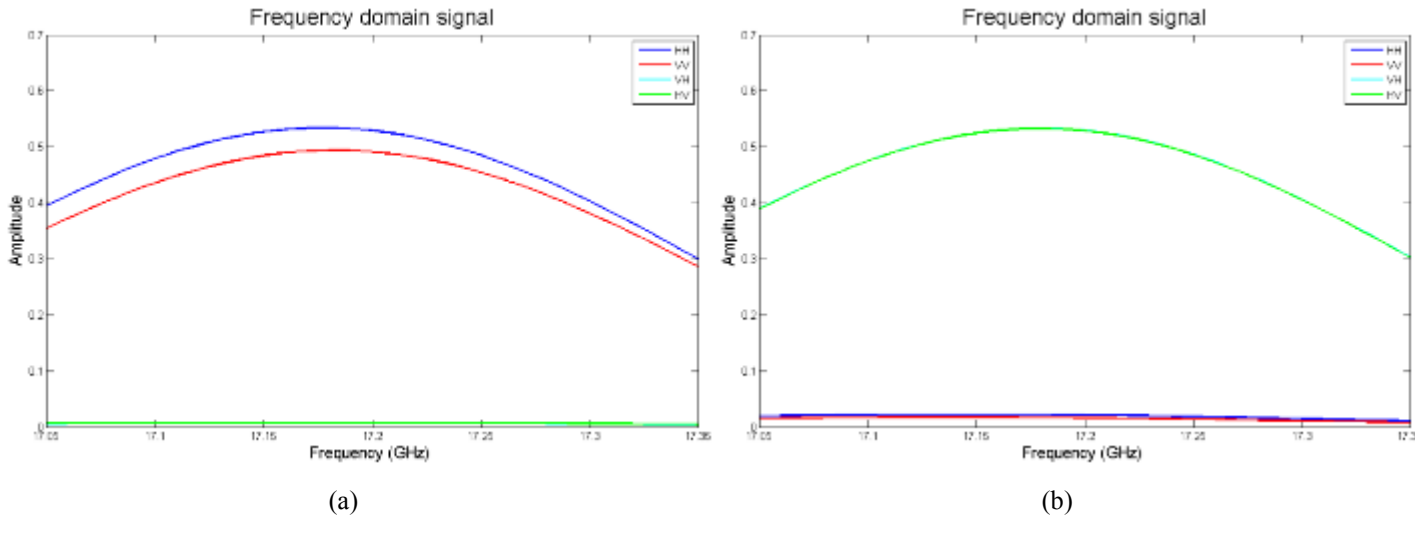
Figure 2.12 frequency domain respond (a) 0 degree dihedral corner reflector (b) 45 degree dihedral corner reflector

The calibration coefficients were estimated and depicted in the Figure 2.13,

(a)   (b)
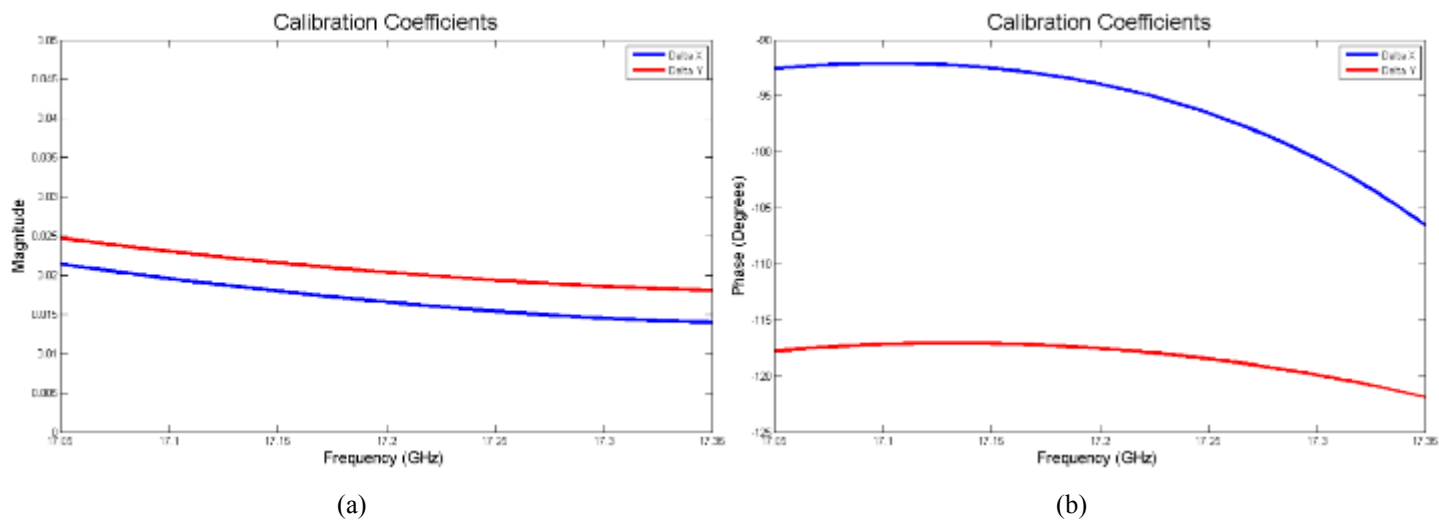
Figure 2.13 Calculated calibration coefficient for (a) 0 degree dihedral corner reflector (b) 45 degree dihedral corner reflector

The estimated cross-calibration factors (equation 2.26) was plotted in the Figure 2.14,
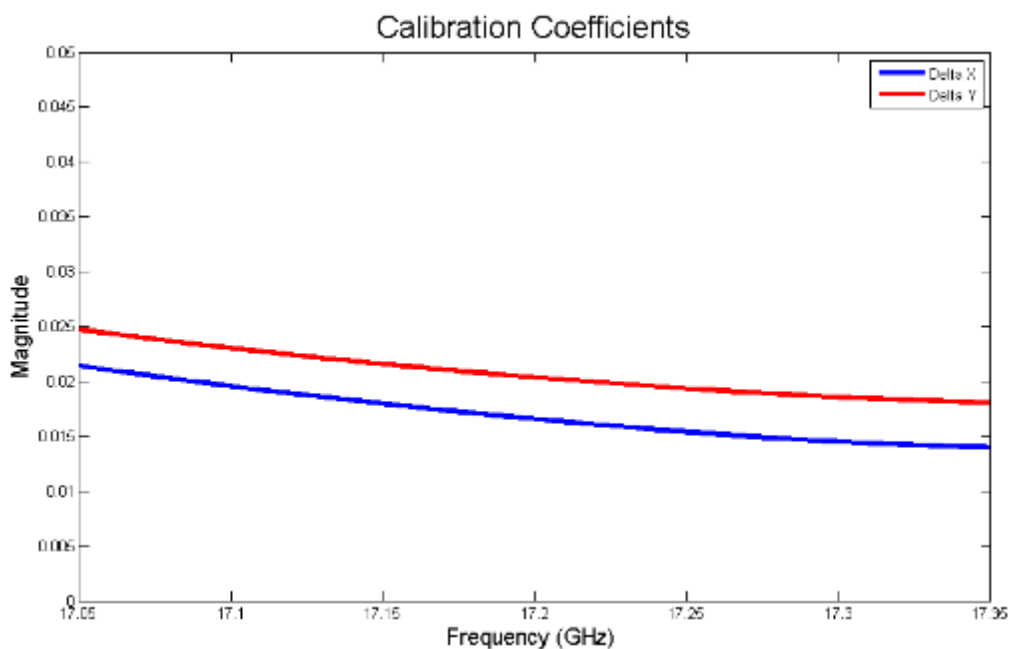
Figure 2.14 Estimated cross-calibration coefficients

Comparison of calibration results was depicted in Figure 2.15. The normalized scattering matrix of 0 degree orientation, both amplitude and the phase component was considered.

(a)

(b)

(c)

(d)
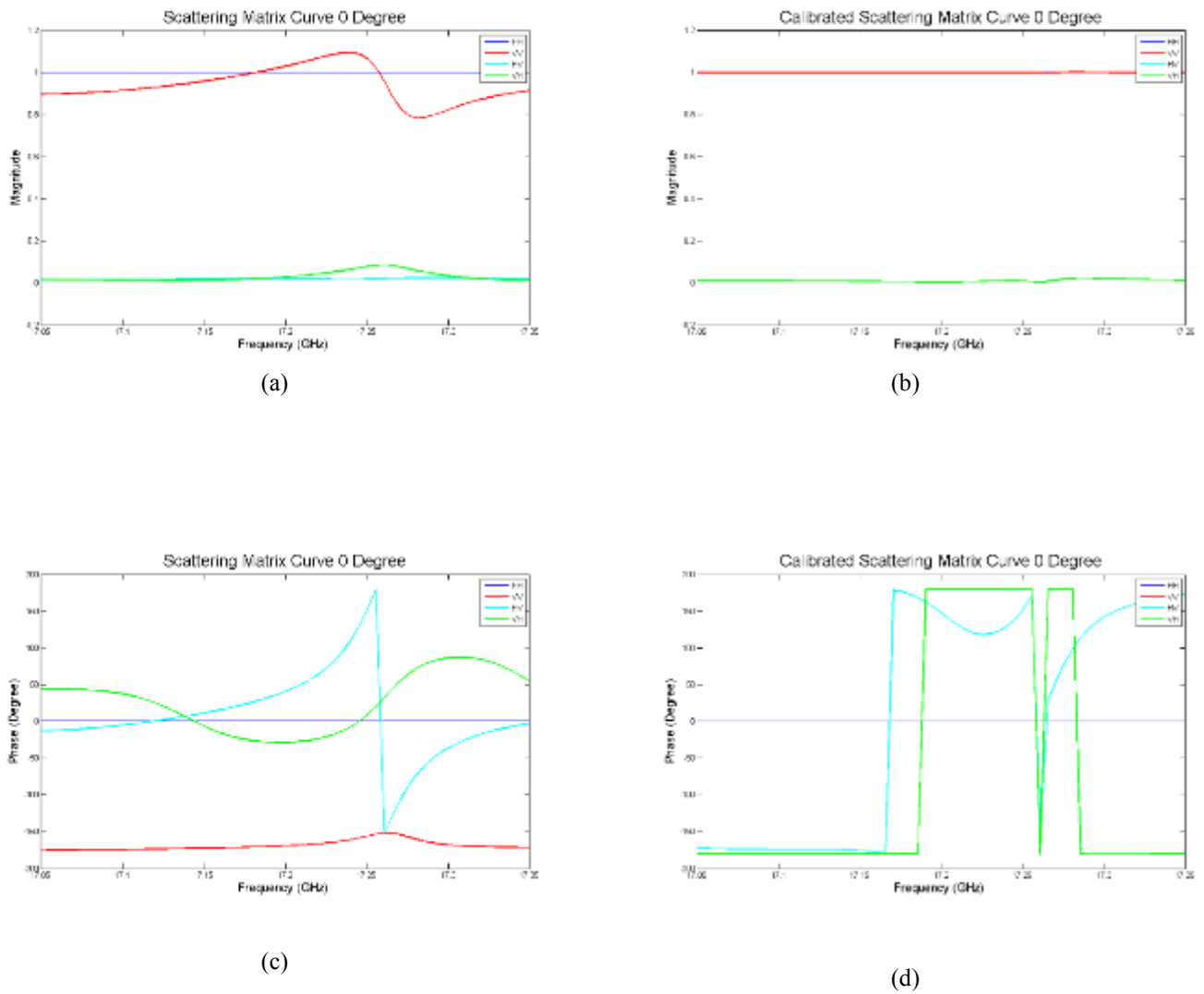
Figure 2.15 Normalized scattering respond (a) Amplitude component before calibration (b) Amplitude component after calibration (c) Phase component before calibration (d) Phase component after calibration for 0 degree dihedral corner reflector

Comparison of calibration results was depicted in Figure 2.16. The normalized scattering matrix of 45 degree orientation, both amplitude and the phase component was considered.
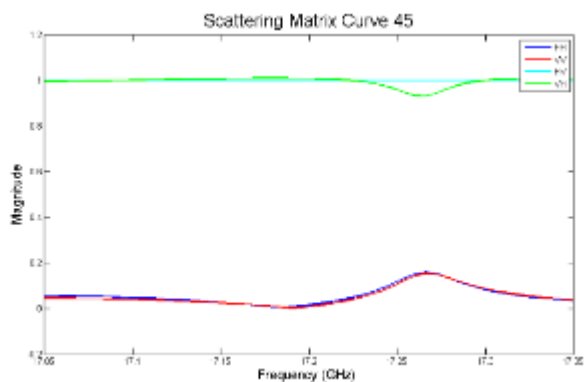
(a)
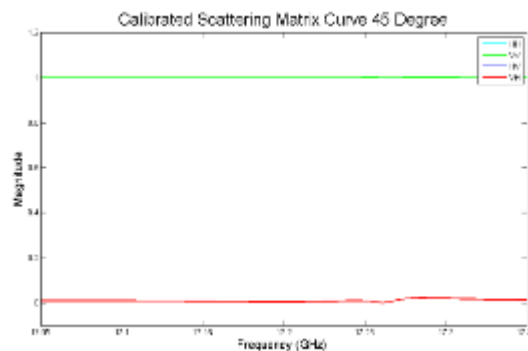
(b)
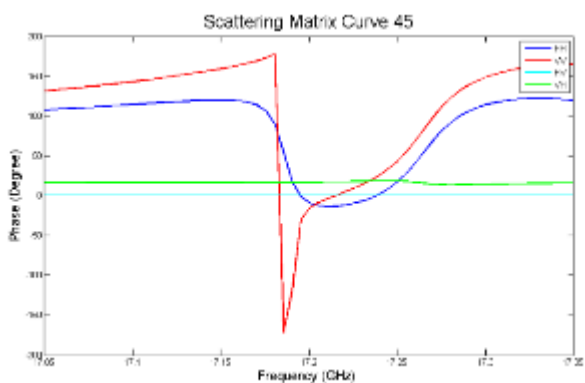
(c)
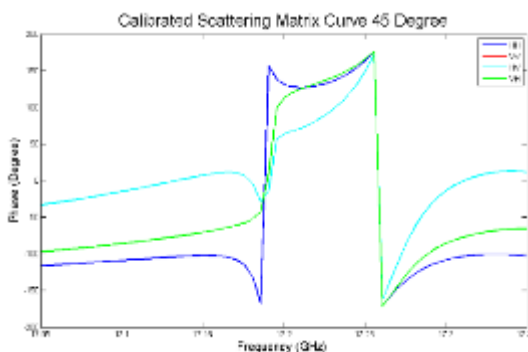
(d)

Figure 2.16 Normalized scattering respond (a) Amplitude component before calibration (b) Amplitude component after calibration (c) Phase component before calibration (d) Phase component after calibration for 45 degree dihedral corner reflector

2.4 Validation

From the theoretical value of stranded calibration targets and measured data, we can completely solve the equation group to recover the calibration coefficients (2.08)-(2.29). In fact, the measured data are picked up by time gating from the real measured signals of calibrators subtracted by the background signals. Using the calibration coefficients, the calibrated scattering matrix can be calculated with the aid of this equation (2.30).

(a)   (b)

(c)   (d)
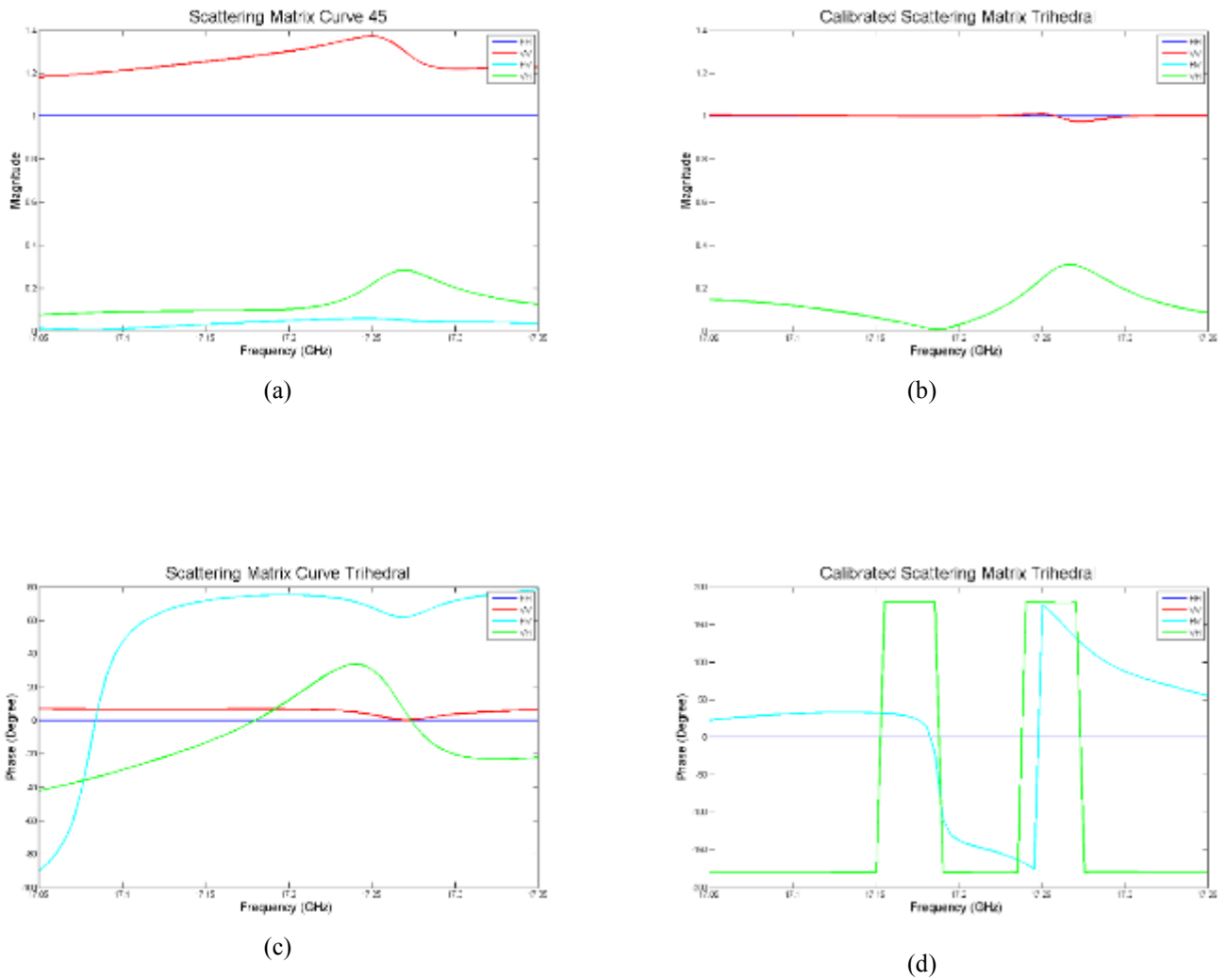
Figure 2.17 Normalized scattering respond (a) Amplitude component before calibration (b) Amplitude component after calibration (c) Phase component before calibration (d) Phase component after validation using trihedral corner reflector

2.5 References

[1] G.W. Stimson, "Introduction to airborne radar," Scitech publication, inc, second edition 1998.

[2] MetaSensing, "FastGBSAR User Manual," MetaSensing BV, Noodwijk, 2015.

[3] S. Placidi, A. Meta, L. Testa and S. Rödelsperger, "Monitoring Structures with FasGBSAR," in IEEE Radar Conf., Johannesburg, 2015.

[4] B.J. Lipa and D.E.Barrick, "FMCW signal processing," Mirage system, sunnyvale, California

[5] J.S. Lee and E. Pottier, Polarimetric radar imaging from basic to application, CRC Press, 2009.

[6] F. T. Ulaby et al., Microwave radar and radiometric remote sensing, The University of Michigan Press, 2014.

[7] H. Mott, Antennas for radar and communications: A polarimetric approach, Department of electrical engineering, University of Alabama, John willey & sons 1992.

[8] Z.S. Zhou, "Application of a Ground-Based Polarimetric SAR system for environmental study," Doctor dissertation of Tohoku University, Japan, August 2003.

[9] Lecture notes, EM wave and communication (PH323), Department of Physics, University of Peradeniya, Sri Lanka 2010.

[10] Lecture notes, Advanced radio systems (023), City & Guilds advanced diploma in applied telecommunication systems, UK 2011.

[11] Lecture notes, Signal and system (EE224), Department of electrical and electronic engineering, University of Peradeniya, Sri Lanka 2010.

[12] Lecture notes, Digital signal processing (EE325), Department of electrical and electronic engineering, University of Peradeniya, Sri Lanka 2010.

[13] A.V. Oppenheim, R.W. Schafer, J.R.Buck, "Discrete-time signal processing," Prentice-Hall, Inc. (second edition) 1999.

[14] F.T. Ulaby, "Fundamental of applied electromagnetics," Pearson prentice hall, Pearson education, Inc. (Media edition) 2004.

[15] B. Nagarajan, "Time frequency analysis-an application to FMCW radar," Master dissertation, University of Madras, Chennai, India 2001

[16] S. Attaway, "MATLAB a practical introduction to programming and problem solving," Butterworth-Heinemann, Imprint of Elsevier (second edition) 2012.

[17] M. Soumekh, "Synthetic aperture radar signal processing with MATLAB algorithms," A Wiley-Interscience publication, Lohn wiley & sons, Inc. 1999.

[18] G.D. Martin, A.W. Doerry, "SAR Polar format implementation with MATLAB," Sandia national laboratories, Albuquerque, California 2005.

[19] E. Gkioulekas, "Algorithem with MATLAB," Mathematical science computer center, University of Washington, USA, December 1996.

[20] B.D. Storey, "Computing Fourier series and power spectrum with MATLAB," Lecture notes – Communication systems, Department of computer engineering, University of Rhode Island, Kingston, USA.

Chapter 3 3D GIS model design for GB-SAR illumination

3D GIS model gives numerous information of ground surface when visual inspection is not necessarily sufficient for user specified analysis. It can be used to render the significant information about spatial dissemination of the electromagnetic signal emits by any active sensor system. This information can be used to optimize the sensor performance in order to achieve successful GB-SAR field experiment. In this chapter, we introduce new software tools that can be used to find the best installation location for the GB-SAR installation and the optimum hardware configuration in order to receive the maximum reflection from the area of interest. It will stringently improve the received data quality and the operating efficacy of the equipment.

3.1 Environmental modelling in spatial domain

With the rapid development of computer technology, space technology and modern information infrastructure, application of 3D GIS is increasingly widespread, covering the battlefield simulation, digital city, resource management, environmental assessment, regional planning, flood modeling, public facilities management as well as telecommunication, mobile communication and many other aspects [1][2]. For the environmental monitoring systems, a terrain is an important object of visual expression of Geographic Information Science based on the very complex natural scenery. Also, the 3D terrain visualization is an extremely important research field in the regions of the Earth, which can reflect the complex topography. Figure 1 (a) depicts the experiment done in front of the GPR laboratory, Tohoku University, Kawauchi campus. The main objective of this experiment is to create a 3D spatial model in a suburban environment in order to understand the power distribution of radar sensor. The radar was mounted on a portable tripod and looking toward GPR laboratory.

(a)   (b)
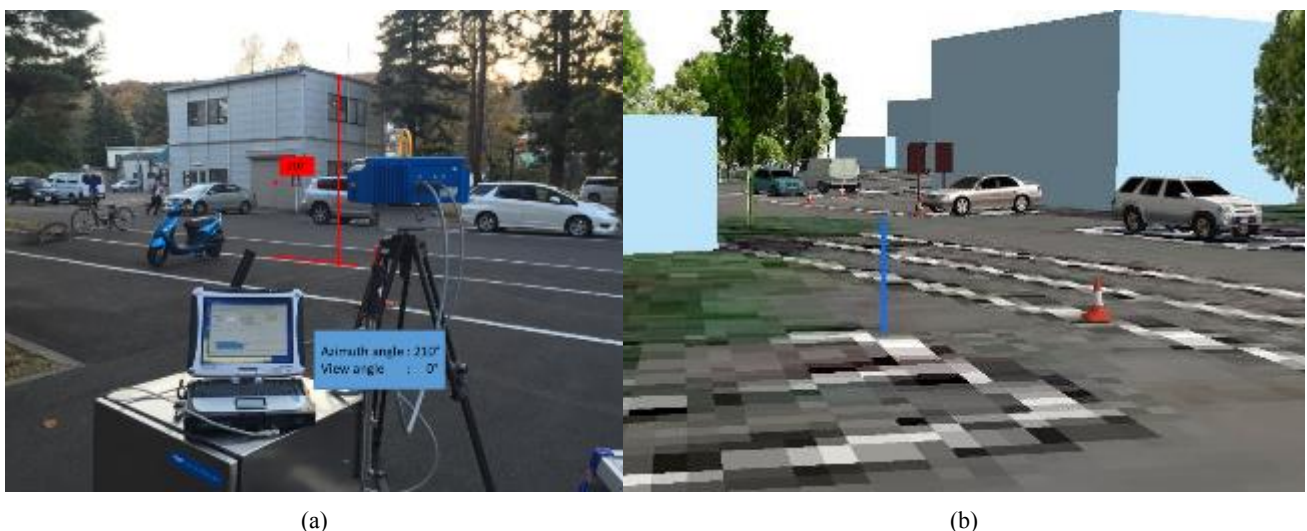
Figure 3.1 (a) Image taken near GPR room (b) 3D model interpretation of corresponding area

The environment in front of the radar system was mapped into geocoded Google image in the preliminary stage. The geocoded image was used to extract the ground truth data such as building location, tree locations and fixed obstacles such as a fence, road signs, vehicles observed during the experiment time. This information was separated into stranded vector data formats of point, line and polygon according to the physical geometries which accepted by ESRI ArcGIS software platform. It will assist,

- ➢ To understand the illumination area and area which is not illuminated by source due to its installation location,
- ➢ To estimate the angle of incidence in specific illumination area,
- ➢ To estimate the incidence power in specific illumination area,
- ➢ To find the relative location of the AOI,
- ➢ To interpret the information more accurately and user-friendly.

With the rapid development of information technology and major needs, the software needs to be developed to support the trend of dynamical, fast system, user-friendly and can be used by the wider society. Therefore, it is necessary to develop an integrated application for data processing of special 3D visualization resources information systems. The compatible software that is widely used today, the spatial database can be utilized more effectively and efficiently. Therefore we have proposed 3D GIS model assisted survey in order to find the best location for GB-SAR installation and estimate the best GB-SAR configuration prior to site installation. The new software tool were designed in order to estimate the optimum radar illumination. The developed technique was successfully used for feasibility survey in large scale landslide location in Minami-Aso, Kumamoto. The simulation result shows the expected illumination from different installation location in the designed 3D model [3].

3.2 3D Model design

3.2.1 Kumamoto earthquake and landslide

<p style="text-align:center">(a.)   (b.)</p>
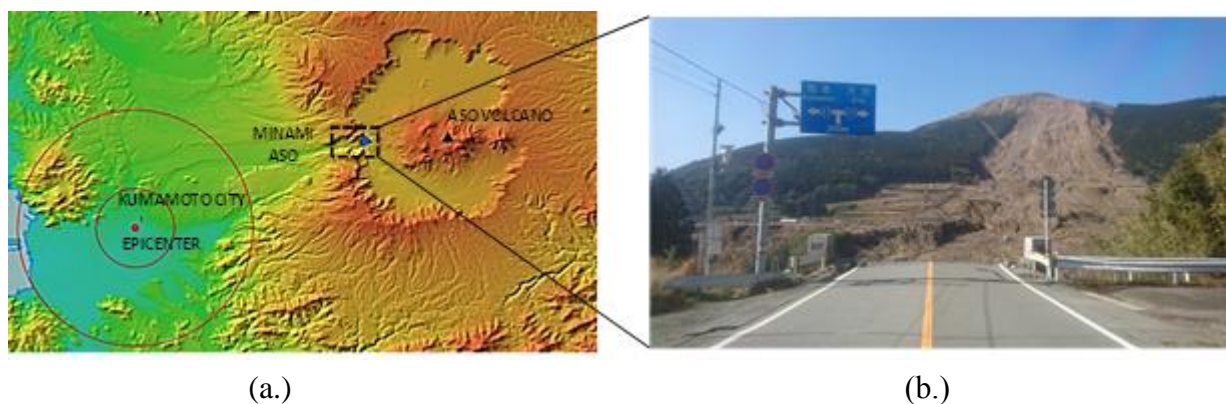
Figure 3.2 (a) The Kumamoto earth quake (April, 2016) epicenter and the location of the landslide was shown in elevation map. The image taken during the first field observation, Minami-Aso was shown on figure 3.2 (b)

The Kumamoto earthquake named as the largest catastrophic earthquake recorded in the recent year. In April 2016, the highest number of foreshock and aftershocks were recorded near to the Futagawa and Hinagu fault zones, which expanded northeastward and southwestward along the Kyushu Island in Japan. A M6.5 earthquake occurred at 21:26 JST on April 14th, and a M7.3 earthquake at 01:25 JST on April 16 were occurred [4]. The two earthquakes killed at least 50 people and injured about 3,000 others in total. Severe damage occurred in Kumamoto and Ōita Prefectures, with numerous structures collapsing and catching fire. More than 44,000 people were evacuated from their homes due to the disaster [5].

The number of earthquake-triggered landslides was significantly increased and the largest one was reported near to the National road 57. It was named after the 200m long *Aso-ohashi* bridge that formerly spanned the 80m deep gorge of the *Kurokawa river* [6]. Also, the main debris flow of the landslide was shut off the main railway and the road which connects the two prefectures.

3.2.2 Disaster recovery project

The sudden recovery projects were launch to remove the debris flow after the landslide. It was started as part of the disaster recovery plan. The deposited soil layer of the main debris flow near to the mountain foot was removed by the manned vehicles and the unstable soil layer closed to the mountain peak was removed by the unmanned vehicles controlled by the nearby remote station. This total soil removal process was completed and road construction project was launched from January 2017. Due

to the instability of the top soil layer on the hillside and number of the recorded earthquake in the fault zone, stability information of the open soil layer become significantly important for the workers who involve with daily road construction work. In this background, GB-SAR remote sensing technique notified as the best solution for retrieving the stability information of the total landslide area in order to give the landslide early warning for the workers from the remote monitoring station for disaster prevention.

3.2.3 LiDAR survey

Lidar has become an established method for collecting very dense and accurate elevation data across landscapes and project sites. This active remote sensing technique similar to radar but uses laser light pulses instead of radio waves. Lidar is typically "flown" or collected from planes where it can rapidly collect points over large areas. Lidar, as a remote sensing technique, has several advantages. The foremost among them are high accuracies, high point density, large coverage areas, and the ability of users to resample areas quickly and efficiently. This creates the ability to map discrete changes at a very high resolution, cover large areas uniformly and very accurately [7][8].

After the earthquake triggered a landslide in the western tip of the *Aso* caldera highlighted as the largest landslide recorded in post disaster period. In another hand, it stops the main transportation roads which connect in *Kumamoto city* and *Oito city*, distorted the main access bridge which crosses the *Kurokawa River*. The LiDAR survey conducted in May 2016 was processed into 30 cm x 30 cm pixel resolution, with 32 bit pixel depth raster layer, was shown in Figure 3.3. It was geocoded and projected into JGD_2001_54N standard projected coordinate system and overlaid in satellite image base layer in order to find relative locations. The total area of the processed LiDAR information (Table 1) was covered around 3 km x 2 km in ground area including western tip of the *Aso* caldera in the middle, national road 57 in west-east and south-north near to the bottom and right corner, *Kurokawa river* from north-south direction in right side corner of the Figure 3.3.

Table 1. LiDAR Information

Parameters	Value
Data format	Laser file format
Survey month	May 2016
Survey area	3 km x 2 km
Number of bands	1
Pixel depth	32 Bit
Elevation range	266.306-815.734 m
Top extent	3641054.86312
Left extent	683532.209701
Right extent	686819.797314
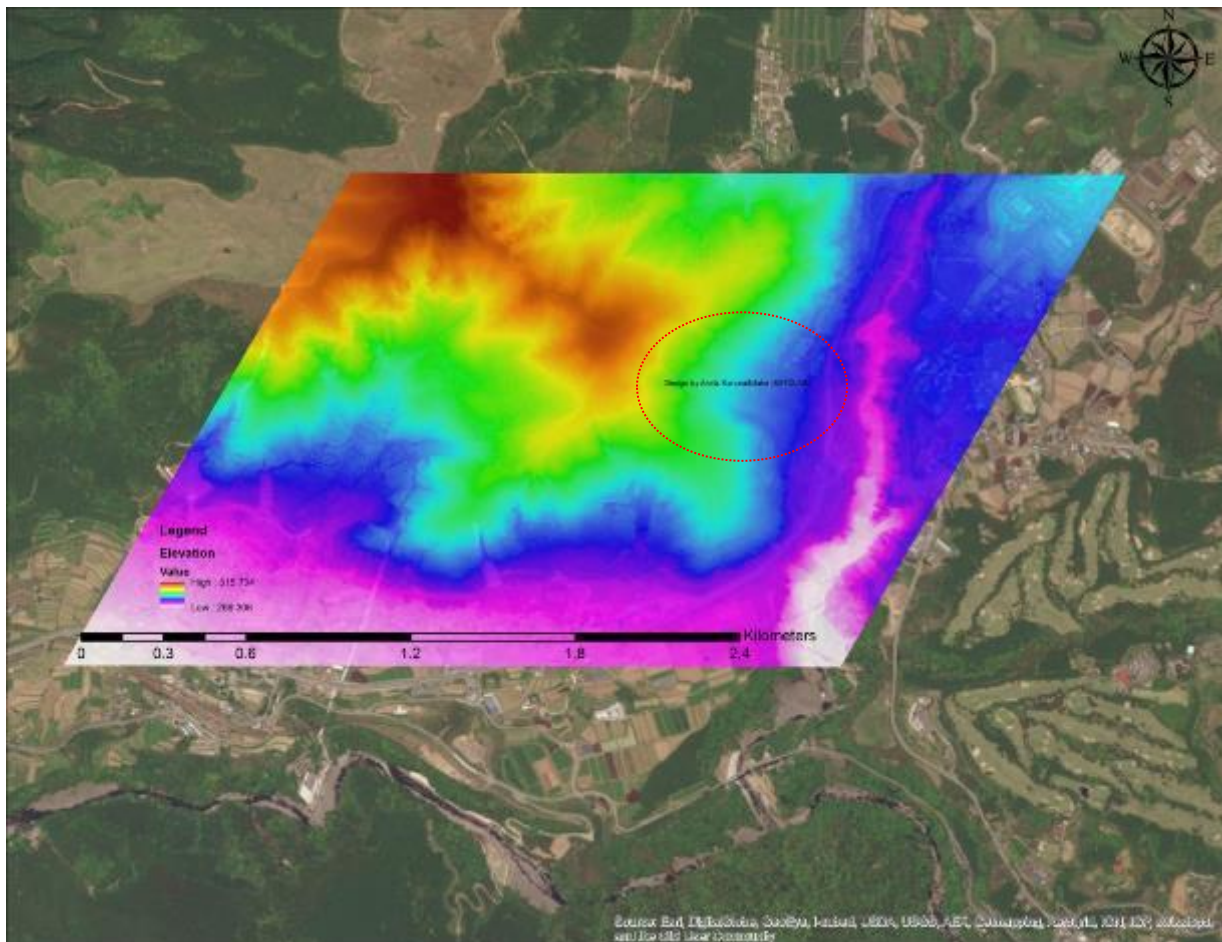
Figure 3.3 LiDAR information of the Mianmi-Aso area was shown. It was geocorded and ovelay with the base map inorder to find the relative location.

After the geocoding, the elevation profile of the processed LiDAR data was estimated as 265 m at *Kurokawa river* and the highest value was recorded as 815 m at peak of the western tip of the mountain cliff. By the color ramp of the elevation profile, rapid elevation change can be observed with in the short distance in the horizontal plane. This has the higher potential and favorable factor to triggered landslides. The overall results of LiDAR survey show the number of the landslide which triggers after the earthquake. The area covered by the circle has recorded the largest landslide and debris flow which collapse the *Aso Ohaiso Bridge* after the landslide. Since the area was restricted for access, LiDAR survey gives considerable results with highly accurate ground truth information. The geocoded LiDAR information can be used to visualize the existing environment than any other remote sensing and pin point measurements. This information can be further processed to obtain the 3D model. It will render more realistic information which is significantly important to estimate spatial dissemination of EM radiation, prior to deploying any ground based remote sensing technique such as GB-SAR.

3.2.4 Digital elevation model (DEM)
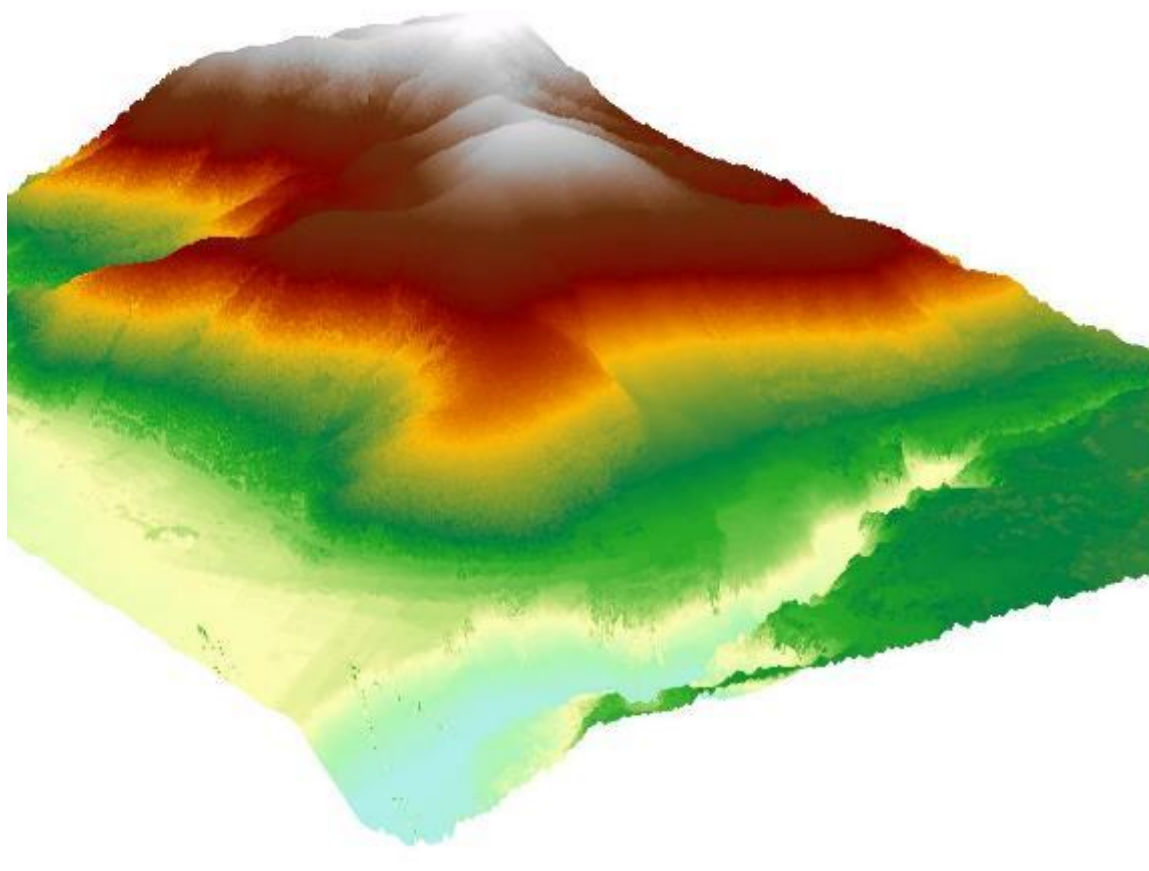
Figure 3.4 DEM generated with 30 cm x 30 cm pixel resolution was shown

The designed DEM model was geocoded with the local coordinated system. Both horizontal and vertical coordinate system was used to preserve the accuracy of the LiDAR information in the horizontal and vertical plane. This information was summarized in table 2.

Table 2 DEM Information

Parameters	Value
Spatial Reference	JGD_2000_UTM_Zone_52N
Survey month	May 2016
Liner unit	Meters (1.000000)
Angular Unit	Degree (0.01745329251994)
False Easting	50000
False Northing	0
Central Meridian	129
Scale Factor	0.9996
Datum	D_JGD_2000

3.3 Software tool design
3.3.1 Estimation of radiation pattern

An antenna radiation pattern describes the far-field directional properties of an antenna. By virtue of reciprocity, a receiving antenna has the same directional antenna pattern as the pattern that it exhibits when operated in the transmission mode. The strength of the radiated field or power density of antenna can be specified by the zenith angle θ and azimuth angle ϕ. For an antenna with a single main lobe, the pattern solid angle Gammap describe the ebullient width of the main lobe of the antenna pattern [9]. It can be described as the integral of the normalized radiation intensity $F(\theta,\phi)$ over a sphere,

$$\Omega_p = \iint F(\theta,\phi)d\Omega \tag{3.1}$$

This pattern solid angle characterized the directional properties of the 3D radiation pattern. The only practical way to increase the directivity of an antenna wave guide is to flare out its end into a horn. In Figure 3.5 (a) and Figure 3.5 (b) shows the rectangular horn antenna used in GB-SAR Figure 3.5 (c), sensor and its dimensions. By using these geometrical parameters the H- plane radiation pattern and the E-plane radiation pattern was estimated.

(a)   (c)

(b)
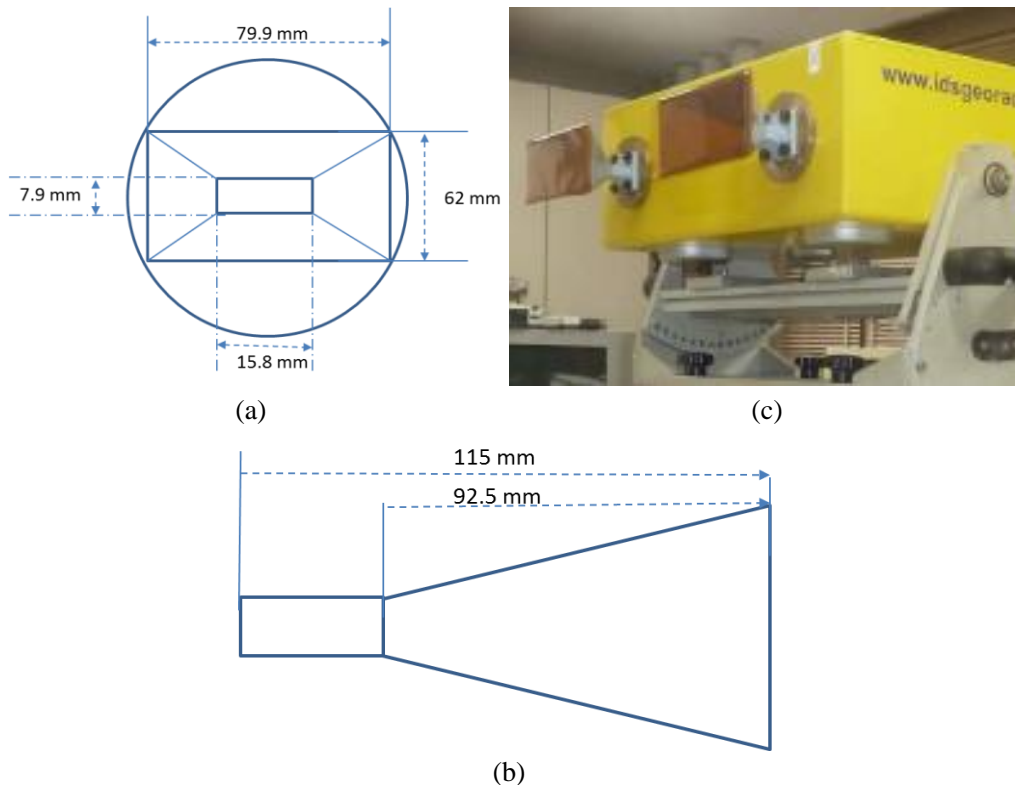
Figure 3.5 (a) and (b) The dimension of the rectangular horn antenna used in (c) GB-SAR was shown in GB-SAR was shown
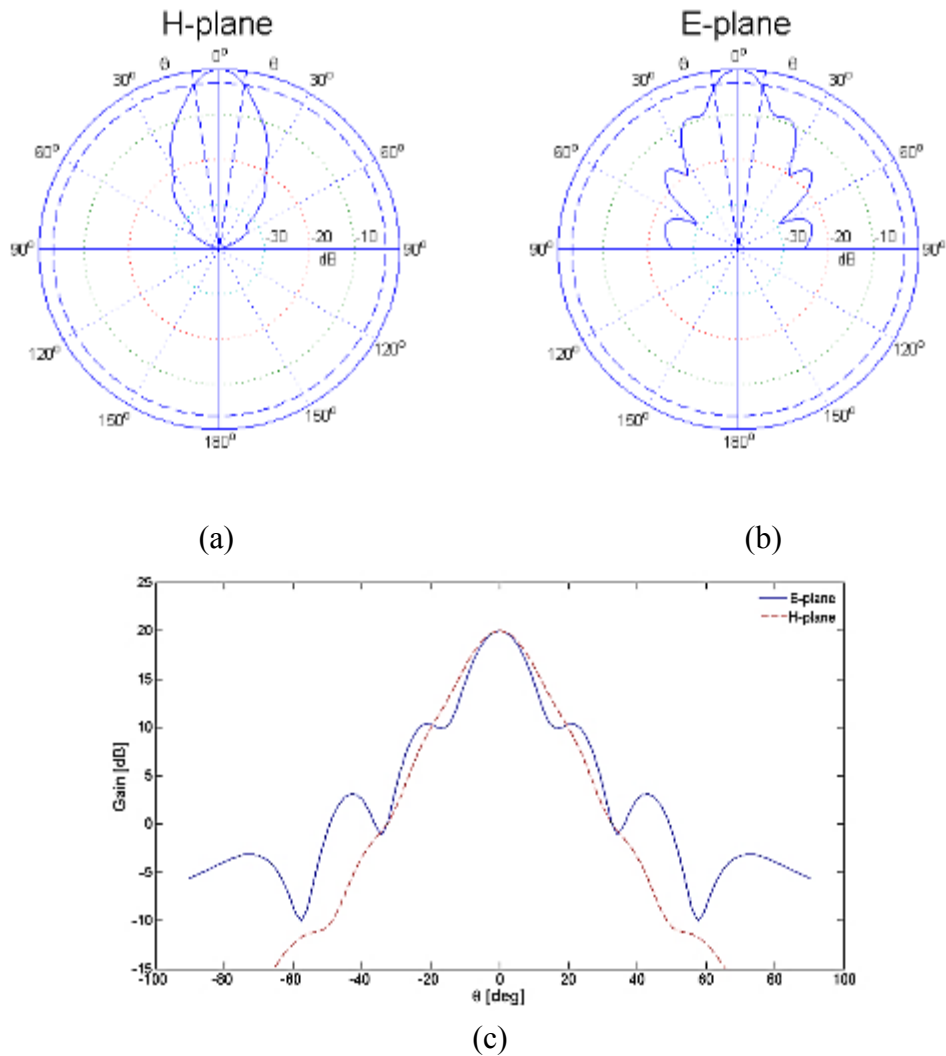
Figure 3.6 (a) Estimated radiation pattern in H –plane (b) Estimated radiation pattern
in E –plane and (c) comparison of radiation power in H and E plane

The estimated radiation pattern in each plane gives the directivity properties of the GB-SAR and
radiation pattern as depicted in Figure 3.6 (a) and Figure 3.6 (b). The half-power beam width of the H-
plane and E-plane radiation pattern in the GB-SAR system defined as the angular width of the main
lobe between the two angles at which the magnitude of $F(\theta, \phi)$ is equal to half of its peak value (-3dB
point).

Table 3 Antenna parameters

System Parameters	Value
Horn antenna model	FGBS-ANT-HRN15
Gain	15 dBi
Frequency range	17.05-17.35 GHz
E-plane beam width	32.2°
H-plane beam width	31.9°
Waveguide shape	WG19(WR51,R180)

3.3.2 Vector grid design

We have developed a new software tool to extract spatial information from the terrestrial model. It was developed in Python platform with Arcpy, Numpy libraries [10]. The conical polygon area which given by the estimated radiation pattern was further decomposed according to the range and the azimuth resolution of the SAR image.
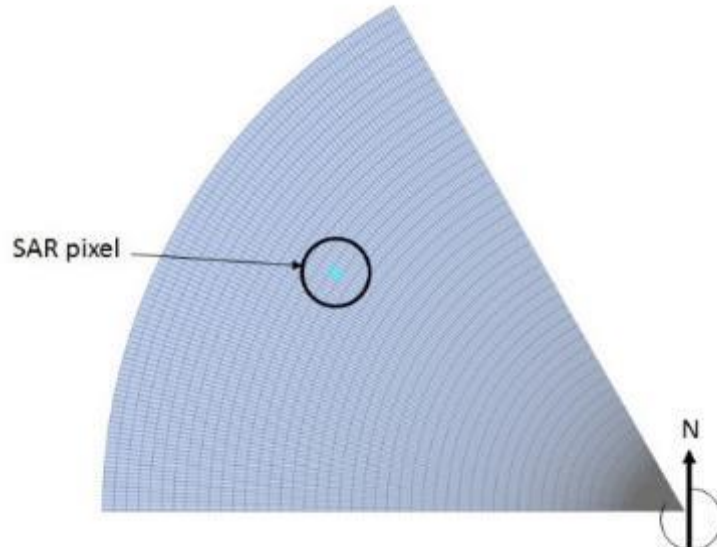
Figure 3.7 The SAR polygon grid tool

The azimuth resolution of the SAR image corresponds to the distance between the two lines in the sector circle of polygon grid. The range resolution of the SAR image corresponds to space between two circular arcs in polygon grid. The azimuth resolution of the GB-SAR image can be calculated by,

$$R_{AZ} = \frac{\lambda_C}{2L} R \qquad (3.2)$$

whereas λ_C is the wavelength of the center frequency of the transmitted signal and L is the length of the GB-SAR rail. The Range resolution R_{RN} of the system can be calculated by

$$R_{RN} = \frac{c}{2B} \qquad (3.3)$$

whereas c is the speed of light in the free space and B is the frequency bandwidth of the transmitted radar signal. The location of a ground patch can be critical for subsequent analysis. Therefore a complete regular sampling network was biased and it coincides in the interval with a regular pattern in the digital elevation model (DEM).

3.3.3 Estimation of illumination pixel

Estimation of pixel orientation
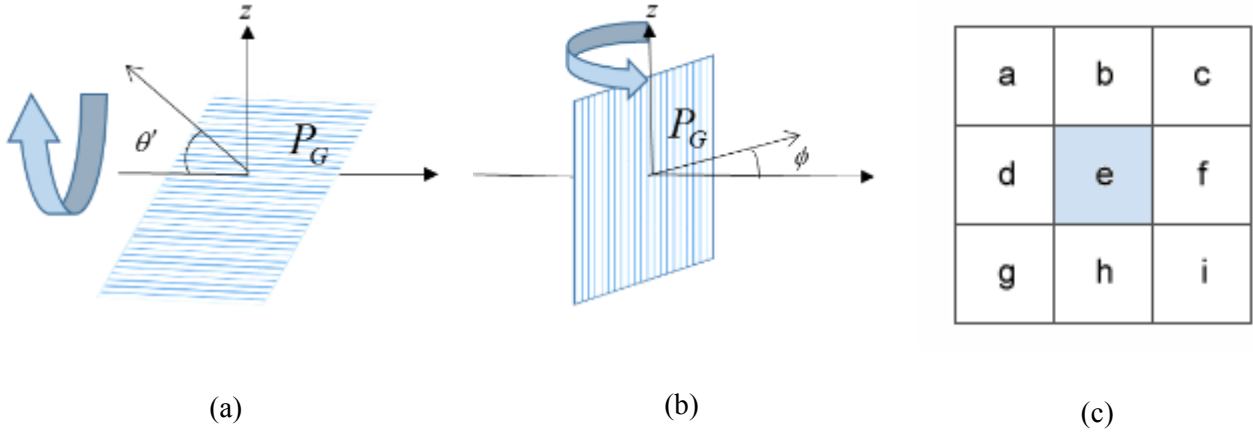
Figure 3.8 Raster pixel orientation in (a) vertical plane (b) horizontal plane and the 3 x 3 kernel used for estimate east-west gradient and south-north gradient.

The gridded surface is supposed to be mathematically continuous. It is possible to derive the mathematical derivatives at any location. In practical, since the raster surface has been discretized, the derivatives along two rectangular planes can be used to approximate the pixel orientation in both vertical plane (plane perpendicular to earth surface) and the horizontal plane (the plane parallel to the earth surface) [11]. In this analysis, the pixel orientation in vertical plane was estimated by gradient, the maximum rate of change of altitude using equation 3.4. The pixel orientation in horizontal plane was estimated by equation 3.5,

$$\tan S = [\left(\delta z / \delta x\right)^2 + \left(\delta z / \delta y\right)^2]^{1/2} \tag{3.4}$$

$$\tan A = [\left(\delta z / \delta y\right) + \left(\delta z / \delta x\right)] \tag{3.5}$$

The corresponding finite difference estimator using all outer points of the kernel in Figure 3.8 (c) in window by,

For the east-west gradient and south-north gradient of the raster layer

$$\left[\delta z / \delta x\right] = [\left(z_{i+1,j+1} + 2z_{i+1,j} + z_{i+1,j-1}\right) - \left(z_{i-1,j+1} + 2z_{i-1,j} + z_{i-1,j-1}\right)]/8\delta x \tag{3.6}$$

$$\left[\delta z / \delta y\right] = [\left(z_{i+1,j+1} + 2z_{i+1,j} + z_{i+1,j-1}\right) - \left(z_{i-1,j+1} + 2z_{i-1,j} + z_{i-1,j-1}\right)]/8\delta x \tag{3.7}$$

(a)

(b)

Figure 3.9 (a) The 2D location of the ground patch (b) The 3D location of the groun patch.

Figure 3.9 (a) shows the 2D location of the raster pixel PG on DEM surface which was located Δd distance from GB-SAR location R. Figure 3.9 (b) shows the 3D location of the illuminated PG´. Thereby the reflection angle can be estimated by [3],

$$\alpha = \arctan\left[\frac{\Delta z}{\sqrt{(\Delta x)^2 + (\Delta y)^2}}\right]$$

(3.8)

3.4 Application of develop method

3.4.1 Field Survey- Minami Aso

Figure 3.10 The proposed location for GB-SAR installation was shown in Loc1 to Loc6 which located in left side (blue) and right side (green) to the *Kurokawa River.*

The thematic map in Figure 3.10 shows the 1 km x 1km area around the main landslide of Minami-Aso. The Spatial dissemination of the radiated signal is an indispensable factor for environmental monitoring systems. It renders the significance information about equipment usability, prior to the field installation. 2D map shows the possible location for the GB-SAR installation which investigated after the field survey. After the catastrophic landslide, the geography of the surrounding was anonymous changed and many places become inaccessible. Meantime, the infrastructure such as transportation, electricity was shouted off and the equipment maintenance facilities were not tantamount in each place. In this background, preliminary estimation for the equipment applicability become mandatory to estimate the system deployment parameters and appropriate configuration. The road reconstruction project was actively carried out in the bottom of the mountain and the GB-SAR illumination was not necessarily needed in all the view of the open soil layer. This makes the requirement more sophisticated method to estimate the GB-SAR illumination prior to the site deployment in order minimize the calibration time for fast deployment in a disaster situation.
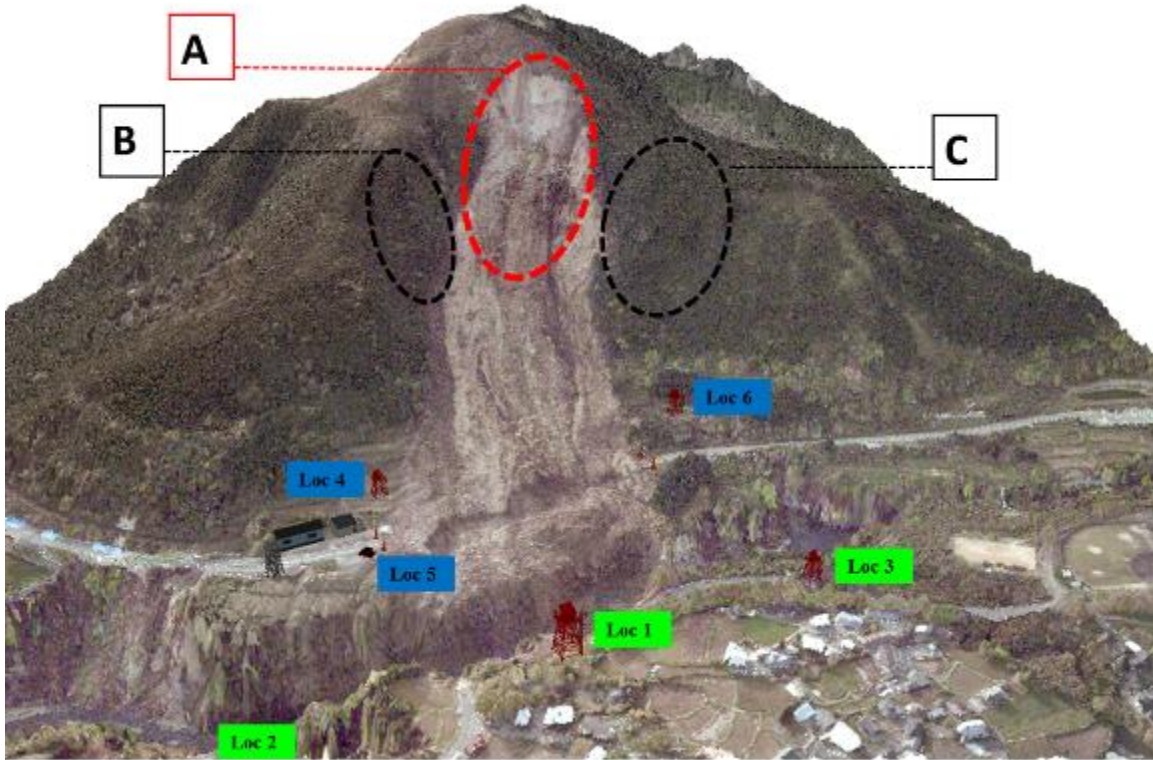
Figure 3.11 The figure shows the 3D simulation model of the *Minami-Aso* area.

After the earthquake, the main debris flow was flushed with dense forest canopy. The open soil layer of the mountain creep was divided into two layers according to the disaster recovery work. The soil layer near to the crown of landslide and surrounding (area A) was prioritized. The remaining unstable soil layer of this area was started to remove by unmanned vehicles which operated by the remote station. This process was systematically done until December 2016. Starting from January 2107, the road reconstruction projects were launched and workers start to work the bottom of the mountain. Due to the instability of the top soil layer on the hillside and the number of the recorded earthquake in the fault zone, stability information of the open soil layer and the newly created geological boundaries in area B, area C become significantly important for the workers who involve with daily road construction work. The proposed locations for GB-SAR installation was shown in Figure 3.11. The 3D model from Loc1 to Loc6 which located on the left side (blue) and right side (green) to the *Kurokawa* River.

3.4.2 3D Simulation results for location selection
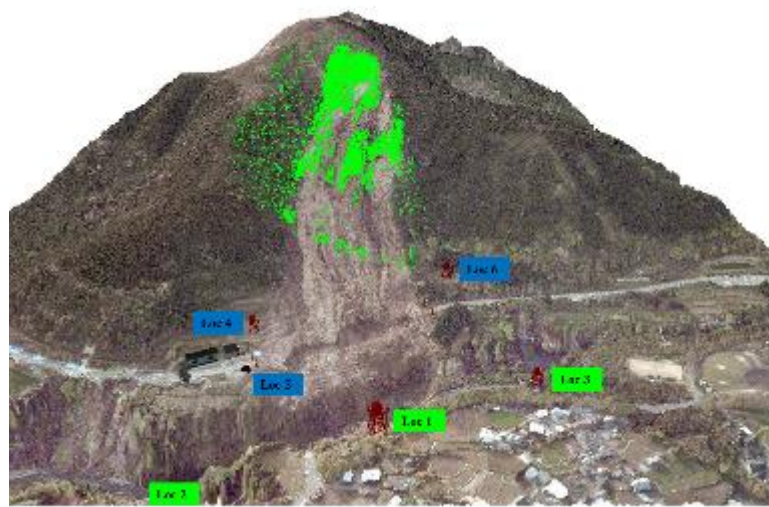
(a)
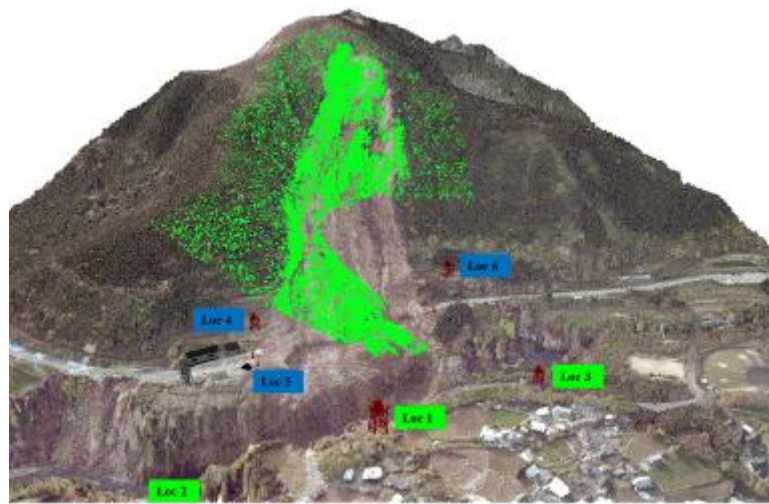
(b)
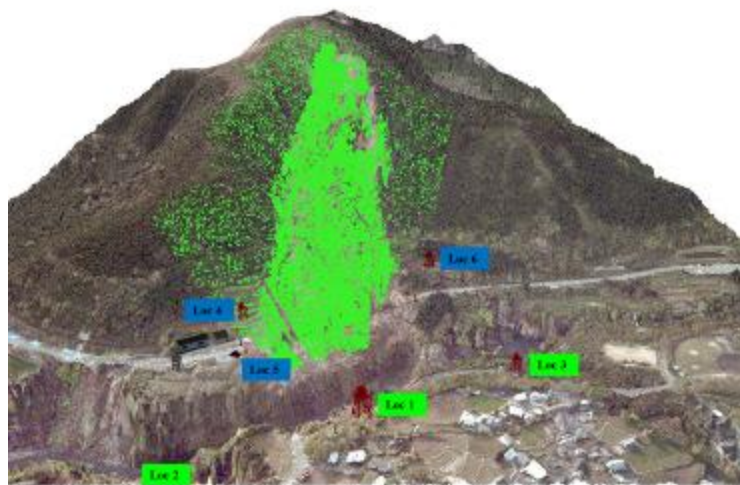
(c)

Figure 3.12 Estimated illumination by simulation results (a) Location 6 in left side of the river and (b) Location 3 and (c) Location 1, right side of the river

The expected illumination for Loc1 to Loc6 was estimated by the developed 3D model. It gives the maximum range, optimum height of the system platform, azimuth angle in the horizontal plane and view angle in the vertical plane. The simulation results with possible installation parameters were summarized in Table 3. The estimated illumination information was geocoded by the local coordinate system and projected on a 3D model. Figure 3.12 (a) shows the expected illumination from Loc6 (in left river bank) and Figure 3.12 (b) and Figure 3.12 (c) shows the expected illumination from Loc1 and Loc3.

Table 3. Estimated parameters for GB-SAR installation

Installation location	Latitude	Longitude	Radar Range (m)	Base height (m)	Azimuth angle (°)	View angle (°)
Loc1	32.883945°	130.990160°	1000	8	290	15
Loc2	32.880030°	130.989195°	1000	10	300	15
Loc3	32.886185°	130.989912°	1000	10	265	15
Loc4	32.883408°	130.986888°	900	7	310	30
Loc5	32.882468°	130.987070°	900	2	315	23
Loc6	32.886487°	130.987352°	900	7	265	15

3.4.3 3D Simulation results for optimum GB-SAR configuration

(a)

(b)

(c)

(d)
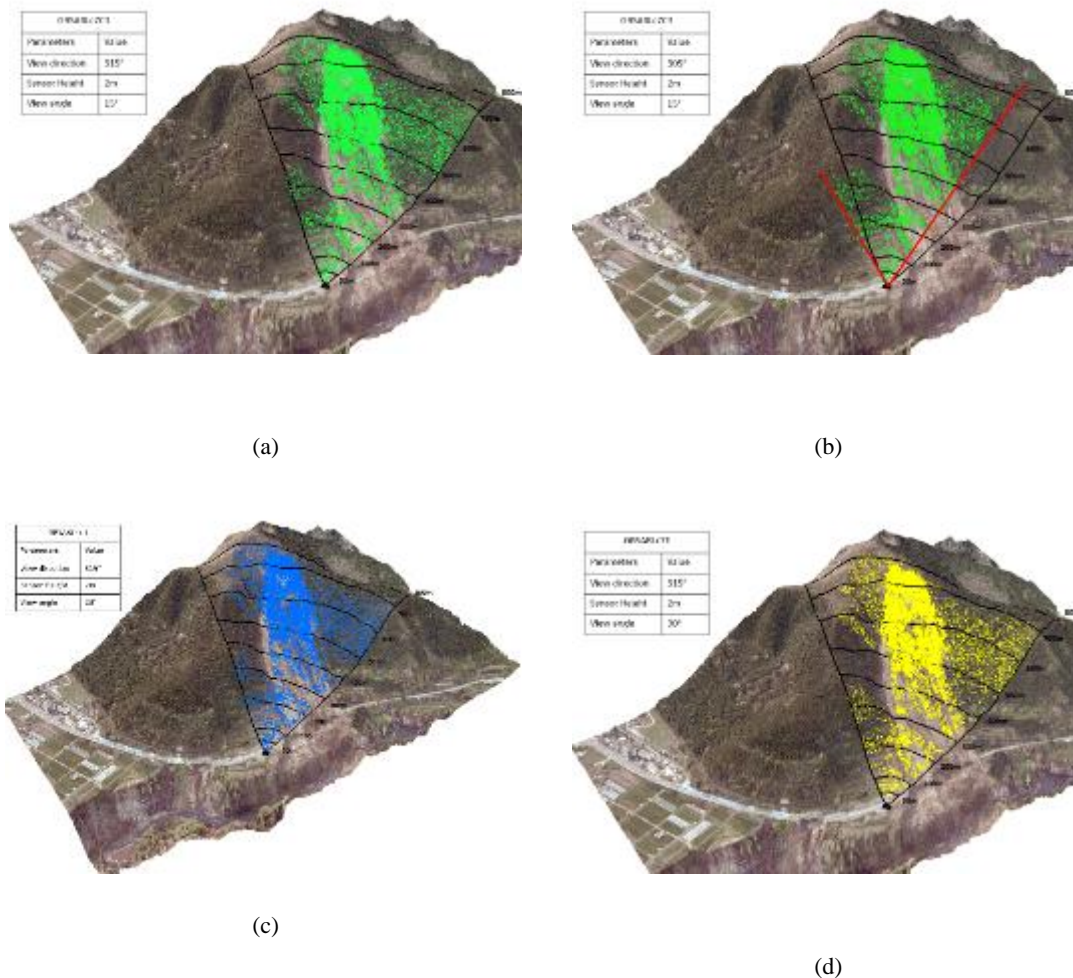
Figure 3.13 Estimated illumination for configuration (a), (b), (c) and (d) by simulation results

Table 4 Summery of GB-SARconfiguration

Configuration	Base height (m)	Azimuth angle (°)	View angle (°)	Illumination area (%)
(a)	2	290	15	76.1
(b)	2	305	15	73.1
(c)	2	315	23	77.4
(d)	1.5	315	30	70.4
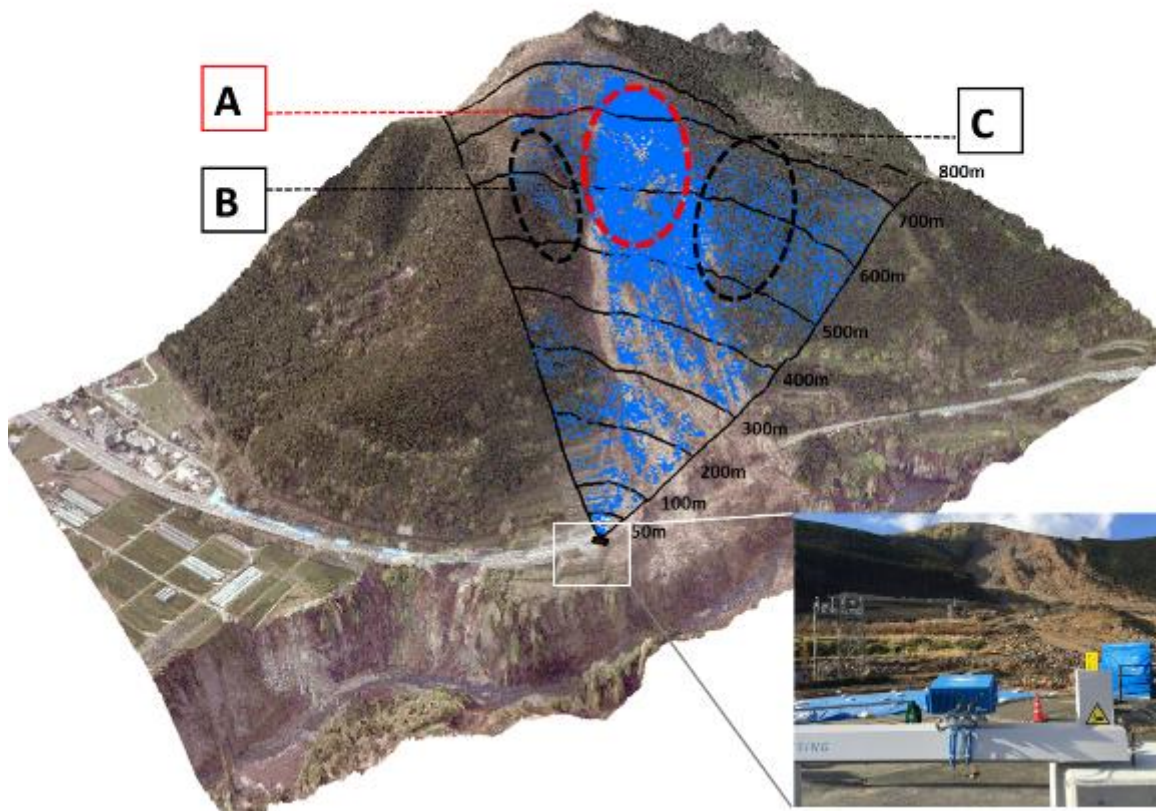
Figure 3.14 The blue color depict the estimated illumination for location 5. The zone A, B and C show the relatively higher illumination than surrounding area. The GB-SAR system was installed in this location and continuous monitoring was started from January, 2017

The location 5 was selected for system installation by considering optimum illumination from expected zones. In advanced, this location was highlighted due to the accessibility of maintenance work and supply for electricity and other infrastructure facilities which were highly important for the real time monitoring. The GB-SAR system was installed and data acquisition was started from mid of January 2017. The linear rail was mounted in 1.5 m rigid concrete blocks, in order to achieve estimated height for a stable platform. The system was aligned to 315° LOS with 23° views (tilt) angle as shown in Figure 3.13.

3.4.4 Estimation and validation
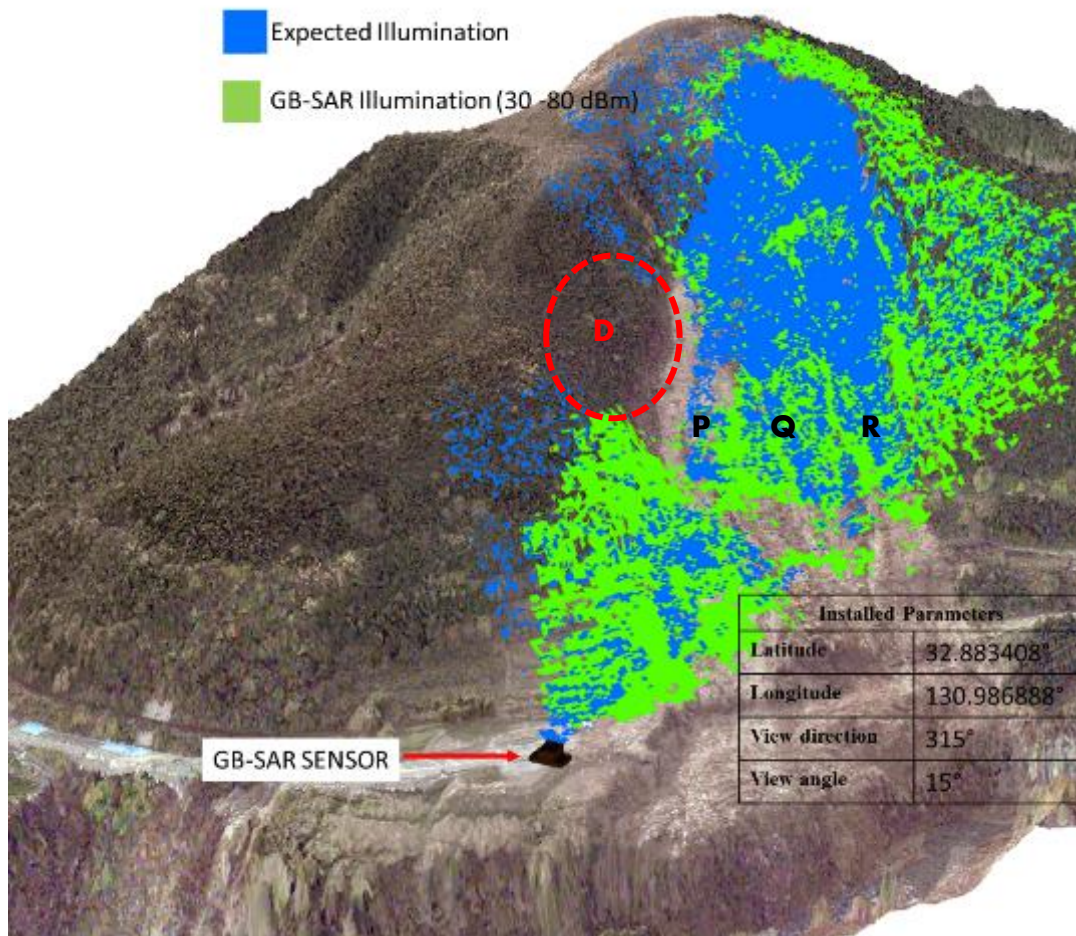
Figure 3.15 Comparison of estimated illumination in blue color and real illumination in green color.

The estimated illumination and the acquired SAR processed power image (20-30 dBm) was projected in the 3D model. The Figure 3.14 shows the better correlation between simulation results and experimental results. In the simulation results, the GB-SAR illumination shows the discontinuity in illumination area E which around 350 m distance from the GB-SAR sensor. This can be seen in the real illumination observed in SAR processed image. It could be due to the elevation difference of the mountain cliff along radar LOS. Besides the open soil layer of main landslide area, the reflection becomes more random due to the tree canopy. Therefore the backscatter power becomes lower. In the 3D model design by LiDAR data is affluent with this ground truth information. So we can see very clear illumination difference in simulation results of soil layer and the tree canopy. Furthermore, three separate linear wedges shape structure of p, q, r can be seen in the simulation results of main landslide area. These structures become more identical and visible to the processed GB-SAR images.

3.5 References

[1] Lecturer notes, "Advanced Technologies in GIS," Master degree program in remote sensing and GIS, Postgraduate institute of science, University of Peradeniya, Sri Lanka.

[2] Lecturer notes, "Spatial analysis and modeling," Master degree program in remote sensing and GIS, Postgraduate institute of science, University of Peradeniya, Sri Lanka.

[3] A. Karunathilake and M. Sato, "3D Model assisted survey to design and estimate ground based SAR illumination," in 第 42 回リモートセンシングシンポジウム., Chiba. 2017, pp. 35-38.

[4] K. Dang, K. Sasa, H. Fukuoka, N. Sakai, Y. Sato, K. Takara, L. H. Quang, D. H. Loi, P. V. Tien and N. D. Ha, "Mechanism of two rapid and long-runout landslides in the 16 April 2016 Kumamoto earthquake using a ring-shear apparatus and computer simulation (LS-RAPID)," Recent Landslides, Springer-Verlag Berlin Heidelberg, vol. , August 2016.

[5] Online resource, Wikipedia, https://en.wikipedia.org/wiki/2016_Kumamoto_earthquakes

[6] Y. Yagi, R. Okuwaki, B. Enescu, A. Kasahara, A. Miyakawa and M. Otsubo," Rupture process of the 2016 Kumamoto earthquake in relation to the thermal structure around Aso volcano," Earth planet and space, Springer, vol., July 2016.

[7] H.K. Heidemann, Lidar Base Specification, Chapter 4 of Section B, U.S. Geological Survey Standards 2014.

[8] U. Wandinger, Introduction to Lidar, TeLeibniz Institute for Tropospheric Research, Permoserstraße 15, D-04318 Leipzig, Germany.

[9] C. A. Balanis, Antenna Theory, New Jersey: John Wiley & Sons, 2005.

[10] P. A. Zandbergen, PYTHON Scripting for ArcGIS, Redland: Esri Press, 2013.

[11] P.A. Burrough, M.F.Goodchild, R.A. McDonnell, P. Switzer, M. Worboys, "Principles of geographical information systems," Oxford University press, Great Clarendon Street, Oxford ox2 6DP, Oxford New York 2000.

Chapter 4 Development of empirical model for atmospheric phase screen reduction in extreme weather condition

In this chapter, a new semi-empirical model was proposed to remove the atmospheric phase screen of ground-based synthetic aperture radar (GB-SAR) differential interferometry (DInSAR) in a steep mountainous area with extreme weather condition. In the proposed method based on the model-based statistical technique combined with topographical information. Unlike conventional atmospheric phase compensation methods, the meteorological parameters such as atmospheric temperature, pressure or humidity are not been used in this method. Hence, the model can be used for a minimum number of site information under any atmospheric conditions.

4.1 Atmospheric effect for Ku band GB-SAR

4.1.1 Deferential SAR interferometry

If a scatterer on the ground slightly changes its relative position in the time interval between two complex SAR images (e.g. due to subsidence, landslide, earthquake …etc.), an additive phase term will appear independent of the baseline. This can be quantitatively estimated by the phase difference between two SAR interferograms. This technique is known as Differential Interferometric SAR (DInSAR) which have been developed during last decades, showing their usefulness for monitoring deformation with millimetric precision (Chapter 1). In the GB-SAR, differential phase can be directly translated into an equivalent range displacement or, in another word, in the deformation,

$$\Delta d = -\frac{\lambda}{4\pi} . \arg(I_2. I_1^*) \qquad (4.1)$$

$$\Delta \mathrm{d} = -\frac{\lambda}{4\pi} . \Delta \varphi_{2-1} \qquad (4.2)$$

Differential SAR interferometry works under the coherent condition where the received waveforms correlate in the compared SAR pair. One of the benefits of the GB-SAR sensor is the opportunity to gather zero-baseline repeated scans for differential measurements. Therefore terms usually affecting the differential coherence such as image co-registration approximation, baseline construction uncertainties, and digital elevation model removal residual errors become negligible.

However, in the equation 4.1, we are assuming that the propagation properties of the transmission medium are preserved its homogeneity in the spatial and temporal domain. Then the transmission medium remains same in consecutive acquisitions and Δd can be interpreted as the line-of-sight physical displacement of the target. In the real application, this assumption is no longer preserve due to the presence of atmospheric phase screen and its inhomogeneity [1]-[8].
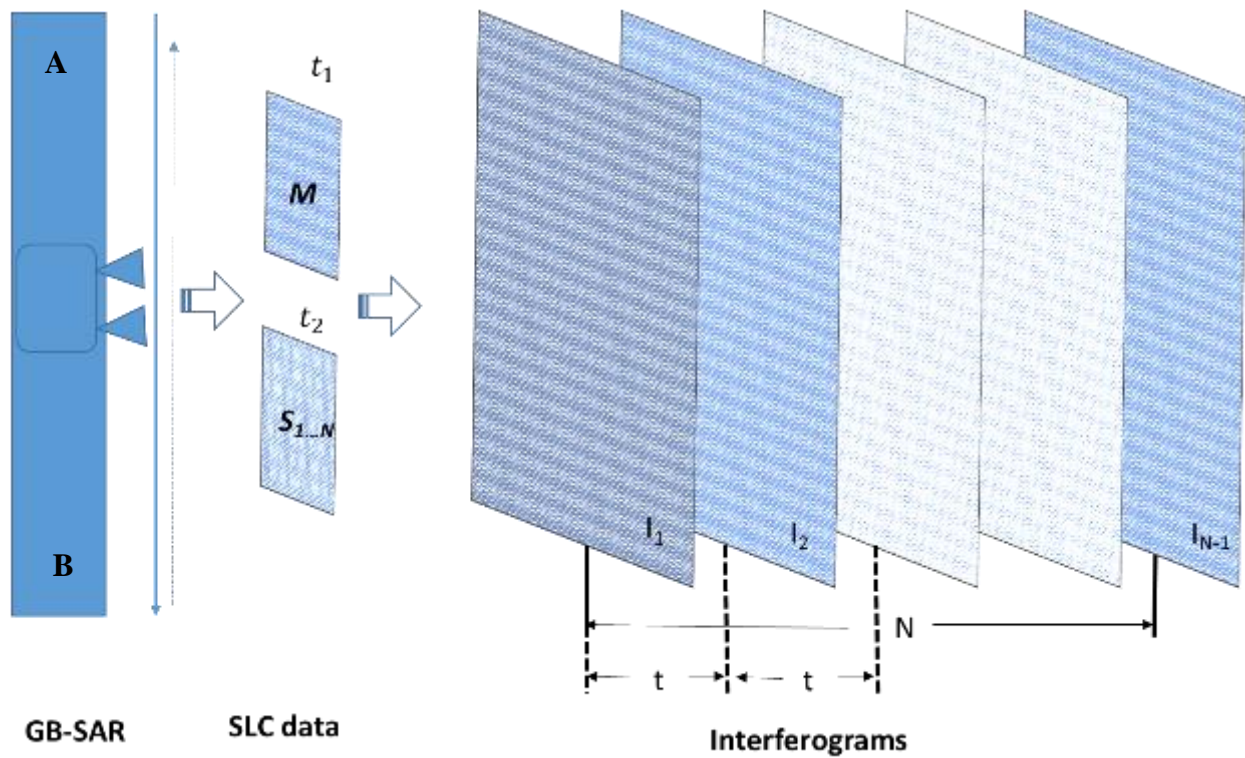
Figure 4.1   Schematic diagram of DInSAR in GB-SAR

Above Figure 4.1 describes the schematic of DInSAR image formation by GB-SAR. The GB-SAR moved on the linear rail as shown in the left-hand side of Figure 4.1 and it completes one scan by moving the sensor A to B for complete one scan. After the one scan is completed, the sensor goes back to its starting position of A by saving the acquired data in control PC. After SAR processing is done [9], this SLC (Single Look Complex) data set was considered as M - Master image and consecutively acquired data set was named as S – Slave image. The phase difference between this master image and slave image generate an interferogram I_1. This process was continuously done by user defined time interval t and each data acquisition $I_1, I_2, I_3, I_4, \ldots \ldots I_{N-1}$ interferogram was generated. The phase information of those interferograms was further processed to estimate the displacement (Chapter 5 and Chapter 6). Figure 4.2 and Figure 4.3 depict the sample data sets acquired from Minami-Aso GB-SAR monitoring site at two different time intervals. In Figure 4.2, the observed weather condition was normal during the data acquisition for Master image in t_1 time and Slave image t_2. The estimated interferograms depict the zero phase change for both near range and far range. But in Figure 4.3, due to the sudden fluctuation of the weather condition during the data acquisition in t_1 time and t_2, the estimated interferograms depict the different trend in the phase change in near range and far range. This will add phase artifacts for the interferograms. In the GB-SAR terminology, this effect was named as the atmospheric artifacts or atmospheric phase screen which come into existence by several atmospheric parameters.
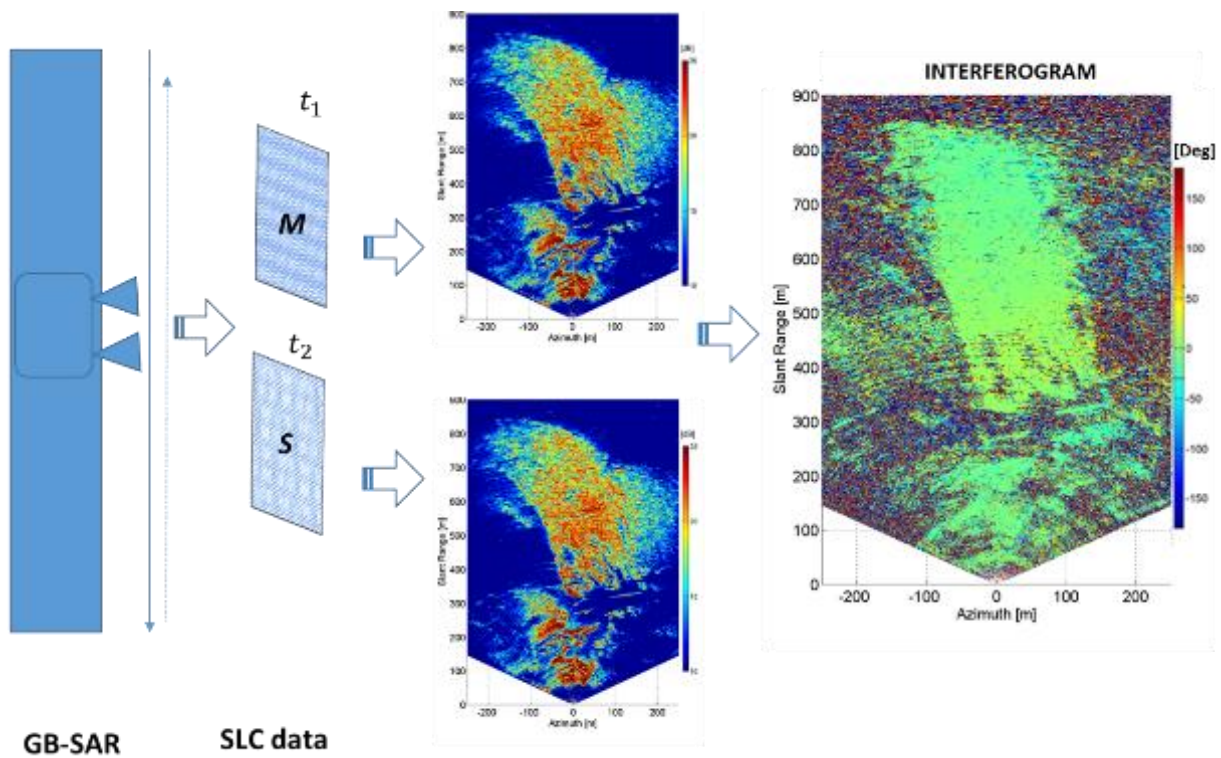
Figure 4.2   DInSAR image in normal weather conditions
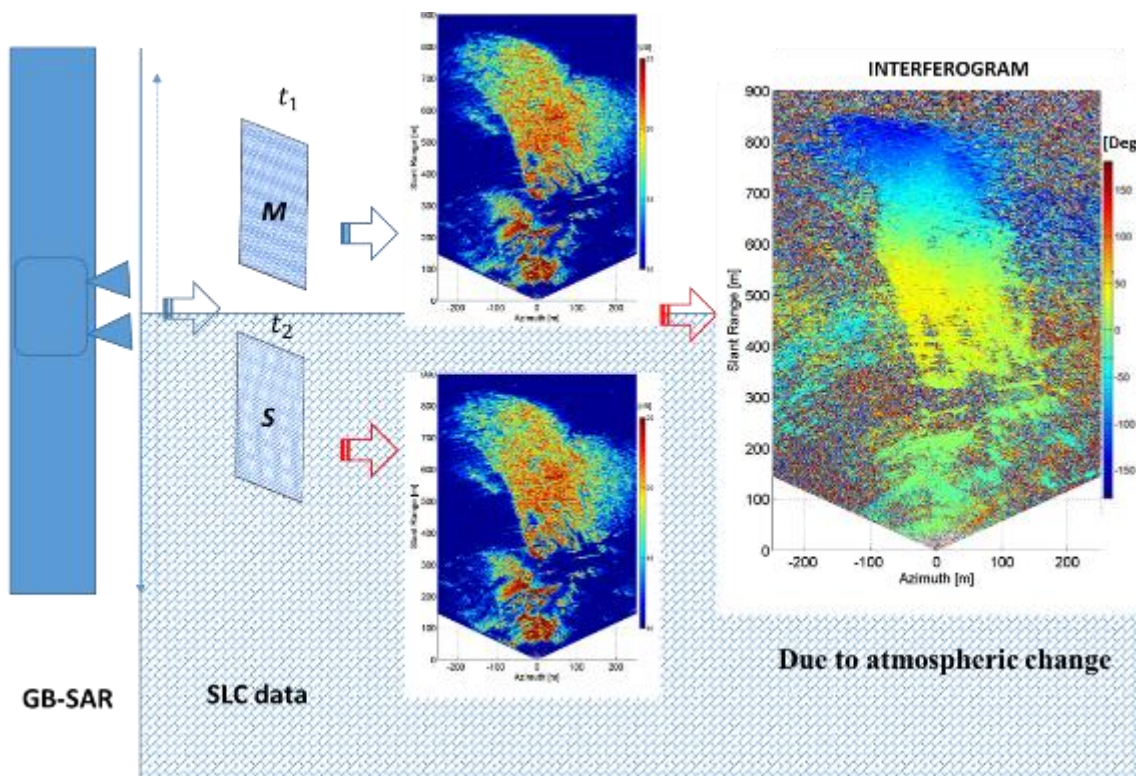
Figure 4.3   DInSAR image in extreme weather conditions

4.1.2 Atmospheric parameter change

(a)

(b)

(c)

(d)
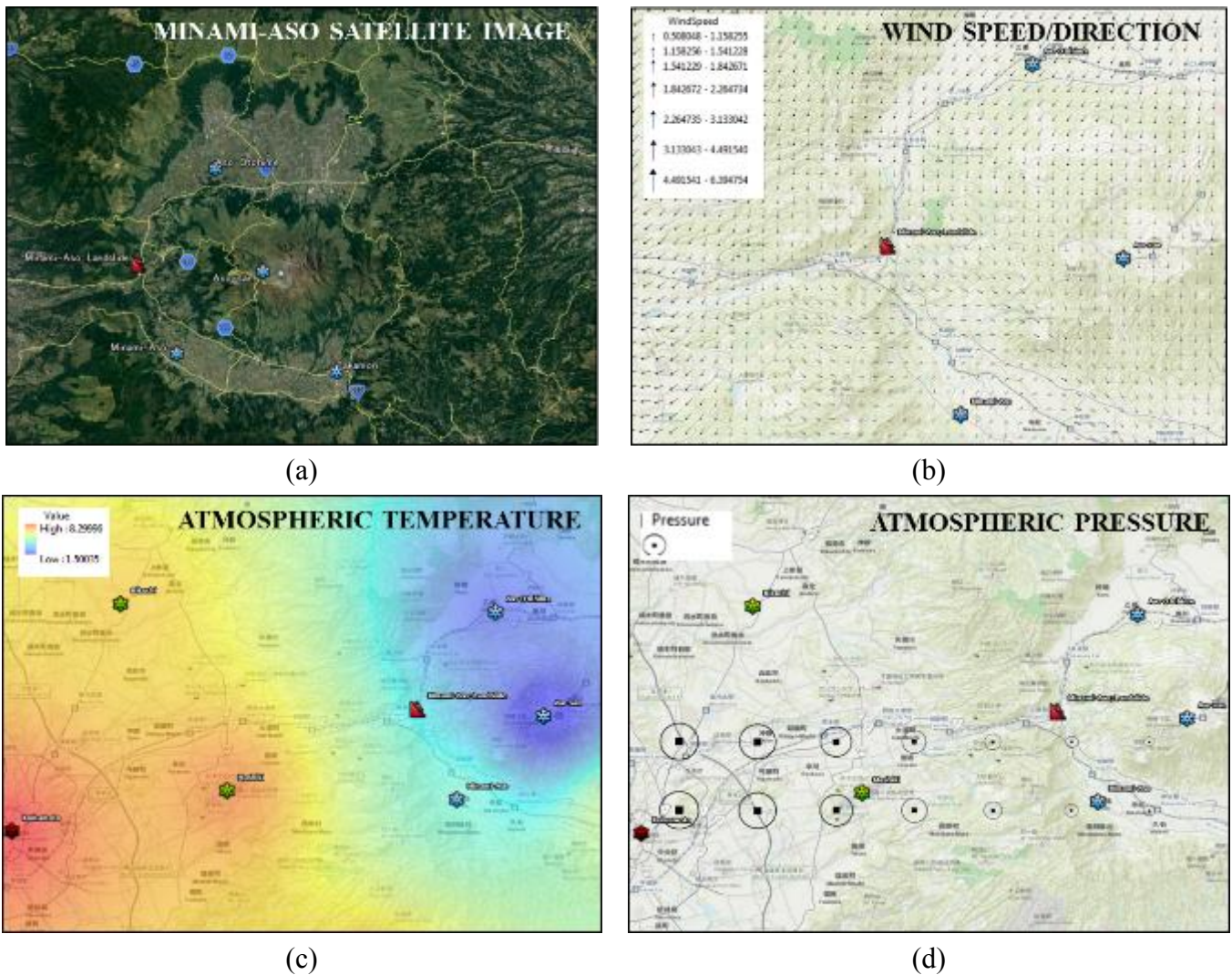
Figure 4.4 The atmospheric parameter distribution

The electromagnetic signal transmitted by the GB-SAR was propagated through the troposphere before reach to its destination. Due to the temporal change of atmospheric parameters such as temperature (T), pressure (P) and relative humidity (H) the propagation velocity through troposphere was rapidly changed. This phenomenon becomes more unstable in mountain regions due to the sudden change of weather conditions. Figure 4.4 (a) shows the GB-SAR installation location which is near to the *Aso caldera*. The system was installed 401 m elevation from mean sea level. The total observation area was located within 900 m of steep terrain up to 815 m elevation. Due to high elevation and surrounding mountain cliffs, sudden fluctuations of metrological parameters were observed. Especially, the due to the continuous wind flow in Figure 4.4 (b) along *Kurokawa river* become a critical factor which governs localized weather condition completely different from weather condition observed in Kumamoto city as shown in Figure 4.4 (c) and Figure 4.4 (d).

4.2 Atmospheric phase screen estimation

4.2.1 Observation of meteorological parameters

(a)

(b)
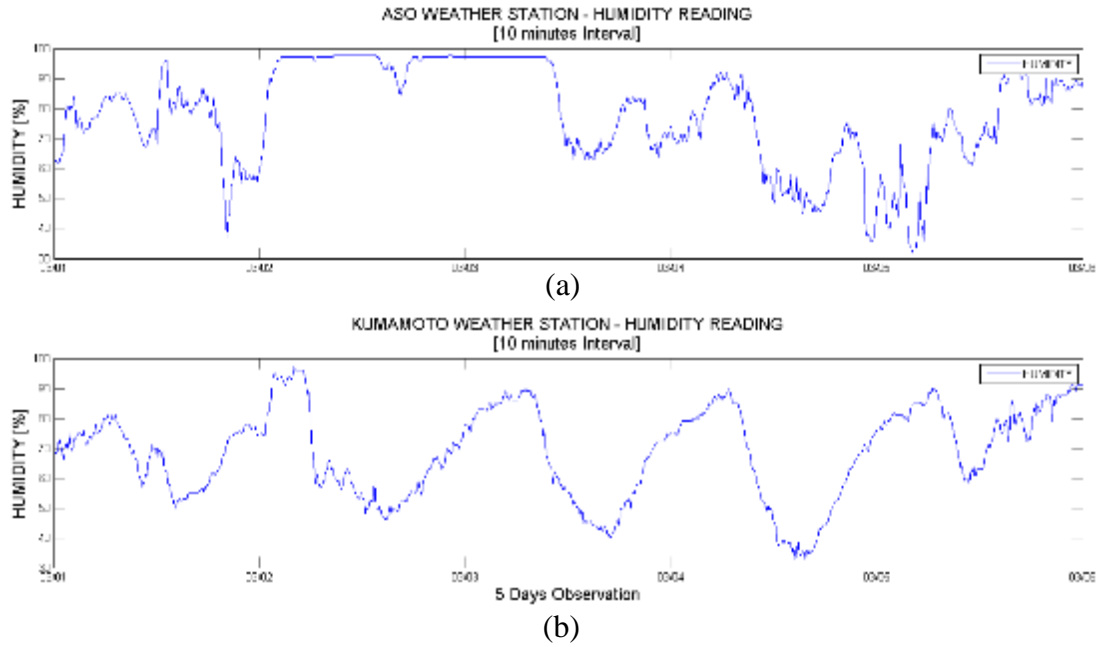
Figure 4.5 Observation of atmospheric humidity fluctustion

(a)

(b)
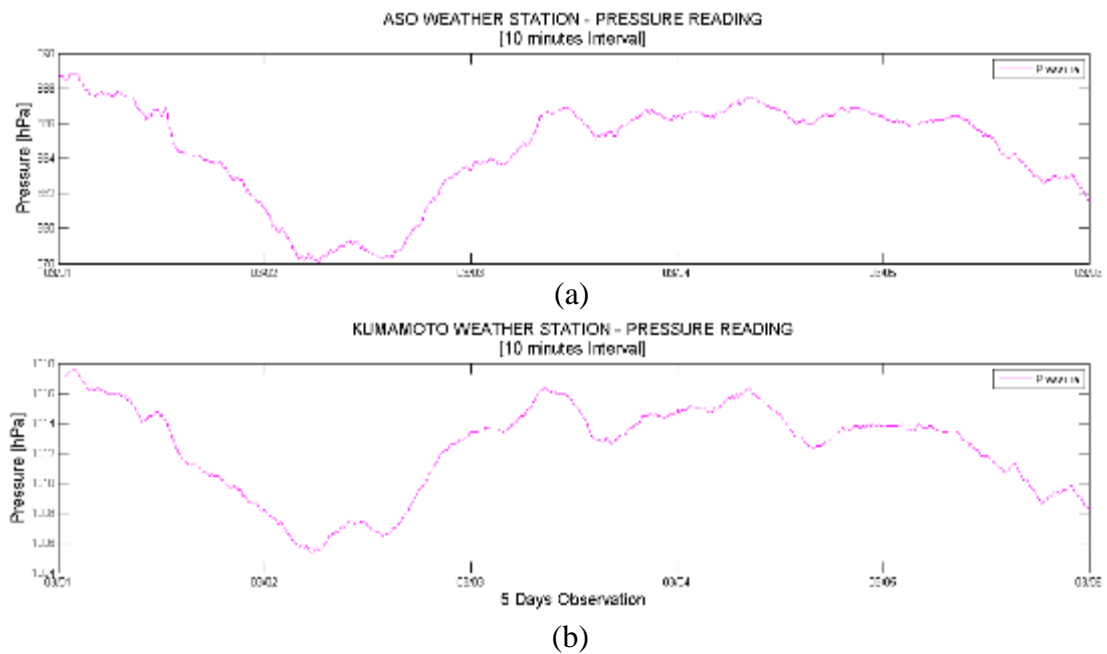
Figure 4.6   Observation of atmospheric pressure fluctustion
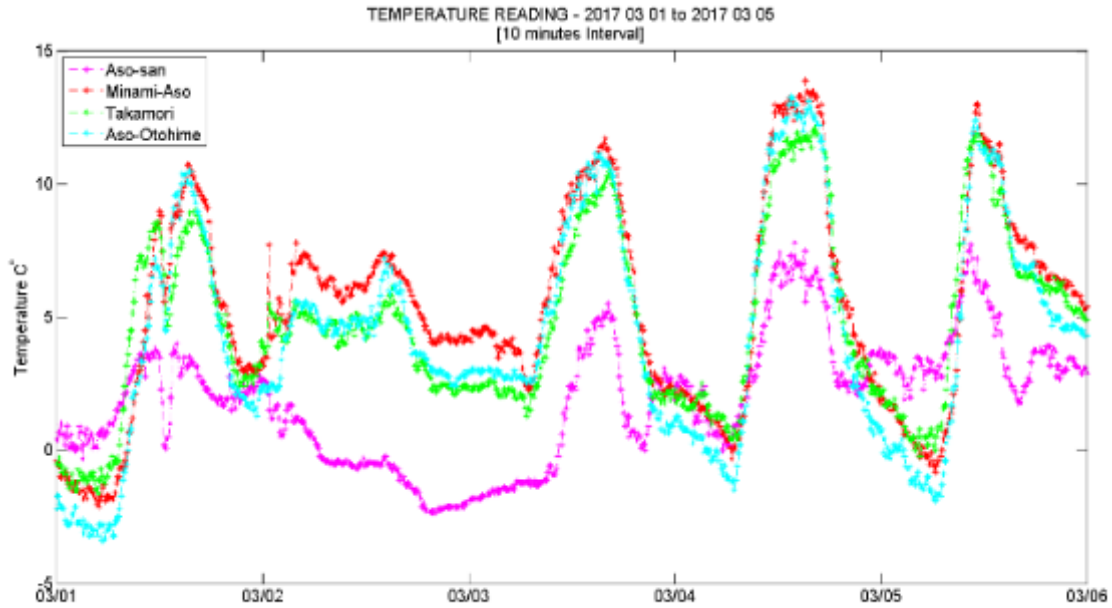
Figure 4.7   Observation of atmospheric temperature fluctustion

The GB-SAR work on Ku band has high sensitivity for the small scale changes in the reflected surface, as well as the temporal changes in the medium. This happened due to the modulation of the velocity of an electromagnetic wave through a propagation medium by the refractive index n. In GB-SAR case, the medium is the troposphere, so that the *n* could be estimated by any mathematical model, which could attune with the trend observed by the experimental results. In the GB-SAR installation location in Minami-Aso, heavily suffered from sudden atmospheric fluctuation along time. Figure 4.5, Figure 4.6 and Figure 4.7 shows the atmospheric humidity, pressure and temperature change recorded in meteorological stations near to the GB-SAR experimental site [10]. The Figure 4.5 (a), Figure 4.6 (a) shows the 5 days weather data recorded in every 10 minutes of a time interval in *Kumamoto* and the Figure 4.5 (b), Figure 4.6 (b) in *Aso* volcanic mountain area. Concurrently, the atmospheric temperature fluctuation was shown in Figure 4.7. These fluctuations result in an ambiguity of observed interferometric phase during the GB-SAR observation. This can be estimated by calculating the change of refractive index *n* [11]-[16], along the GB-SAR observation time. Thereby the estimated *n* can use to evaluate phase change due to atmospheric artifact and deduct in order to estimate the real displacement.

4.2.2 Atmospheric phase screen estimation

The phase compensation by metrological observation become a more popular approach for artifacts removal which based on the reflective index [7] [17] during the observation period. An electromagnetic wave is affected by atmosphere both on phase and amplitude. Especially phase shift caused by the atmosphere is a more serious problem for GB-SAR interferometry. As for amplitude term, attenuation factor [dB/km] is a function of pressure P [hPa], temperature T [K] humidity and radar frequency, and mainly caused by fog and vapor in the air. If the atmospheric conditions are $P = 1013hPa$, $T = 288.15K$, the attenuation factor for frequency below 57 GHz for oxygen A_{o_2} and water vapor A_{H_2o} are expressed as [18],

$$A_{o_2} = \left[7.19 \times 10^{-3} + \frac{6.09}{f^2 + 0.227} + \frac{4.81}{(f - 57)^2 + 1.5} \right] f^2 \times 10^{-3} \qquad (4.3)$$

$$A_{H_2o} = \left[0.050 + 0.0021\rho + \frac{3.6}{(f-22.2)^2+8.5} + \frac{10.6}{(f-183.3)^2+9.0} + \frac{8.9}{(f-325.4)^2+26.3} \right] f^2 \rho 10^{-4} \qquad (4.4)$$

where ρ is the water vapor concentration and f [GHz] is a radar frequency. The equation 4.3 and 4.4 work when the frequency range is $f \leq 57$ [GHz] and $1 \leq f \leq 350$ [GHz], respectively. Therefore the total attenuation,

$$Atn = A_{o_2} + A_{H_2o} \qquad (4.5)$$

If the water vapor concentration is 7.5g/m3, frequency is 17.2 GHz, attenuation is approximately 0.05dB/km. Therefore this change can be negligible.

The propagation velocity of electromagnetic wave becomes slower due to a change of refraction index n in the atmosphere. The n can be represented as,

$$n = 1 + \frac{K_1 P}{T} + \frac{K_2 e}{T^2} \qquad (4.6)$$

$$e = \frac{H. e_i}{100} \qquad (4.6)$$

where H is a relative humidity, e_i is saturated vapor pressure and $K_1 = 7.76 \times 10^{-5} \left[\frac{K}{Pa} \right]$ and $K_2 = 3.73 \times 10^{-1} \left[\frac{K^2}{Pa} \right]$ are constants.

$$e_i = 6.1121e^{\left[\frac{17.502(T-273.15)}{T-32.18}\right]} \tag{4.7}$$

$$(273.15 \leq T \leq 323.15) \tag{4.8}$$

The equation 4.7 works between -20 ℃ and 50 ℃ [18]. The pressure is dependent on the altitude z expressed as,

$$P = P_0 \left[\frac{T}{T + 6.5z}\right]^{5.2558} \tag{4.9}$$

where P_0 is pressure at sea level. The refractivity n is used,

$$n(t) = n[T(t), P(t), H(t)] \tag{4.10}$$

Thereby the refractivity index can be mathematically calculated by observed meteorological parameters; atmospheric pressure, atmospheric temperature and the humidity. The estimated refractivity index for 1st March to 4th March was shown in the Figure 4.8.
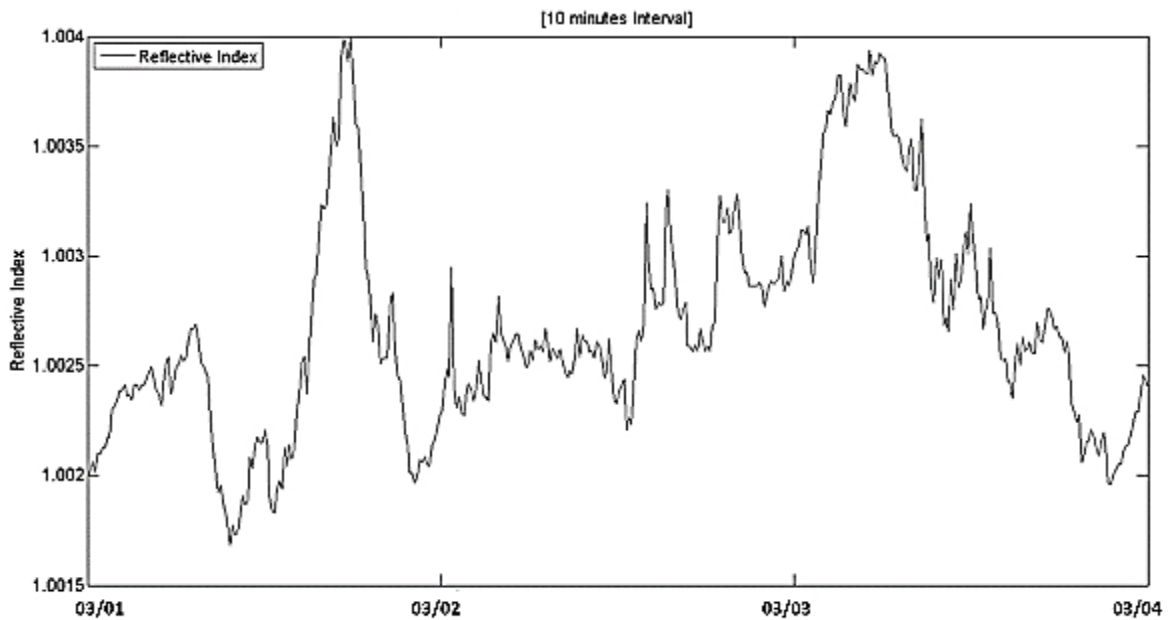
Figure 4.8   Estimated refractivity index
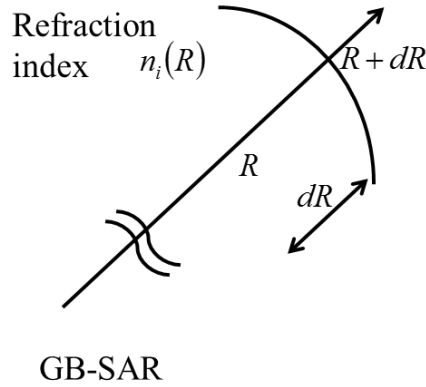
Figure 4.9   The schematic diagram describes the change of the refraction
index along the EM wave propagation direction

Figure 4.9 shows the schematic diagram of the change of the refraction index where the subscript i indicates the time index, r is a distance from the radar. If we divided into thin layer having the width of dr along the direction of r, the phase term of electromagnetic waves propagating the atmosphere can be expressed as,

$$d\varphi_i = 2k \cdot dr = 2\frac{2\pi f_c}{c/n_i(r)} \cdot dr = \frac{4\pi f_c}{c}n_i(r) \cdot dr \qquad (4.11)$$

where k is wavenumber f_c is center frequency, c is the speed of light in vacuum, n_i is a refraction index of the atmosphere,

$$\varphi_i(r) = \frac{4\pi f_c}{c}\int n_i(r)dr \approx \frac{4\pi f_c n_i}{c}\int dr = \frac{4\pi f_c r}{c}n_i \qquad (4.12)$$

Therefore phase shift in an interferogram $\Delta\varphi$ can be expressed as following formula [5],

$$\Delta\varphi(r) = \varphi_2(r) - \varphi_1(r) = \frac{4\pi f_c r}{c}(n_2 - n_1) = \frac{4\pi f_c r}{c}\Delta n \qquad (4.13)$$

Thus $\Delta\varphi$ is linear with r, respect to the distance if $\Delta\varphi$ is caused only by change with n. However,

this model (equation) only be valid with the assumption of the atmosphere is homogeneous with respect to the position in range the direction. This means that the pressure, temperature and humidity should be uniformly changed over the scene. But this is not true in real world scenario. As a result, the estimated displacement would miscellaneous and the results become inaccurate. It also leads to have the problem of phase wrapping is one of the main issue observed in long range SAR interferograms.

4.2.3 Conventional method for atmospheric phase screen compensation

Some models are proposed to compensate the atmospheric effect [3]-[8]. In this attempt, we have testified the linear phase model [7] and is assumed in order to make signal processing simple in the real time monitoring system. The linear phase model is expressed as,

$$\Delta\varphi(r) = \alpha \cdot r_i \tag{4.15}$$

We estimate the α using least mean square method. In order to correct the atmospheric effect on phase, we need to extract the coherent scatterer (CS) from the SAR images. The methods to select the CSs are discussed in Chapter 5. Using the phase information of CS's pixels, we estimate a regression line for phase shift correction. At first we assume one liner model with the gradient α and then by minimizing 4.16, we get optimum regression line,

$$\alpha_{min} = min\left(\sum_N [arg(exp[j\alpha \cdot r]) - arg(exp[j(\Delta\varphi)])]^2\right) \tag{4.16}$$

where N is an index of the pixels. The interferometric phase after the correction $\Delta\varphi_c$ can be expressed as,

$$\Delta\varphi_c = arg\left(e^{j(\Delta\varphi - (\alpha_{min}\cdot r))}\right) \tag{4.17}$$

In Figure 4.10 depict the application of above method by the sample data set at Minami-Aso GB-SAR monitoring site. The top right side of Figure 4.10 shows the image was taken which covered the total illumination area by GB-SAR. The left side of Figure shows the estimated interferogram. At the moment, linear phase change can be observed in range direction as described in Figure 4.9. It adds additional phase to the interferograms, both near range and far range. This can further analyze by selecting the coherent scatterer which distributes along the range direction L1-L6. In this sample data set, the estimated phase of the coherent scatterer shows the phase gradient from 0° to 100° along 0 to 900 m in the range direction. This phase change can be modelled by conventional atmospheric phase screen removal method explain in equation 4.16 and 4.17. The estimated phase gradient of each data acquisition can be used to remove the range phase effect from entire DInSAR image as a simultaneous process of real time monitoring. Figure 4.11 depicts the interferogram after removing the atmospheric phase screen. Moreover, the corresponding phase of the coherent scatterer was shown in Figure 4.11 range-phase plot. After the atmospheric phase removal, the total illumination area shows the zero phase change along the range direction. Figure 4.12 -Figure 4.15 show the observed phase change in negative and positive phase gradient in different data samples and corresponding phase compensation results.
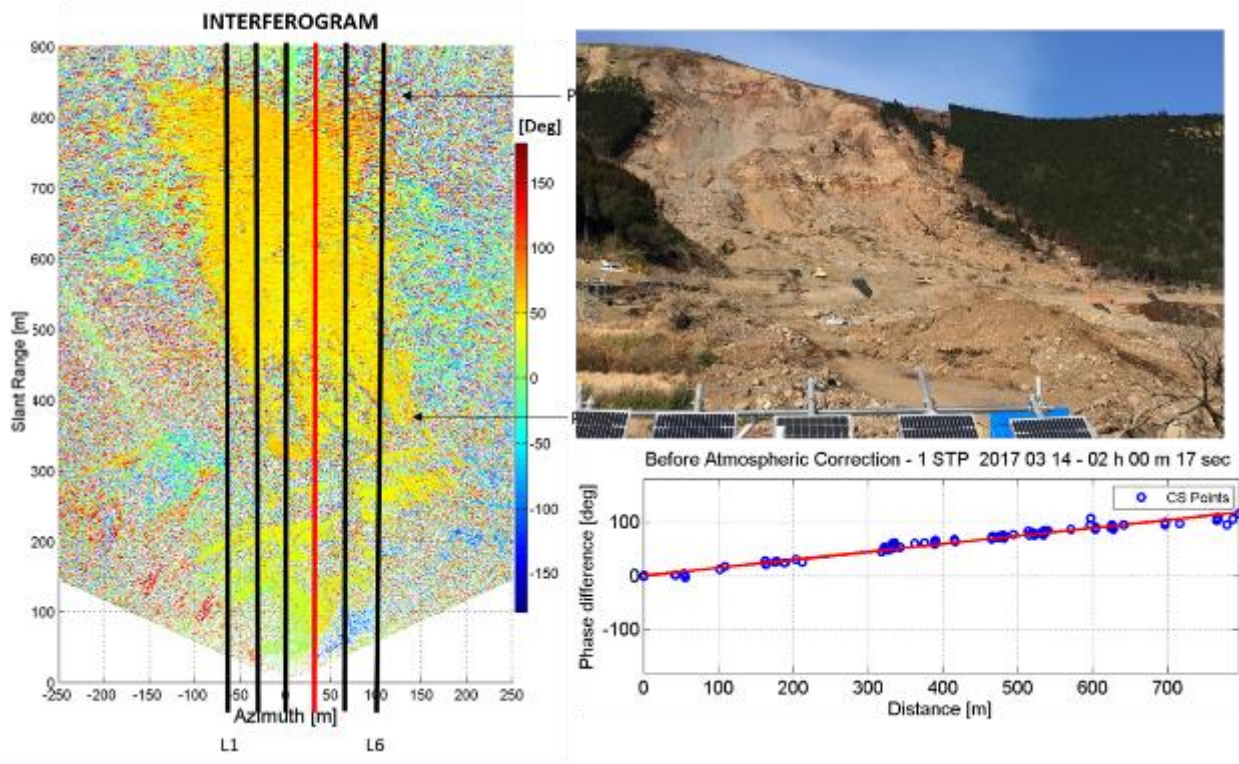
Figure 4.10　DInSAR image in extreme weather conditions
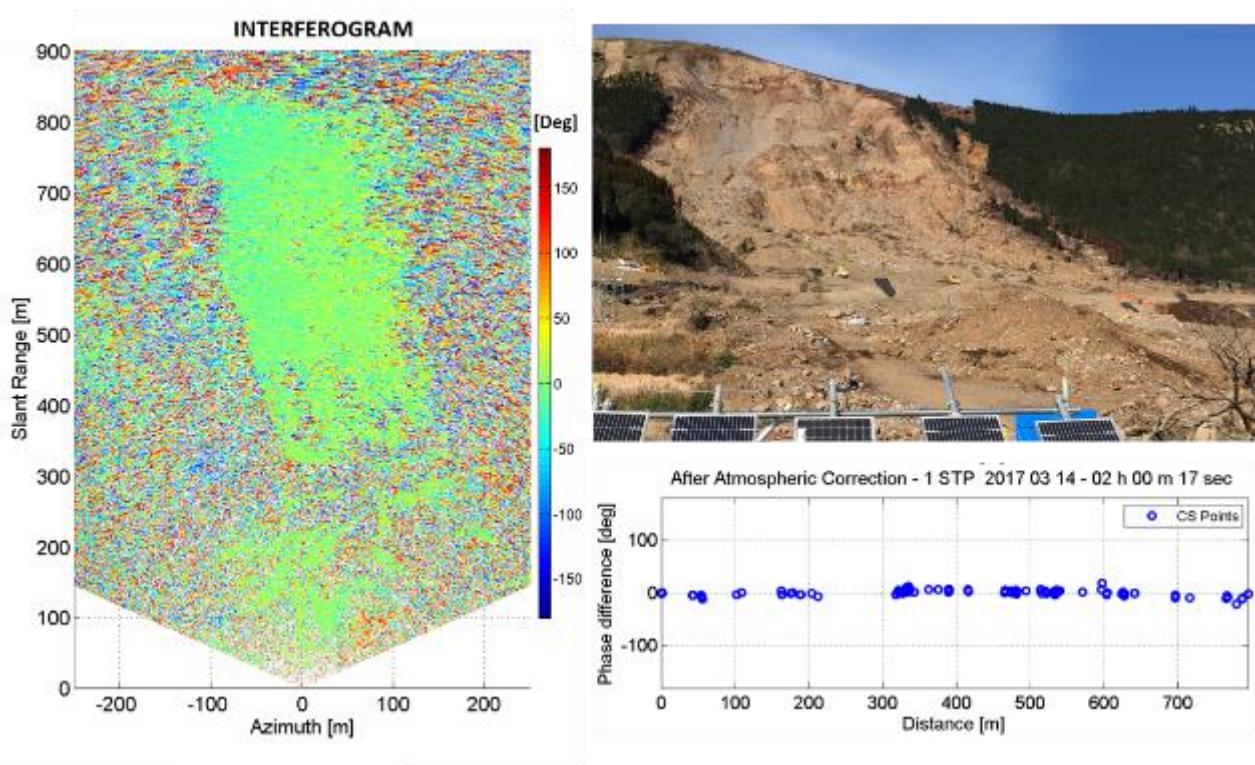
Figure 4.11　DInSAR image in extreme weather conditions

Figure 4.12 The coherence scatters (CS) phase change due to atmospheric artifact was represented. (a) Observed phase change at 13:30 along range direction with the linear regression model (b) Observed phase change at 13:45 along range direction with the linear regression model (c) and (d) shows the corresponding phase after applying the conventional atmospheric phase compensation model.

Figure 4.13 The coherence scatters (CS) phase change due to atmospheric artifact was represented. (a) Observed phase change at 15:00 along range direction with the linear regression model (b) Observed phase change at 15:15 along range direction with the linear regression model (c) and (d) shows the corresponding phase after applying the conventional atmospheric phase compensation model.

Figure 4.14 The coherence scatters (CS) phase change due to atmospheric artifact was represented. (a) Observed phase change at 16:30 along range direction with the linear regression model (b) Observed phase change at 16:45 along range direction with the linear regression model (c) and (d) shows the corresponding phase after applying the conventional atmospheric phase compensation model.

Figure 4.15 The coherence scatters (CS) phase change due to atmospheric artifact was represented. (a) Observed phase change at 07:15 along range direction with the linear regression model (b) Observed phase change at 07:30 along range direction with the linear regression model (c) and (d) shows the corresponding phase after applying the conventional atmospheric phase compensation model.

4.2.4   Atmospheric phase screen due to extreme weather condition

(a)

(b)

(c)

(d)

(e)

(f)
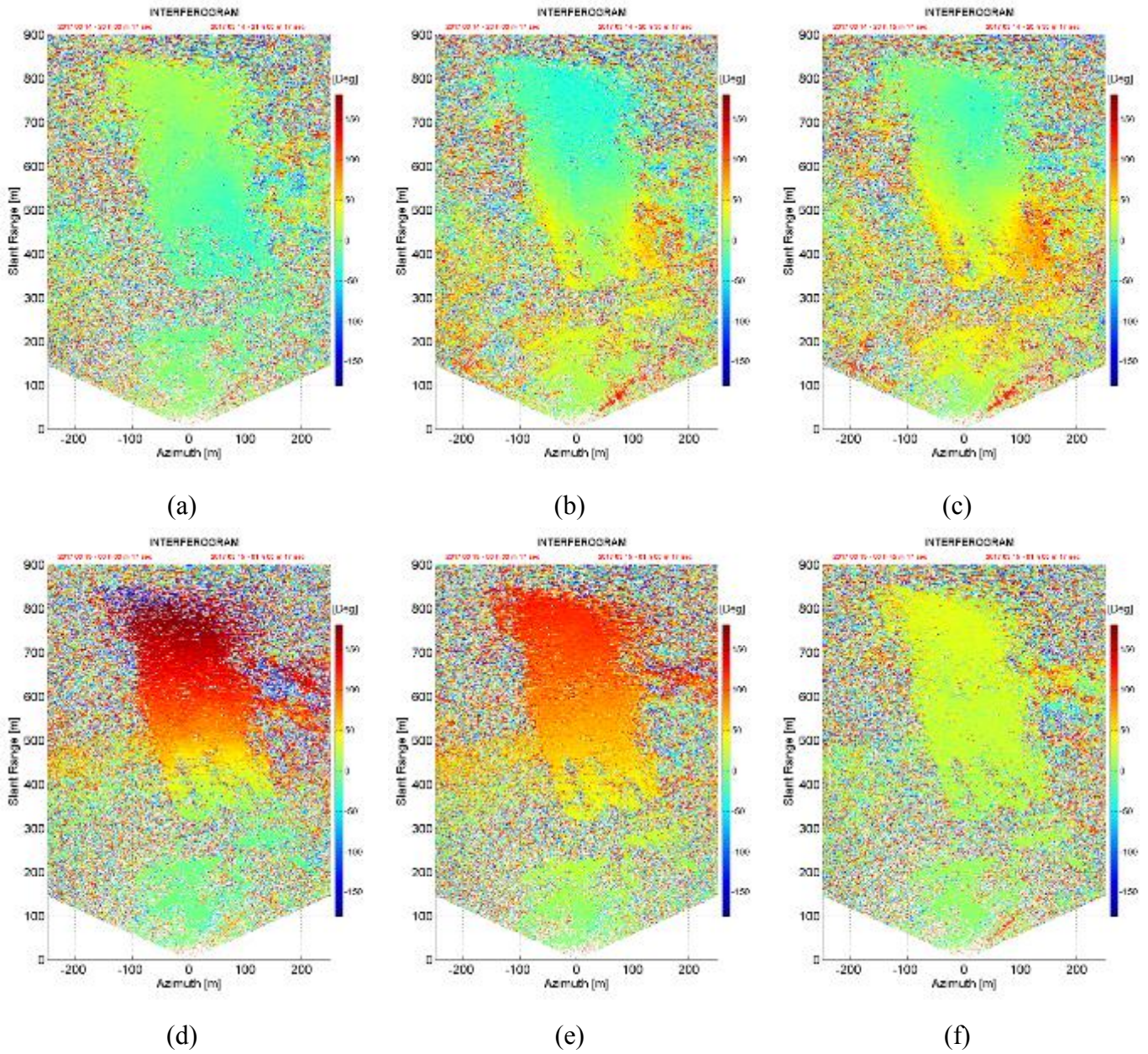
Figure 4.16 The interferometric phase change due to atmospheric artifact was represented. (a)   The interferometric phase of 1 hour time interval. (b) 30 min. (c) 15 min. Differential phase due to inhomogeneity of the troposphere. After 3 hours in the same day (d) Interferometric phase of 1 hour interval. (e) 30 minutes and (f) 15 minutes time intervals.

In this test site location, the temporal decorrelation becomes a significant problem due to the frequent fluctuation of atmospheric condition. Figure 4.16 depicts the differential interferometric SAR images estimated by changing the temporal base line. It shows that the atmospheric phase screen and its sudden fluctuation over time become a significant factor which affects for interferometric phase estimation. Figure 4.16 (a) shows the estimated interferometric phase in 1 hour data acquisition interval and Figure

4.16 (b) and (c) shows the interferometric phase change due to atmospheric phase screen variation during 30 minutes and 15 minutes short data accusation interval. After 3 hours, the estimated interferometric phase was completely changed and was severely suffered due to change of atmospheric condition. Figure 4.16 (d), (e) and (f), the interferometric phase in range direction show higher dispersion during 1 hour time interval and it became minimum in short temporal base line. The interferograms show that the area between $300-900$ m in the range direction has higher phase gradient than area less than 300 m.

The major affection of atmospheric phase fluctuation is observed mainly due to the presence of steep topography which was created after the landslide. Moreover, the atmospheric condition shows the non-linear inclination in phase gradient of range direction in interferograms. The area up to 300 m from the slant range direction shows a small inclination to the interferometric phase and area greater than 300 m was heavily suffered from the atmospheric phase screen in range the direction. This observed ambiguous change varies with time due to the extreme weather condition near to the Aso volcanic mountain. It has a clear correlation with the spatial formation, especially due to the elevation profile of the observation area. The atmospheric artifacts removal model correlated with the spatial information need to be developed for the atmospheric phase compensation.

The GB-SAR employs the interferometric principle in order to measure the changes on target from a distance, the atmospheric correction is a crucial factor for retrieve reliable information in two-dimensional images. The number of correction methods were proposed [3]-[8] and they mainly rely on the response of coherent scatters (CS). If the CSs are known in a scene, the atmospheric correction can be performed by correcting the response of CS. In the beginning of this campaign, the CS are not known and they have to be selected from acquired SAR processed image of the observed terrain. In a conventional method [7], CSs are selected by estimating dispersion index, which quantifies the variation of amplitude through a number of images taken at different lapse time and obtained as;

$$D_{m,n} = \frac{\sigma_{m,n}}{A_{m,n}} \tag{4.14}$$

where $\sigma_{m,n}$ is the standard deviation and $A_{m,n}$ is mean of amplitude with respect to the lapse time at pixel *(m, n)* respectively. The Minami-Aso GB-SAR was heading to the soil surface eroded after the landslide and the newly exposed mountain cliff. The most of the scatter which has the minimum dispersion index was lain in this area and was located along the range direction. The pixel values used in the conventional amplitude dispersion method calculates the consistency of the real-valued amplitude. The phase was sensitively influenced by changes of atmospheric condition.

The high coherency scatters and their range position was shown in the range phase diagrams depicted in Figure 4.17 to 4.20 in different data samples on 14th to 19th March 2017. Figure 4.17 (a), 4.18 (a) data samples were selected in data sets acquired during the night time in consecutive days. Figure 4.20 (a) and (b) data samples were selected in data sets acquired during the night time in the same day. Also, Figure 4.17 (b), 4.18 (b) data samples were selected in data sets acquired during the morning in the consecutive days. Figure 4.19 (a) and (b) data samples were selected in data sets acquired during the morning in a same day. But each and every coherent scatterer phase show the highly random phase change in the morning and the night time. It depicts that the temporal phase change becomes more dynamic in the spatial and the temporal domains.

4.2.3 Inaccuracy of conventional atmospheric phase compensation method in extreme weather condition

The conventional model which describes in the section 4.2.3 was applied to the coherent scatterer in the second data sample and the results were depicted in Figure 4.17 to 4.20 (c) and (d) plots. The results depict that the conventional linear phase compensation model gives large phase error for the coherent scatterer which reclines in near distance between 100 to 400 m and the far distance 500 to 800 m. Furthermore, it shows higher deviation from the estimated regression line which could not be applied for the real-time continuous data processing in GB-SAR.

In this conventional atmospheric phase removal process consists of a linear phase ramp over the range axis, which could be estimated through a simple linear regression model. Figure 4.17 (a) and Figure 4.17 (b) shows the phase of the coherent points distributed along range direction with the estimated linear regression line, before the atmospheric correction. Figure 4.17 (c) and 4.17 (d) shows the phase compensated results by the conventional method. Similarly, the Figure 4.18, 4.19 and 4.20 depict the inapplicability of the conventional phase screen removal method for the areas which shows highly fluctuating, unpredictable and extreme weather condition in both day time and night time.

In the scenes with steep topographic variation, fluctuation of atmospheric parameters such as temperature, pressure, and humidity are observed in random directions. Hence, the assumption of spatial homogeneity in a single direction is no longer be applied. As a result, the conventional linear regression model makes phase residual which makes an erroneous estimation for phase compensation. Therefore, the conventional atmospheric phase screen removal method no longer can be used as an atmospheric phase compensation model for extreme weather conditions. Furthermore, new phase compensation model needs to be developed which can be used for both normal weather condition and extreme weather condition for real-time GB-SAR measurements.
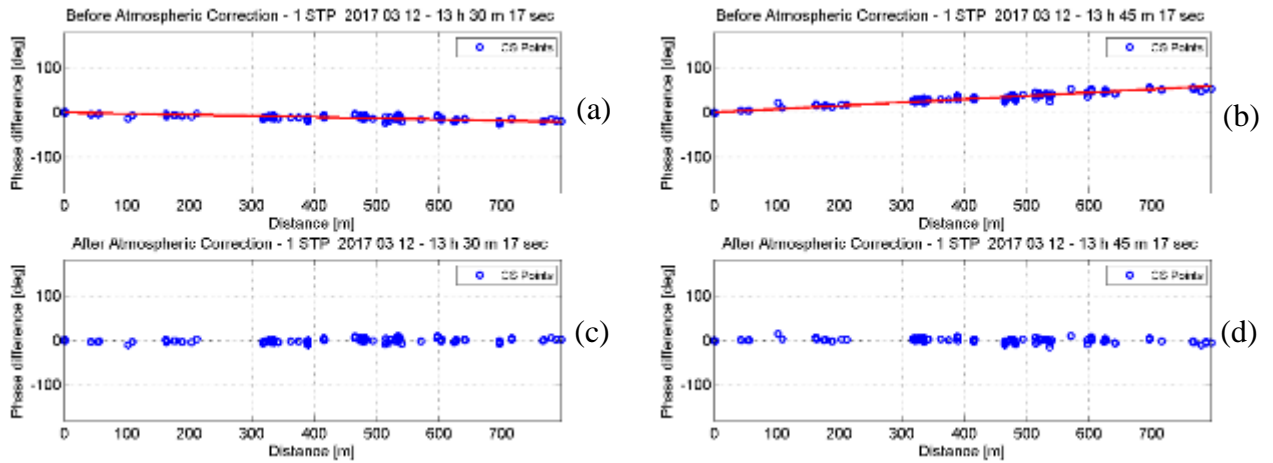
Figure 4.17 The coherence scatters (CS) phase change due to atmospheric artifact was represented. (a) Observed phase change at 20:30 along range direction with the linear regression model (b) Observed phase change at 01:00 along range direction with the linear regression model (c) and (d) shows the corresponding phase after applying the conventional atmospheric phase compensation model.
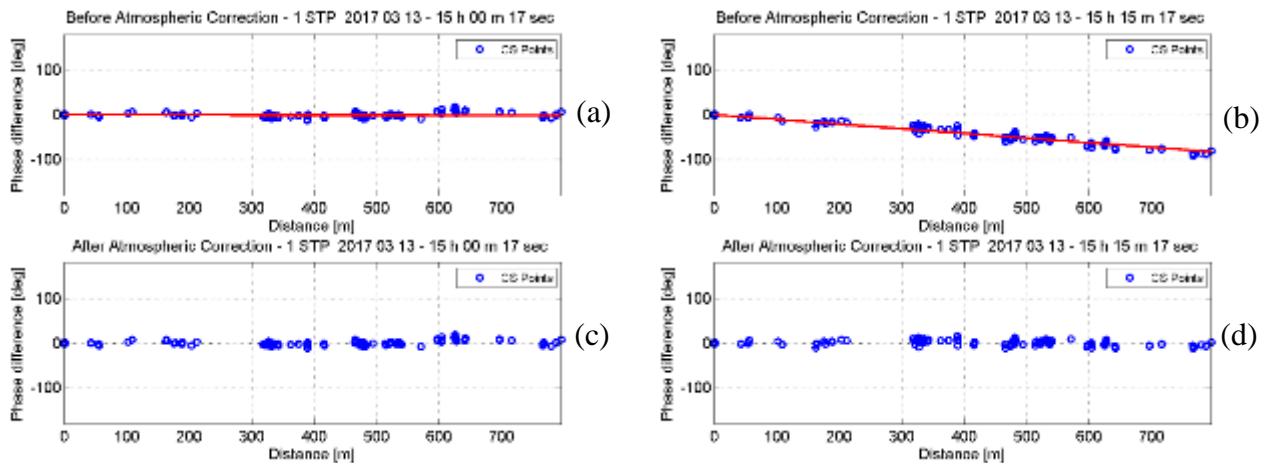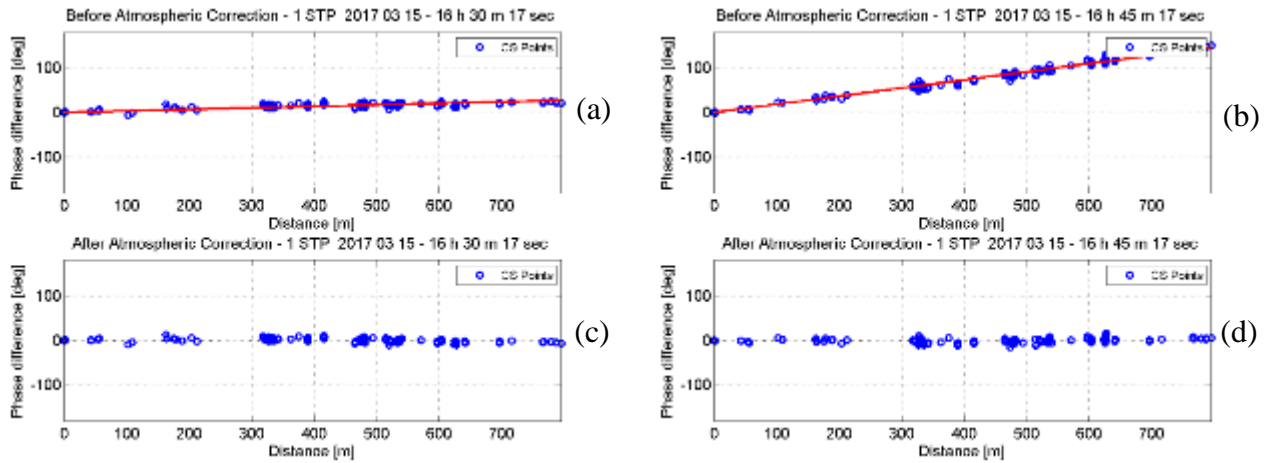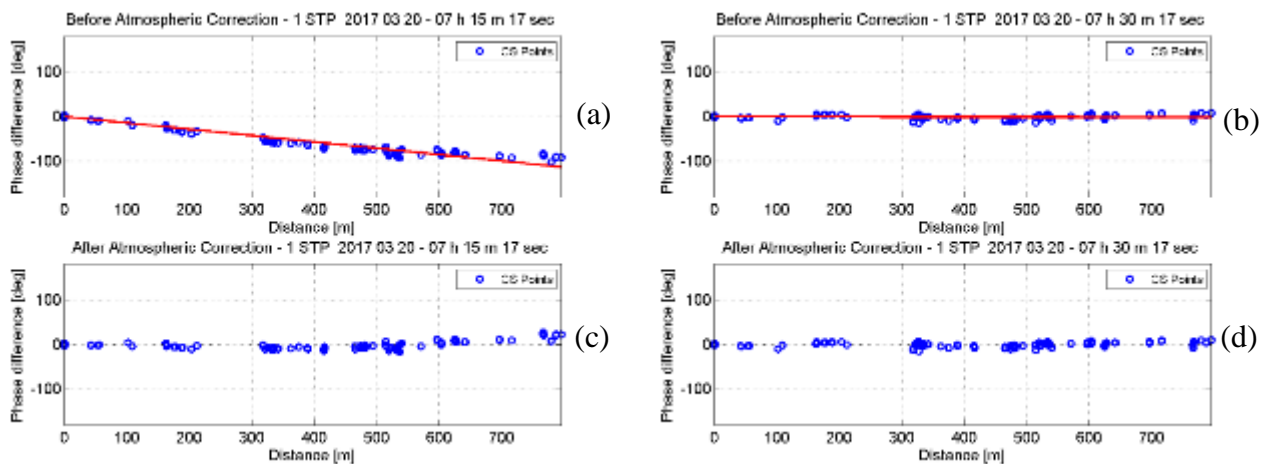

Figure 4.18 The coherence scatters (CS) phase change due to atmospheric artifact was represented. (a) Observed phase change at 20:00 along range direction with the linear regression model (b) Observed phase change at 07:10 in next day morning, along range direction with the linear regression model (c) and (d) shows the corresponding phase after applying the conventional atmospheric phase compensation model.

Figure 4.19 The coherence scatters (CS) phase change due to atmospheric artifact was represented. (a) Observed phase change at 09:15 along range direction with the linear regression model (b) Observed phase change at 09:00 in the next day (after 24 hours) along range direction with the linear regression model (c) and (d) shows the corresponding phase after applying the conventional atmospheric phase compensation model.

Figure 4.20 The coherence scatters (CS) phase change due to atmospheric artifact was represented. (a) Observed phase change at 22:00 along range direction with the linear regression model (b) Observed phase change at 22:15 (after 15 minutes) along range direction with the linear regression model (c) and (d) shows the corresponding phase after applying the conventional atmospheric phase compensation model.

81

4.3 Proposed Two Stage Semi-empirical Algorithm for atmospheric phase compensation

4.3.1 Proposed spatial model
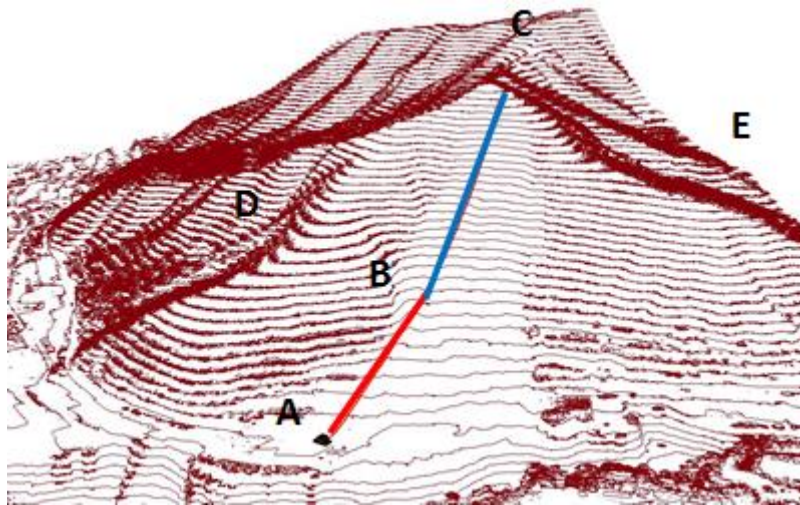
Figure 4.21   This figure shows the 3D terrain model created to assist the spatial dependency of atmospheric phase screen in GB-SAR. The system was installed in location A, heading to the mountain peak

Figure 4.21 shows the terrain model derived from DEM information of western tip of Aso caldera. The GB-SAR was operated in location A by looking towards the mountain peak C. The 100 m buffer zone from the line AC was surrounded by the open soil layer of the landslide area. The area beside this zone covered with natural tree canopy. The point D and E belong to this unchanged geomorphology. The point D, B and E can be identified as a one elevation layer from the stable flat surface where the system was installed. The GB-SAR observation area can be divided into two stages AB and BC. The system was installed in 402 m from mean see level and the total elevation profile was increased up to 750 m into the mountain peak. The top most area of the mountain was covered by barely vegetated soil surface. After the landslide was triggered, part of this area was eroded and the new geological boundary was created.

The simulation results show that the backscatter radar signal in LOS can be divided into two stages, AB near to the radar and BC in the second stage as shown in Figure 4.22. The AB distance was estimated as 330 m in Figure 4.22 (a) from the radar sensor which has high incidence angle due to the average slope gradient. The BC line has lied on stage 2, which has high surface slope gradient than line AB. It starts from 330 m contour line in Figure 4.22 (b) and extends up to the starting point of the landslide. Due to the steep surface slope and its orientation, this area was illuminated with higher

backscatter than AB. The change of weather condition during different time interval has high influence for interferometric phase.

<div align="center">(a)   (b)</div>
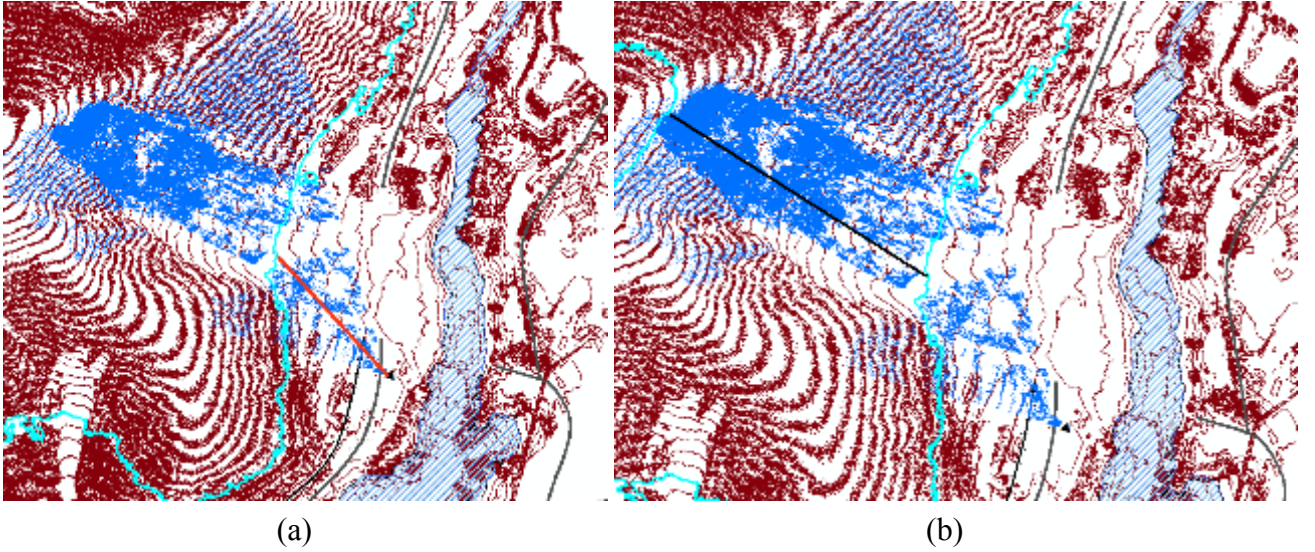
Figure 4.22 (a) shows the 3D terrain model created to assist the spatial dependency of interferometric phase in stage AB (b) shows the 3D terrain model created to assist the spatial dependency of interferometric phase in BC stage.

4.3.1 Proposed method for atmospheric phase removal

The temporal phase change of the CS points within the range of 330 m can be represented in one linear model and the temporal phase change greater than range 330 meters can be represented in another linear model. Therefore total phase change along the slant range direction can be corrected by two stage model. In the proposed model, we divide the phase change into two stages by considering the slant range distance in the elevation plane. Then the model can be rewritten as,

$$\Delta\phi_{i^{th}{corr}} = arg\left\{exp\left[j\int_{1}^{w}(\Delta\varphi - y_1)\right] + exp\left[j\int_{w}^{n}(\Delta\varphi - y_2)\right]\right\} \qquad (4.18)$$

whereas $\Delta\phi$ is the interferometric phase affected due to the atmospheric change y_1 and y_2 are the estimated phase gradient over the slant range direction in i^{th} data acquisition.

$$y_1 = a_1 r + c_1; \quad r < w \qquad (4.19)$$

$$y_2 = a_2 r + c_2; \quad r > w \qquad (4.20)$$

y represents the two stage function which bound on A to B and B to C, in radar LOS. The constant a_1, c_1 and a_2, c_2 was estimated in each interferogram by the piecewise linear regression model.
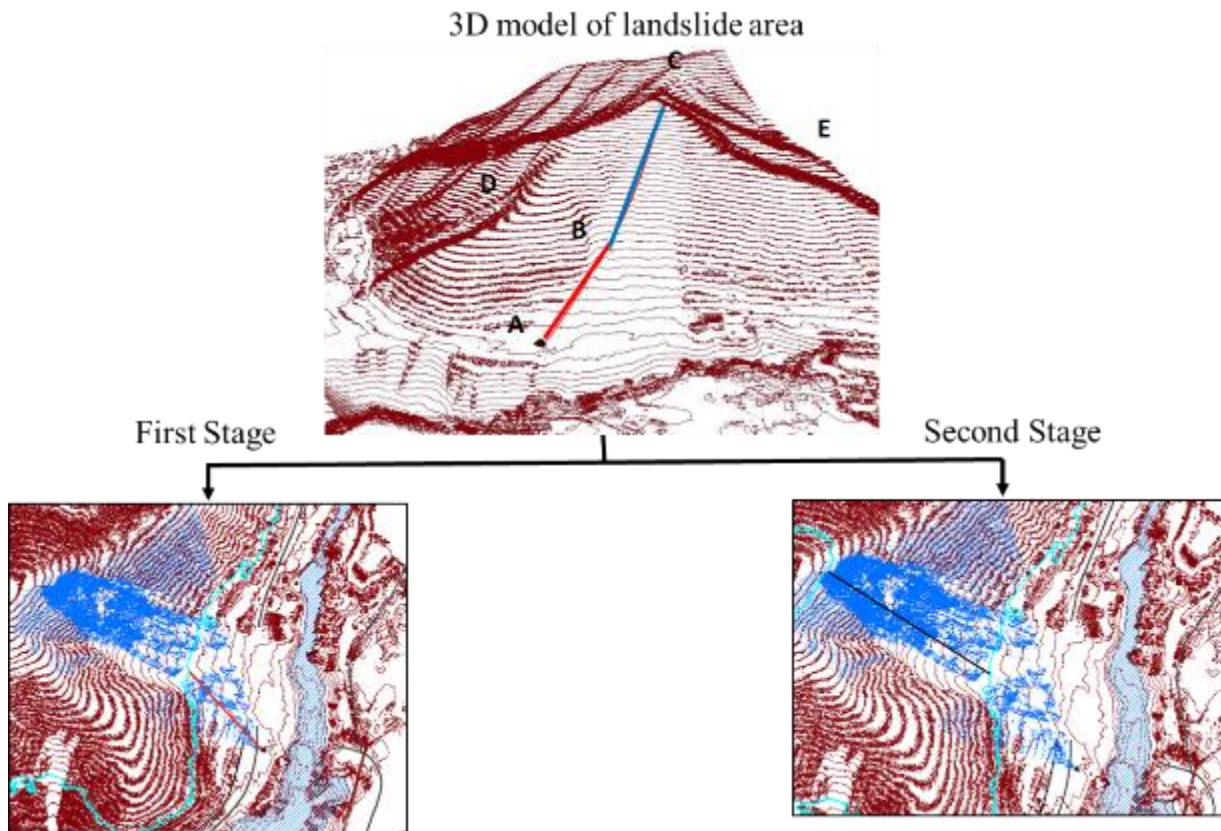
Figure 4.23   The proposed spatial model for atmospheric phase screen estimation

The piecewise linear regression model can be divided into First stage and Second stage as shown in Figure 4.23. Thereby the corresponding constant values can be estimated by,

$$y_i = \sum_{k=0}^{N} a_k r_{k_i} + c_i \qquad (4.21)$$

whereas a_k is the regression coefficient and c_i is the coefficient for the intercept in linear regression model. Due to the temporal change of APS, the regression coefficient shows higher fluctuation, which can be distinguished for each elevation stages. The phase gradient was estimated in each stage along range direction in order to remove the atmospheric phase screen from each interferogram. Moreover, this technique further appropriated for normal weather conditions, which the regression coefficient coincide with each other to setup a linear model. Therefor proposed model can be used for extreme weather condition, and also applicable for normal weather condition of the observation area for remote monitoring.

4.3.2 Application and validation

Figure 4.15 (a) and (b) illustrate the range phase diagram of CS points by applying TSSA. This dynamic model shows the better performance by giving the best fitting for phase diagram. Figure 4.15 (c) and (d) illustrate the CS points after performing the atmospheric compensation by proposed TSSA.
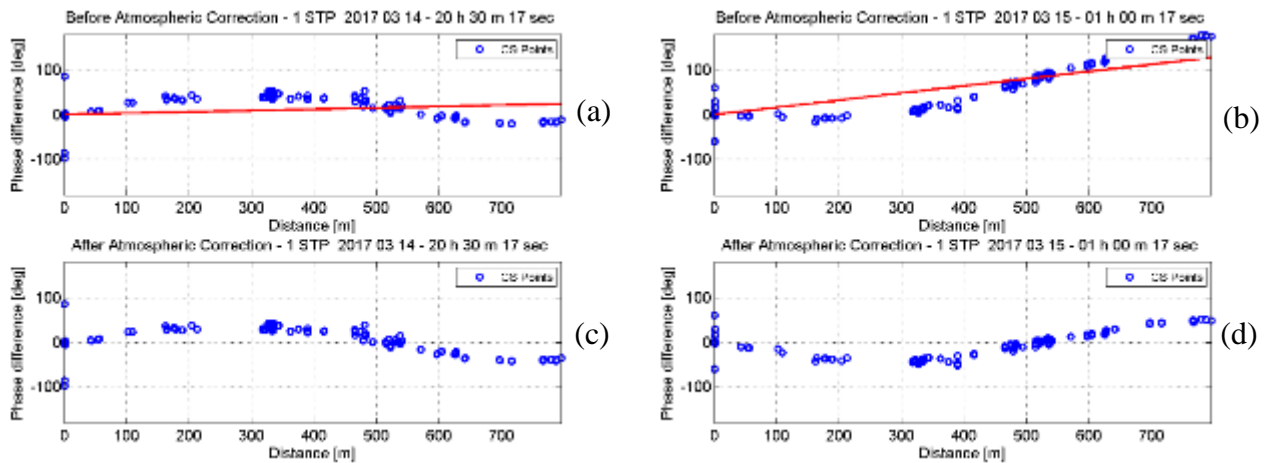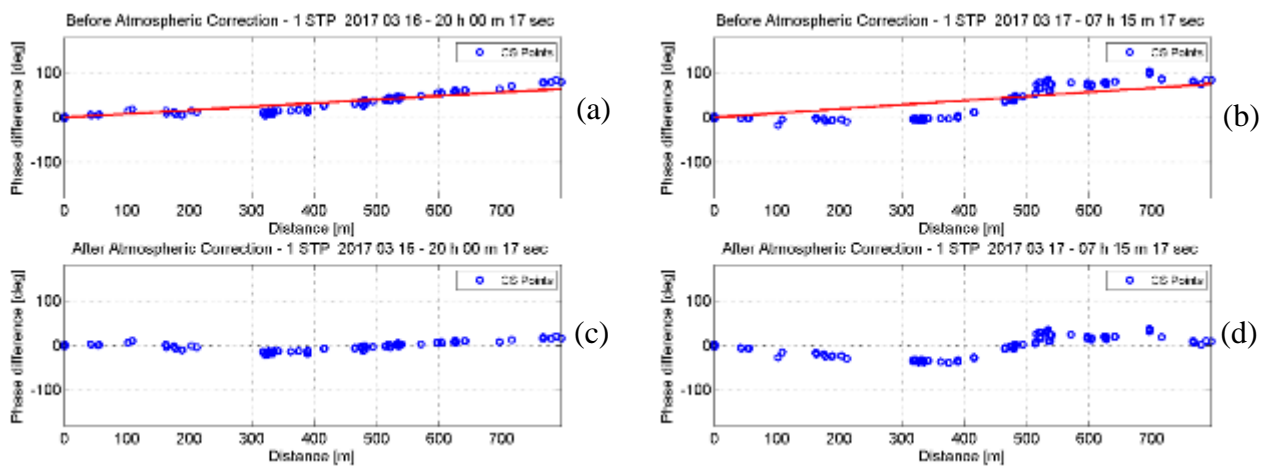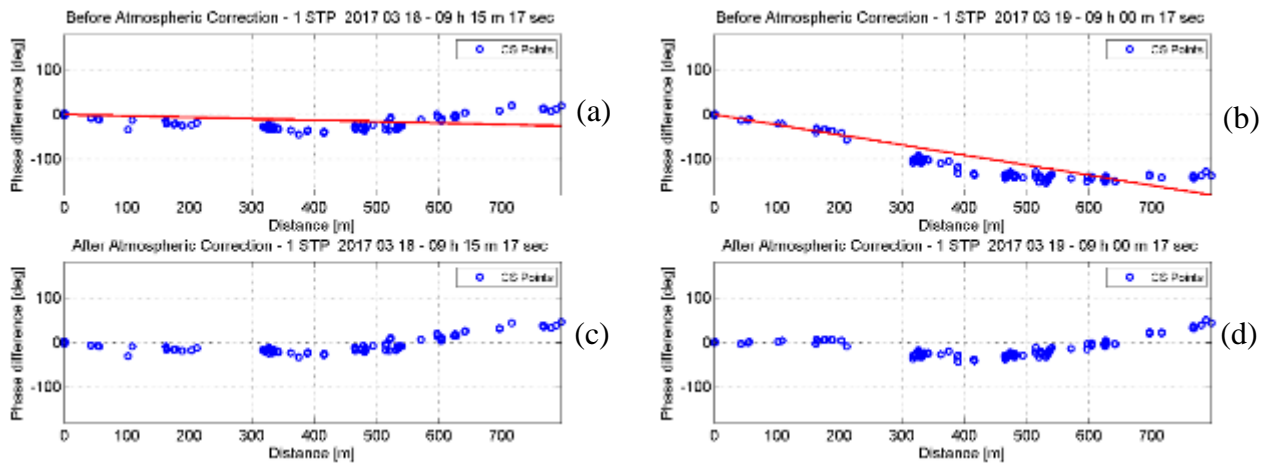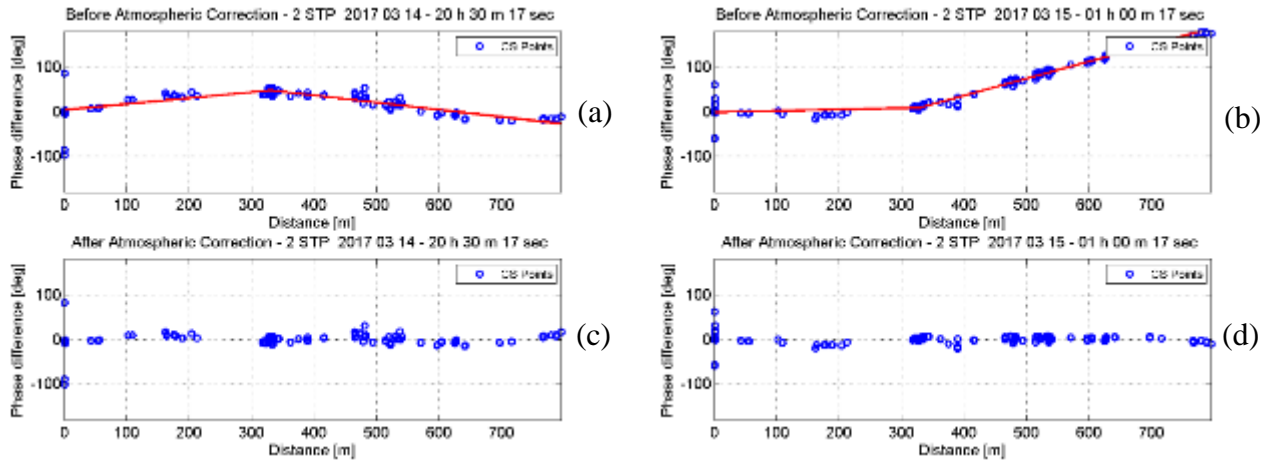

Figure 4.24 The coherence scatters (CS) phase change due to atmospheric artifact was represented. (a) Observed phase change at 20:30 along range direction with proposed model (b) Observed phase change at 01:00 along range direction with the proposed model (c) and (d) shows the corresponding phase after applying the TSSA for atmospheric phase compensation.
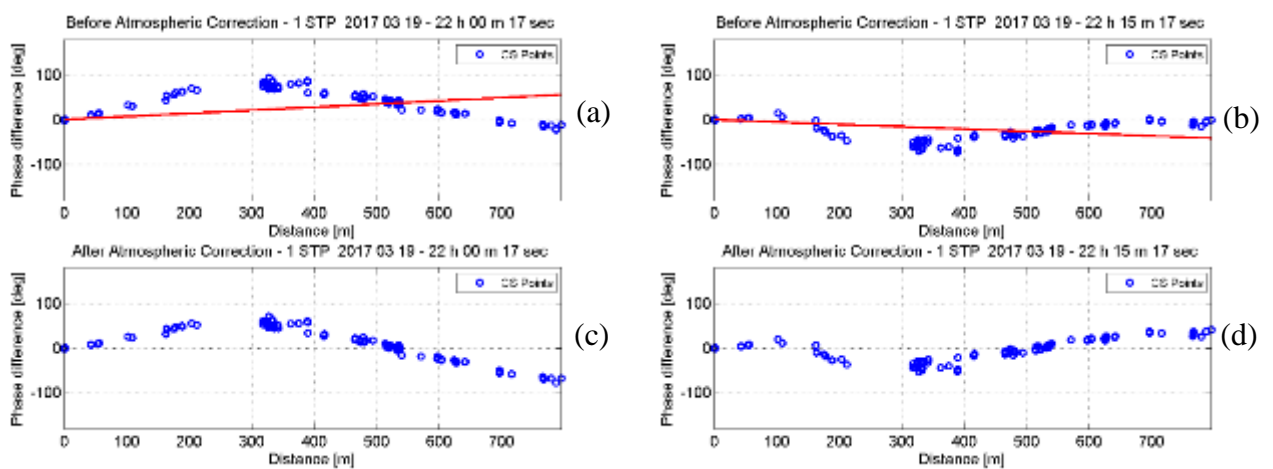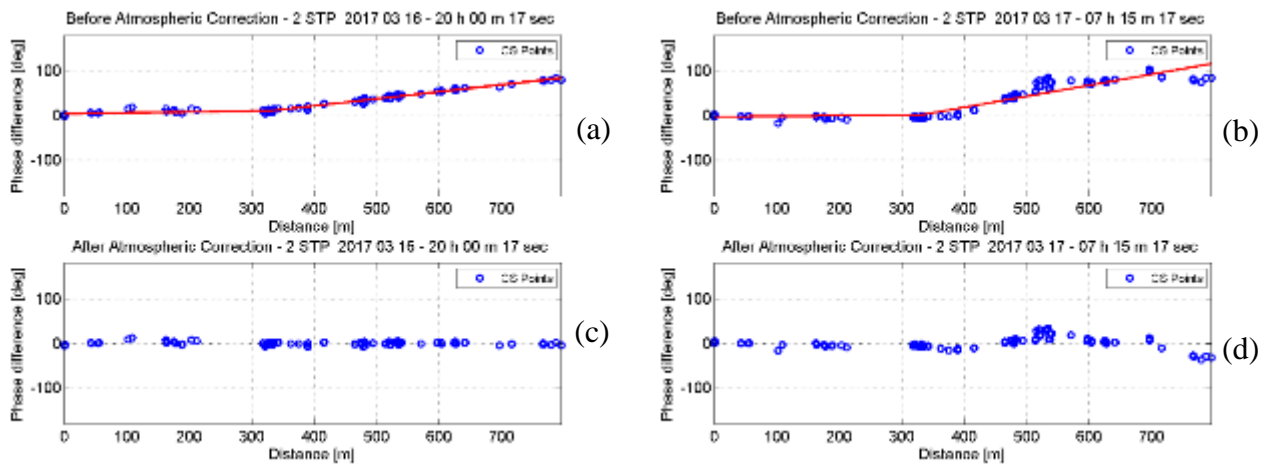

Figure 4.25 The coherence scatters (CS) phase change due to atmospheric artifact was represented. (a) Observed phase change at 20:00 along range direction with the proposed model (b) Observed phase change at 07:10 in next day morning, along range direction with the proposed model (c) and (d) shows the corresponding phase after applying the TSSA for atmospheric phase compensation.

85
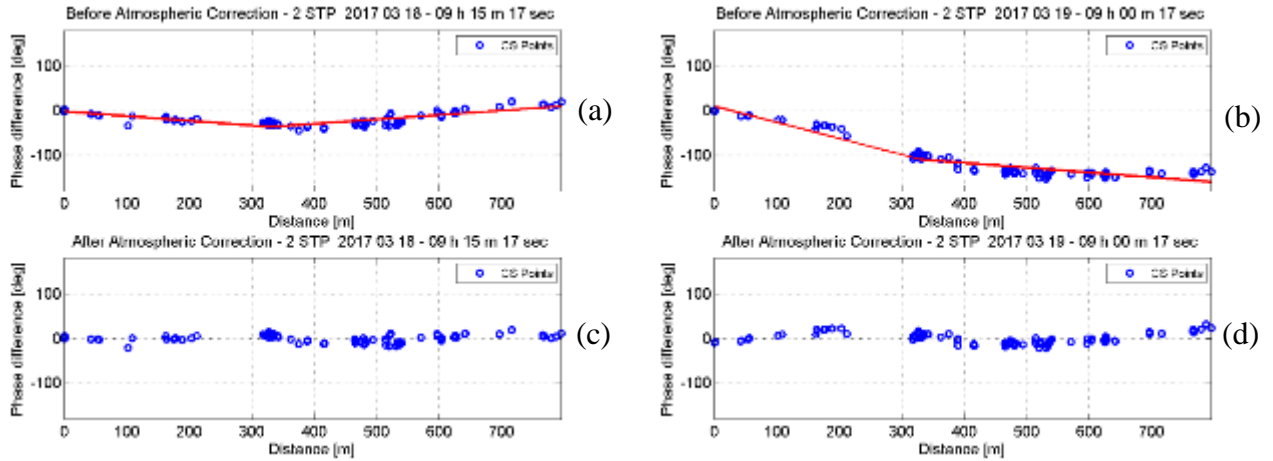
Figure 4.26 The coherence scatters (CS) phase change due to atmospheric artifact was represented. (a) Observed phase change at 09:15 along range direction with the proposed model (b) Observed phase change at 09:00 in the next day (after 24 hours) along range direction with the proposed model (c) and (d) shows the corresponding phase after applying the TSSA for atmospheric phase compensation.
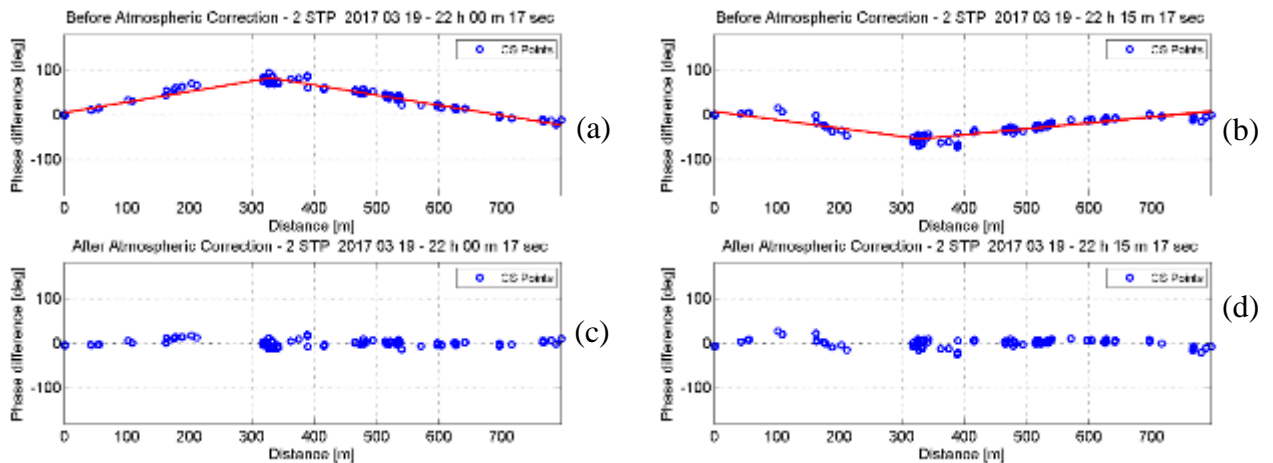
Figure 4.27 The coherence scatters (CS) phase change due to atmospheric artifact was represented. (a) Observed phase change at 22:00 along range direction with the proposed model (b) Observed phase change at 22:15 (after 15 minutes) along range direction with the proposed model (c) and (d) shows the corresponding phase after applying the TSSA for atmospheric phase compensation.

Figure 4.24 (a) and (b) to 4.27 (a) and (b) show the best fitted curve estimated by proposed method in different atmospheric conditions. The compensated phase was shown in corresponding (c) and (d) plots. Further, it demonstrates a good correlation in CS phase over time by minimizing the random fluctuation of the interferometric phase. Unlike conventional method, proposed method preserve the continuity of the phase, by giving similar output for different atmospheric conditions. This is a significant factor for displacement monitoring, in order to eliminate sudden phase jump over time.
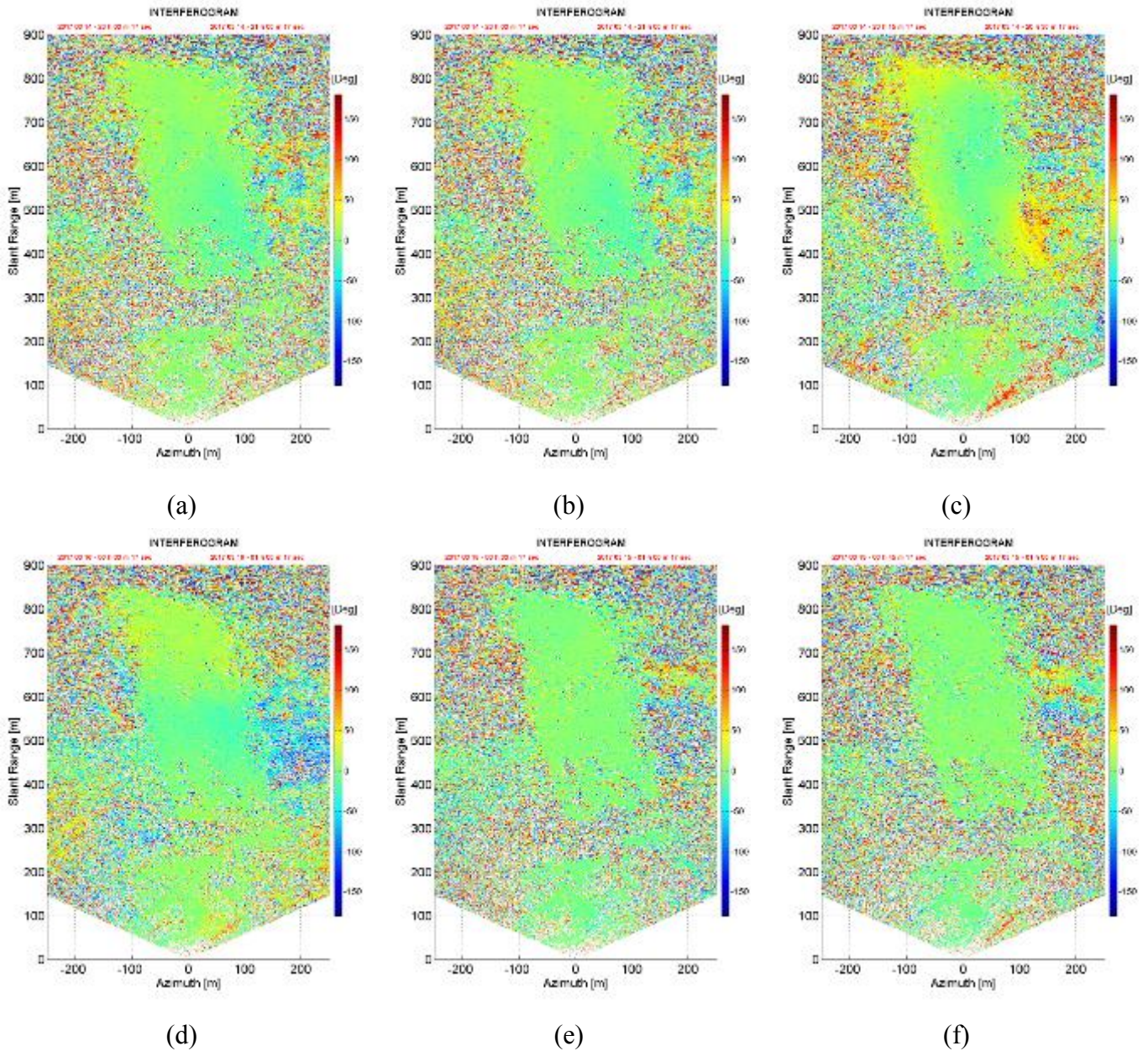
Figure 4.28 Estimated interferometric phase, after applying TSSA for atmospheric artifacts removel in 2D interferomgrams was represented. (a) Interferometric phase of 1 hour time interval. (b) 30 min. (c) 15 min. Differential phase due to inhomogeneity of the troposphere was compensated. Entire landslide area shows the constant vale (zero) for the phase change. After 3 hours in same day (d) Interferometric phase of 1 hour interval. (e) 30 minutes and (f) 15 minutes time intervals whow the similer resiults.

The TSSA was applied for the real time interferometric processing. The each data acquisition was corrected by estimated APS over the natural terrain. Figure 4.19 illustrates the 2D interferograms after applying TSSA. It clearly demonstrates the effectiveness of the proposed TSSA over the total area of illumination. Unlike before, each data set which belongs to different atmospheric conditions over time was equally compensated. The interferograms of one hour acquisition interval in Figure 4.7 (a) and (b) show the largest atmospheric disturbance which gives an erroneous estimation for conventional

87

atmospheric compensation method. Figure 4.7 (a) 1 hour, (c) in 30 minutes temporal based line and (d) 15 minutes baseline shows the multilayer phase ambiguity along range direction. It results under estimation of phase in near CS and overestimation of CS in far range. This was adversely affected for the one dimensional pinpoint measurements of observed displacements during the high atmospheric fluctuation.

The proposed TSSA shows the fastest and best fitting for entire interferogram in order to estimate differential phase free of deformation disturbances. Figure 4.19 (a) shows the APS removed interferogram in 1 hour data acquisition interval. The APS correction for 30 minutes and 15 minutes data acquisition has to illustrate the zero-mean valued for the differential phase. In the other hand, the phase compensation results of Figure 4.19 (d), (e) and (f) prove that the proposed TSSA can be effectively used to remove the APS in consecutive data acquisitions (sample data set after 3 hours) in order to preserve the coherency of interferograms. Also, it depicts that he zero phase change for 30 minutes and 15 minutes time interval both near range and far range for extreme weather conditions. This information was used to estimate the displacement over the monitoring area, in order to give landslide early warning to the people who work in the bottom of the mountain. The APS removed interferograms was used for the real-time early warning system. Since the model has higher sensitivity for the sudden atmospheric fluctuation, it accurately compensates the APS, so that the reliability of the displacement measurement was well defined.

4.3.2 Multiple approaches by piecewise linear regression model

The spatial dispersion of atmospheric phase screen and its temporal fluctuation over GB-SAR observation area shows random movement in above observed data sets. This phenomenon makes an erroneous estimation, especially for long range GB-SAR monitoring sites in a mountain area. When the observation area becomes larger, the observed range distance from GB-SAR become longer. The EM wave travels through the troposphere is larger and it adds considerable error in far filed distance than near field observation. Therefore accurate estimation of displacement for both near field and the far field leads to increase the reliability of both near field and far field in displacement measurement.

In this context, we have tested the reliability of the proposed two stage semi empirical atmospheric phase screen estimation method with distinct models such as three stage and multiple approaches. So we apply the linear regression with a step function and higher stage orders for random sample data sets. The applied regression method and estimated displacement over the total observation area were shown.

Two stage model Vs two step model

(a)   (b)
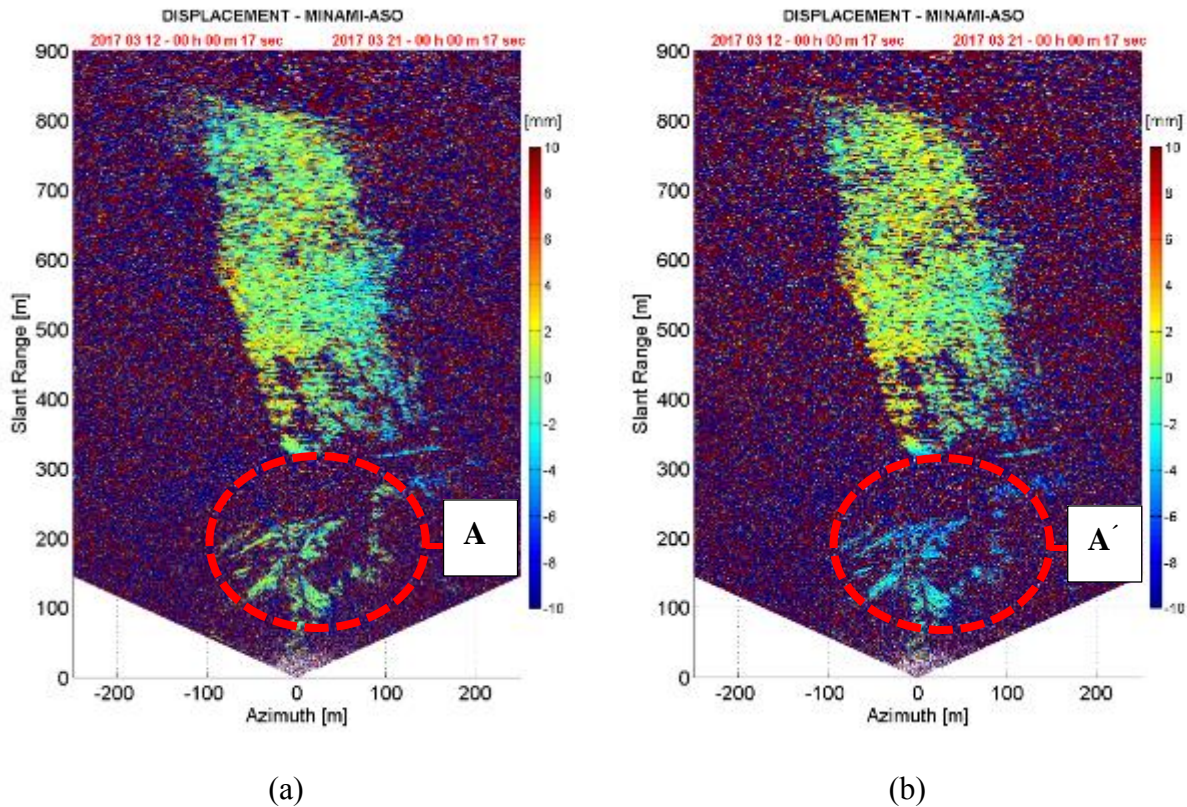
Figure 4.29   The estimated displacement by (a) Two-stage semi-empirical model - TSSA (b) Two-step model.

The TSSA preserve the continuity of the phase estimation in range direction (Figure 4.30 (a)), but two step model (right) completely separate (Figure 4.30 (b)) the near and the far range distance. This makes phase anomaly in the area marked in A and A´ 4.29 (a) shown the displacement around zero for both near and far distance, but Figure 4.29 (b) shows negative displacement, under estimation of phase.

(a)   (b)
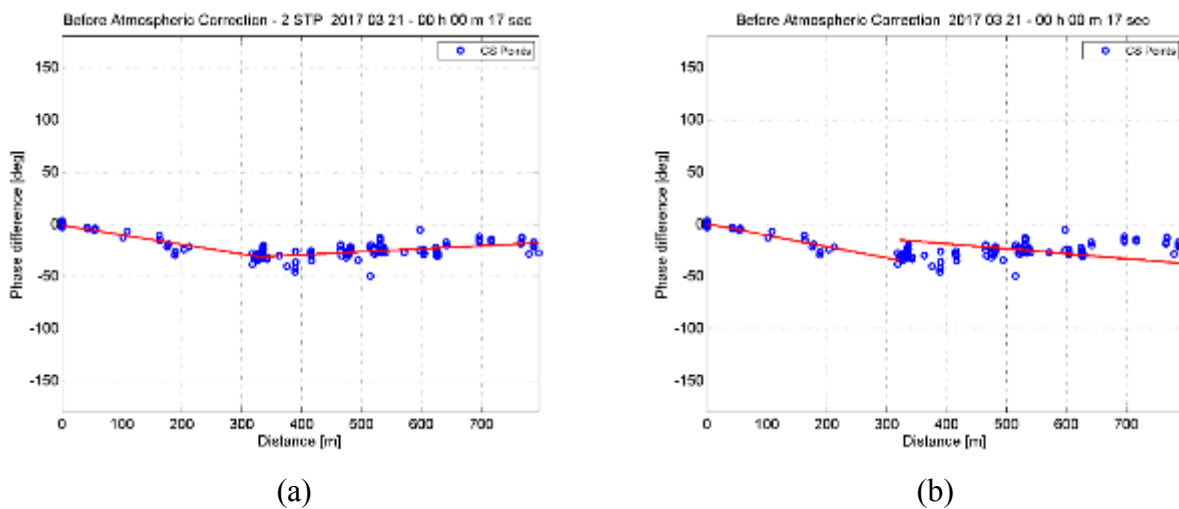
Figure 4.30 The CS phase estimation of (a) Two-stage semi-empirical model (b) Two-step model.

(a)   (b)
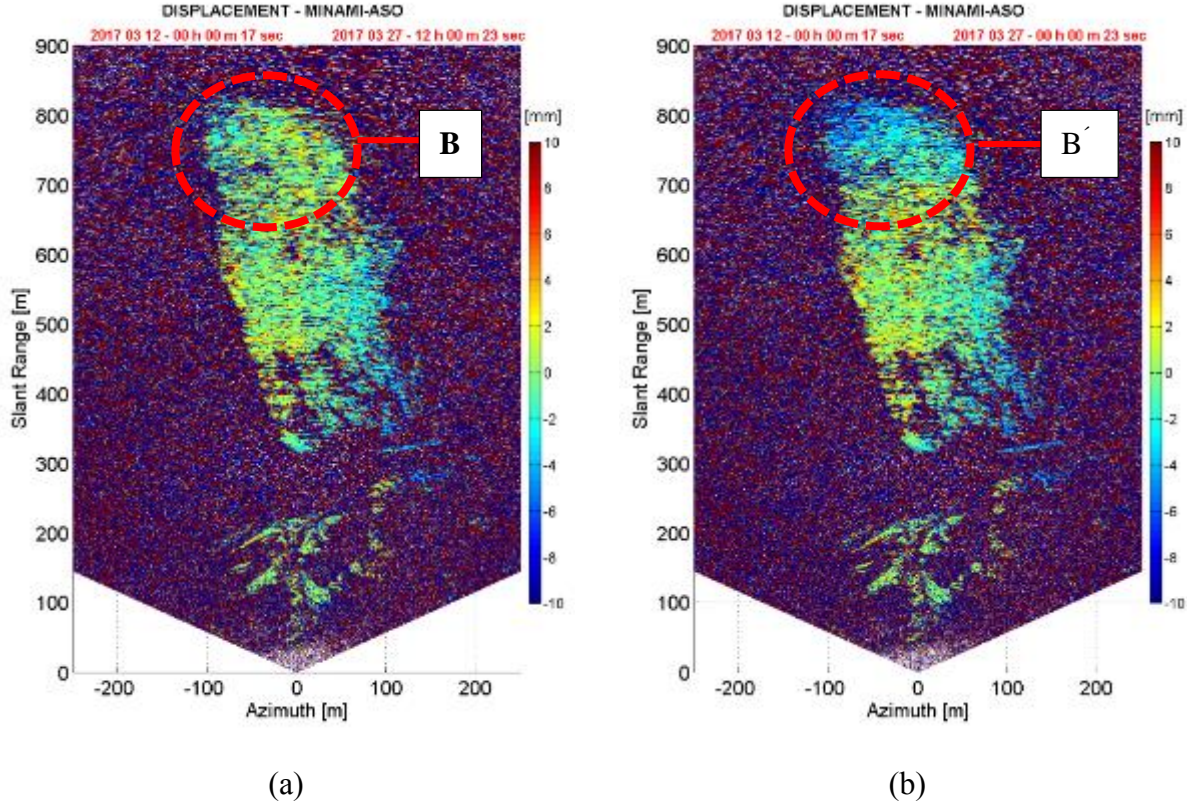
Figure 4.31 The estimated displacement by (a) Two-stage semi-empirical model (b) Three-stage semi-empirical model.

The results depict that the comparison of estimated displacement by TSSA and three stage model during 15 days period start from 12th to 27th March 2017.

$$\varphi_{corr} = \varphi_{Measure} - \varphi_{atm} \qquad (4.22)$$

The area B and the area B´ show the different estimation results for the displacement map. The color change of B´ emprise that this area was moved 10 mm towards the radar, but A does not show such considerable displacement in Figure 4.31 (a). Also, during this time period, the considerable movement was not recorded in pinpoint measurement equipment install in this area, such as extension meters. Therefore the 3 stage model shows an over estimation of phase screen in fare filed region in the 2D displacement map. Furthermore, it proved that B´ displacement was induced due to the inaccurate estimation of the atmospheric phase screen removal method. Therefore, this model could not be considered as an accurate model for atmospheric phase screen reduction.

4.4 References

[1] E. K. Smith Jr. and S. Weintraub, "The constant in the equation for atmospheric reflective index at Radio frequency," Proc. I. R. E, pp 1035-1037, October 1953.

[2] M. Pieraccini, N. Casagli, G. Luzi, D. Tarchi, D. Mecatti, L. Noferini and C. Atzeni (2003) Landslide monitoring by ground-based radar interferometry: A field test in Valdarno (Italy), *International Journal of Remote Sensing*, 24:6, 1385-1391, DOI: 10.1080/0143116021000044869

[3] G. Luzi, M. Pieraccini, D. Mecatti, L. Noferini, G. Guidi, F. Moia and Carlo Atzeni, "Ground-based radar interferometry for landslides monitoring: Atmospheric and instrumental decorrelation source on experimental data," *IEEE Trans. Geosci. Remote Sens.,* vol. 42, no. 11, pp 2454-2466, November 2004.

[4] L. Noferini, M. Pieraccini, D. Mecatti, G. Luzi, C. Atzeni, A. Tamburini and M. Broccolato, "Permanent scatterers analysis for atmospheric correction in ground-based SAR interferometry*," IEEE Trans. Geosci. Remote Sens.*, vol. 43, no. 7, pp 1459-1471, July 2005.

[5] L. Pipia, X. Fabregas, A. Aguasca and C. Lopez-Martinez, "Atmospheric Artifact Compensation in Ground-Based DInSAR Applications," in *IEEE Geoscience and Remote Sensing Letters*, vol. 5, no. 1, pp. 88-92, Jan. 2008.

[6] L. Iannini and A. Monti Guarnieri, "Atmospheric Phase Screen in Ground-Based Radar: Statistics and Compensation," in *IEEE Geoscience and Remote Sensing Letters*, vol. 8, no. 3, pp. 537-541, May 2011.

[7] K. Takahashi, M. Matsumoto and M. Sato, "Coherent scatterer selection based on coherence of interleaved sub-image for atmospheric correction of ground-based synthetic aperture radar interferometry," *in Proc. IEEE IGARSS*, 2013, pp. 3891-3894.

[8] R. Iglesias, X. Fabregas, A. Aguasca, J. J Mallorqui, C. Lopez-Martinez, J. A. Gili and J. Corominas, "Atmospheric phase screen compensation in ground-based SAR with a multiple-regression model over mountainous region," *IEEE Trans. Geosci. Remote Sens.*, vol. 52, no. 5, pp 2436-2449, May 2014.

[9] J. Fortuny-Guasch, "A Fast and Accurate Far-Field Pseudopolar Format Radar Imaging Algorithm," in *IEEE Transactions on Geoscience and Remote Sensing*, vol. 47, no. 4, pp. 1187-1196, April 2009.

[10] Online resource, Japan meteorological agencies, http://www.jma.go.jp/jma/indexe.html.

[11] G. D. Thayer, B. R. Bean and B. A. Hart, "Worldwide characteristics of refractive index and climatological effects," Environmental science services administration boulder, Colorado, 80302, United States, August, 1970.

[12] O. A. Alduchov and R. E. Eskridge, "Improved Magnus form approximation of saturation vapor pressure," *Journal of applied meteorology*, vol. 35, pp. 601-609, April 1996.

[13] R. F. Hanssen, Radar Interferometry: Data Interpretation and Error Analysis. Dordrecht, the Netherlands: Kluwer, 2001.

[14] G.D. Bye and R.G. Howell, "Average radio refractive index lapse rate of the lower troposphere for locations in NW Europe," British telecom research laboratory, UK, 1979.

[15] D.A. Tahmoush and A.E.E.Rogers, "Correcting atmospheric path variations in millimeter wavelength very long baseline interferometry using a scanning water vapor spectrometer," Radio science, vol. 35, no. 5, pp. 1241-1251, October 2000.

[16] Technical report, Evaporation, Atmospheric physics lab work, Institute for atmospheric and climatic science-IACETH, Swiss federal institute of technology, Zurich 2012.

[17] M. Matsumoto, "Fundamental studies on polarimetric and interferometric ground-based SAR for environmental monitoring," Doctor dissertation of Tohoku University, Japan, August 2013.

[18] Technical report, Attenuation by atmospheric gases, ITU Recommendation ITU-R P.676-3, online https://www.itu.int/dms_pubrec/itu-r/rec/p/R-REC-P.676-3-199708-S!!PDF-E

Chapter 5 Eigen vector and Eigen value based method for coherent scatter (CS) selection using radar polarimetry

In this chapter, Eigenvector and Eigenvalue based model was proposed to select the persistent scatters (PS) for fully polarimetric Ground Based Synthetic Aperture Radar (GB-SAR) system. The proposed model can be used to extract the PS pixels in a complicated urban environment such as construction site which highly correlated with random movements of man and unmanned vehicle and equipment with in short period of time.

5.1 Coherent scattering estimation

5.1.1   Coherent scatter

Prior to the estimation of land displacement phenomena, an adequate pixel selection must be carried out in order to prevent the inclusion of noisy pixels in the processing. The rationale is to detect the so-called persistent scatterer (PS), which are characterized by preserving their phase quality along the multi-temporal set of synthetic aperture radar (SAR) images available. Two criteria are mainly available for the estimation of pixels' phase quality, i.e., the coherence stability of the observed interferometric phase [1] [2] and the amplitude dispersion or permanent scatters (PS) approach [3].

In the coherence stability method, the PS were estimated by coherence from the multi-looked interferograms, which can be directly related to the standard deviation of the interferometric phase. The choice of the pixel selection criterion basically depends on the number acquired datasets, on the resolution required and on the nature of the scenario to be monitored. On the one hand, the coherence stability method ensures accurate estimations of the phase statistics, even when a reduced number of SAR images is available. In contrast, the PS approach demands a larger number of SAR images to be reliable, typically more than 30 [3]. On the other hand, the coherence stability criterion performs better over environments with the predominance of distributed targets.

5.1.2   Conventional method

In this method, CS estimation criteria based on the dispersion of the amplitude along consecutive SAR images. The reflected signal from deterministic targets presenting high values of signal-to-noise ratio (SNR) with the amplitude dispersion (DA) estimator, which basically corresponds to a measure of the pixels' amplitude stability. This can be estimated as variation of amplitude through a number of images taken at different lapse time and obtained as,

$$D_{m,n} = \sigma_{m,n} / A_{m,n} \qquad (5.1)$$

where is the $\sigma_{m,n}$ standard deviation and $A_{m,n}$ is mean of amplitude with respect to the lapse time at pixel (m, n) respectively. In this method, the pixels stable by amplitude is assumed to be reliable in phase. The phase dispersion was estimated from the amplitude dispersion. But this assumption only be reliable for when the SNR of SAR image was lower, indeed estimated dispersion of amplitude was lower (typically DA <0.25) [3].

The concept of distributed target arises from the fact that not all radar targets are stationary or fixed, but generally, they are located in a dynamically changing environment and are subject to spatial and temporal variations. However, even if the environment is dynamically changing, one has to make an assumption concerning stationarity, homogeneity, and ergodicity. This can be analyzed more precisely by introducing the concept of space and time varying stochastic processes, where the target or the environment can be described by the second order moment of the fluctuations which will be extracted from the polarimetric covariance matrices [4].

5.2 Eigenvector and Eigenvalue based method for CS estimation

5.2.1 Polarimetric statistics

The backscattered signal from fully polarimetric GB-SAR contain S_{HH}, S_{VV} co-channel reflection and S_{HV}, S_{HV} cross-channel reflection. The characterization of a given scatterer by means of the target surface and its orientation, the backscatter signal has more detail information which is very important to monitor the spatiotemporal changes of the target. The eigenvector and eigenvalue analysis of the coherency T3 matrix employs a three-level Bernoulli statistical model to generate an estimate of the average target scattering matrix parameters. This alternative statistical model sets out with the assumption that there is always a dominant scattering mechanism in each cell and then undertakes the task of finding the parameters of those average component. The backscattered signal from fully polarimetric GB-SAR contain, co-channel reflection and, cross-channel reflection,

$$T = \begin{bmatrix} \langle |S_{HH} + S_{VV}|^2 \rangle & \langle (S_{HH} + S_{VV})(S_{HH} - S_{VV})^* \rangle & 2\langle (S_{HH} + S_{VV})S_{HV}^* \rangle \\ \langle (S_{HH} - S_{VV})(S_{HH} + S_{VV})^* \rangle & \langle |S_{HH} - S_{VV}|^2 \rangle & 2\langle (S_{HH} - S_{VV})S_{HV}^* \rangle \\ 2\langle (S_{HH} + S_{VV})^* S_{HV} \rangle & 2\langle (S_{HH} - S_{VV})^* S_{HV} \rangle & 4\langle |S_{HV}|^2 \rangle \end{bmatrix} \qquad (5.2)$$

(a)   (b)

(c)   (d)
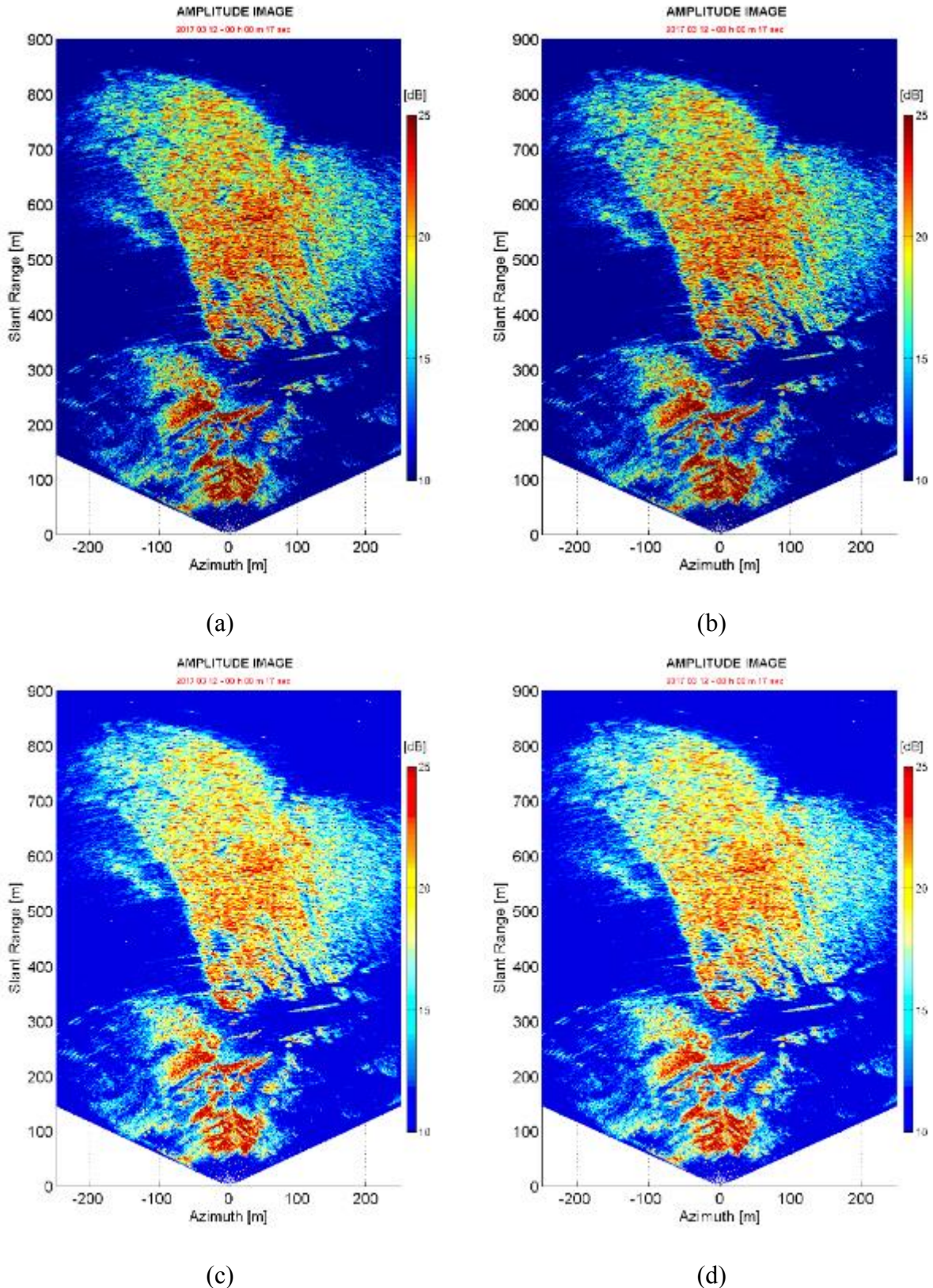
Figure 5.1 The backscattering power from co- polarimetric channels (a) HH (b) VV and cross-polarimetric channel (c) HV (d) VH was interpreted. The both channel shows higher power reflection in near object and it was decrease with increasing range. The co-polarimetric channels shows relatively high scattering power than cross-polarimetric channel. The open soil layer of the landslide area and the tree canopy can be clearly separated.

5.2.2 Matrix formulation for Eigen based model

The eigenvector and eigenvalue of the 3 x 3 Hermitian averaged coherency T3 matrix can be calculated to generate a diagonal form of the coherency matrix which can be physically interpreted as a statistical independence a set of target vectors. The coherency T3 matrix and its eigenvalue and eigenvector satisfy the following equation,

$$T_3 \underline{u}_i = \lambda_i \underline{u}_i \qquad (5.3)$$

where $i = 1, 2, 3$ and   is a 3 x 3 diagonal matrix with nonnegative real elements and the unitary matrix

$$T_3 [\underline{u}_1 \quad \underline{u}_2 \quad \underline{u}_3] = [\underline{u}_1 \quad \underline{u}_2 \quad \underline{u}_3] \begin{bmatrix} \lambda_1 & 0 & 0 \\ 0 & \lambda_2 & 0 \\ 0 & 0 & \lambda_3 \end{bmatrix} \qquad (5.4)$$

$$U_3 = [\underline{u}_1 \quad \underline{u}_2 \quad \underline{u}_3] \qquad (5.5)$$

The equation 5.4 can be written in matrix notation with a diagonal matrix

$$T_3 U = U \Lambda \qquad (5.6)$$

$$T_3 = U \Lambda U^{*T} \qquad (5.7)$$

$$T_3 = \begin{bmatrix} \underline{u}_1 & \underline{u}_2 & \underline{u}_3 \end{bmatrix} \begin{bmatrix} \lambda_1 & 0 & 0 \\ 0 & \lambda_2 & 0 \\ 0 & 0 & \lambda_3 \end{bmatrix} \begin{bmatrix} \underline{u}_1^{*T} \\ \underline{u}_2^{*T} \\ \underline{u}_3^{*T} \end{bmatrix} \qquad (5.8)$$

$$T_3 = \begin{bmatrix} \underline{u}_1 & \underline{u}_2 & \underline{u}_3 \end{bmatrix} \begin{bmatrix} \lambda_1 \underline{u}_1^{*T} \\ \lambda_2 \underline{u}_2^{*T} \\ \lambda_3 \underline{u}_3^{*T} \end{bmatrix} \qquad (5.9)$$

$$T_3 = \lambda_1 \underline{u}_1 \underline{u}_1^{*T} + \lambda_2 \underline{u}_2 \underline{u}_2^{*T} + \lambda_3 \underline{u}_3 \underline{u}_3^{*T} \qquad (5.10)$$

$$T_3 = \sum_{i=1}^{i=3} \lambda_i \underline{u}_i \underline{u}_i^{T*} \qquad (5.11)$$

where T^* represents the complex conjugate of the matrix T.

The matrix is of rank one. The Hermitian matrix is decomposed into the sum of three independent scattering targets, each of which is represented by a single scattering matrix as indicated as above.

5.2.3 Polarimetric entropy H for GB-SAR

The polarimetric entropy represents the statistical disorder of each distinct scattering type. It indicates the depolarization of the backscattered signal. According to Von Neumann [6] entropy concept can write as,

$$H = -\sum_{k=1}^{N} P_k \log_N (P_k) \tag{5.12}$$

Where Pi corresponds to the pseudo-probabilities obtained from the eigenvalues by,

$$P_i = \frac{\lambda_i}{\sum_{k=1}^{3} \lambda_k} with \sum_{k=1}^{3} P_k = 1 \tag{5.13}$$

The eigenvalue is the logarithm basis and it is important to note that this basis is not arbiter but must be equal to the polarimetric dimension (N=3 for GB-SAR). Since the eigenvalues are rotation invariant, the polarimetric entropy H is also a roll-invariant parameter.
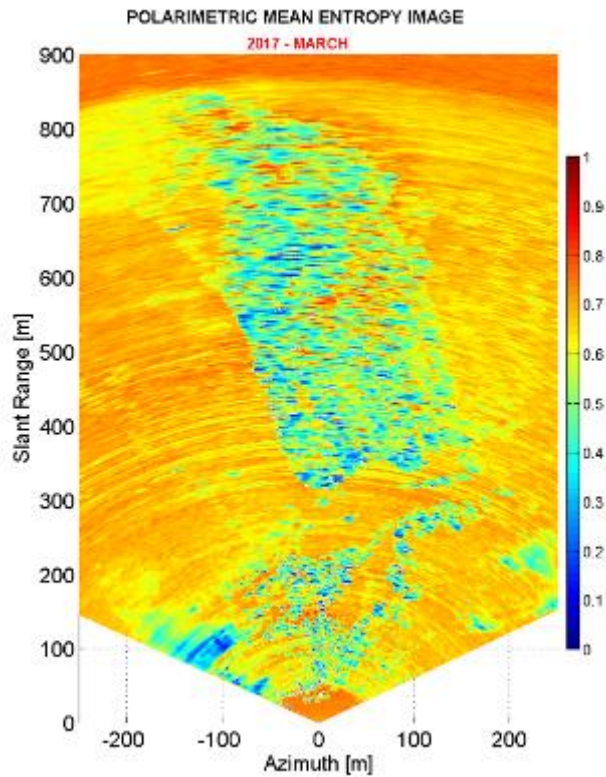
Figure 5.2 The Estimated polarimentic entropy

5.2.4 Polarimetric Alpha for GB-SAR

The polarimetric Alpha angle is directly related to the average physical scattering mechanism. Hence, it can be used to associate observables with physical properties of the medium. The mean polarimetric scattering angle alpha is derived from normalized eigenvector of equation 5.11, and is calculate as,

$$\alpha_i = \sum_{i=1}^{n} P_i \cdot a\cos\left(\left|e_{i1}\right|\right) \tag{5.14}$$

where e_i correspond to the eigenvector of,

$$e_i = \begin{bmatrix} e_{i1} & e_{i2} & e_{i3} \end{bmatrix}^T \tag{5.15}$$
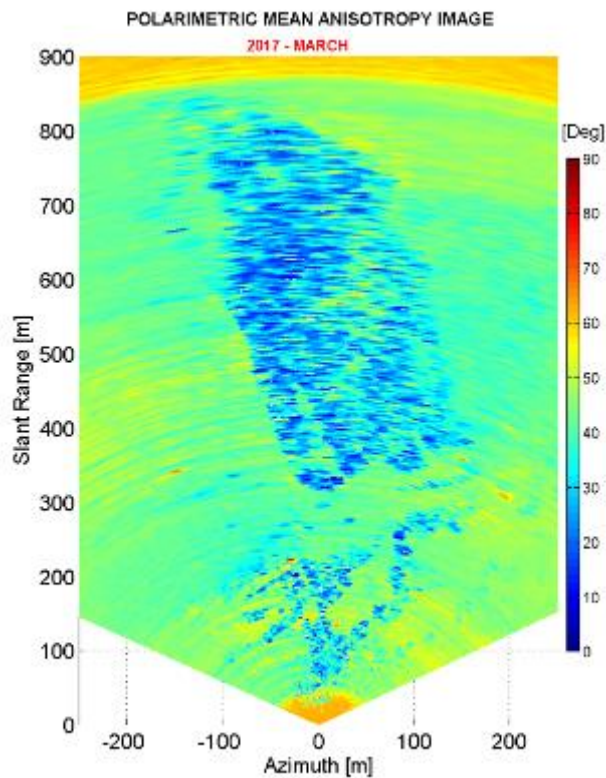
Figure 5.3 The Estimated polarimetric alpha angle

5.2.5 Proposed criteria for CS estimation

The entropy arises as a natural measure of the inherent reversibility of the scattering data and that the alpha angle can be used to identify the underlying average scattering mechanisms. The H/Alpha plane can be subdivided into nine basic zones as shown in Figure 5.4 by considering different scattering behavior, in order to separate the data into basic scattering mechanism. The each of this zones independently represent the pixel indexes which correspond to dominant scattering mechanisms identified by backscattered signal.
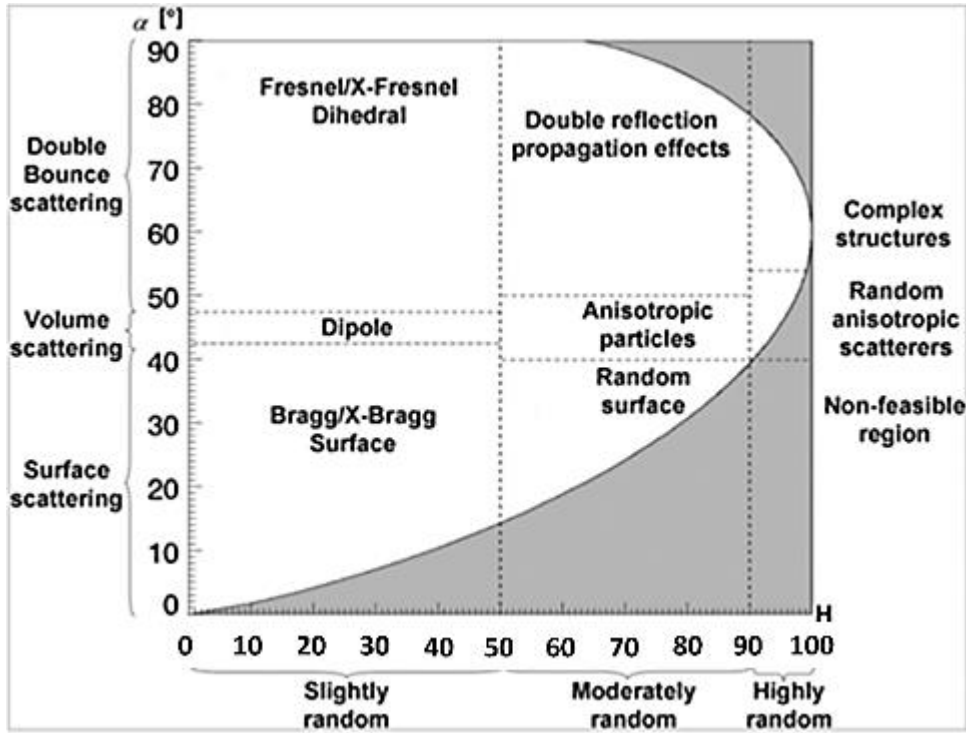
Figure 5.4 The entropy alpha plane was depected. The total plane was devided in to nine classes [2]

In lower entropy region, scatters are more stable. They show slightly random movement for incident EM wave, which is most stable among the total observation area. On the other hand, thesis scatter interfaces show most simple surface scattering for poalrimetric alpha angle. Therefor combing these two criteria, results most stable and deterministic scatter location in 2D plane in the observation area. This criteria can further used to find the most stable CS locations,

$$\sum_{i=1}^{m}\sum_{i=1}^{n} CS_{index} = a. \left| -\sum_{k=1}^{N} P_k log_N(P_k) \right| \cap b. \left| \sum_{i=1}^{n} P_i. acos(|e_{i1}|)P_k) \right| \qquad (5.16)$$

5.3 CS estimation and validation Minami-Aso

5.3.1 CS estimation for fully polarimetric GB-SAR
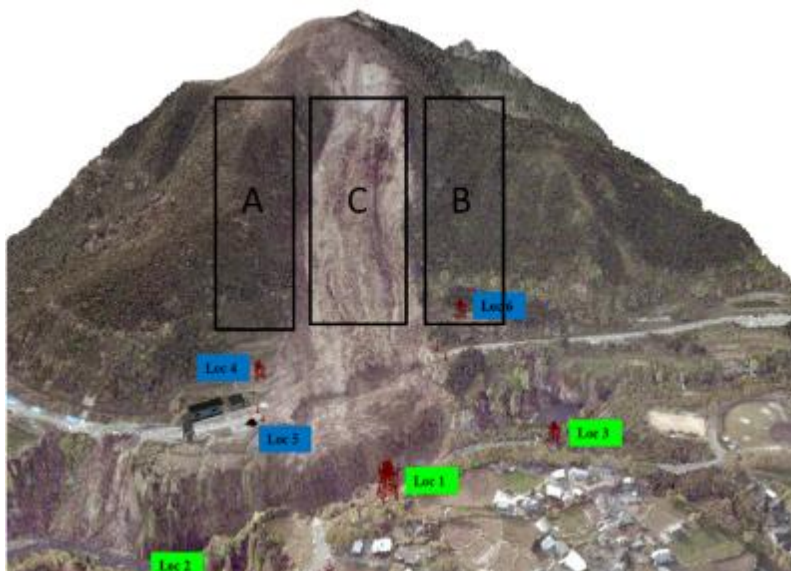
Figure 5.5 The reflected fully polarimetric was classified in to Class A, B and C spatial model
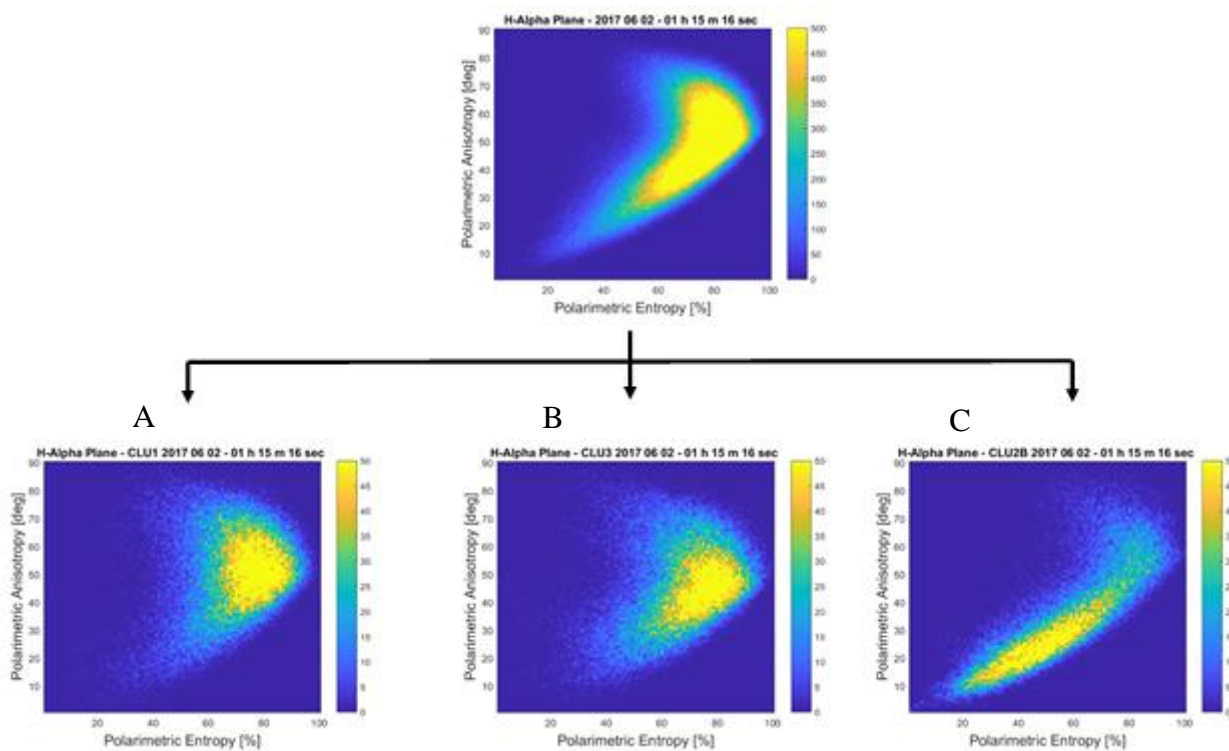
Figure 5.6 Observed total backscatter was separated into spatial model A, B and C

5.3.2 Reflection from corner reflectors
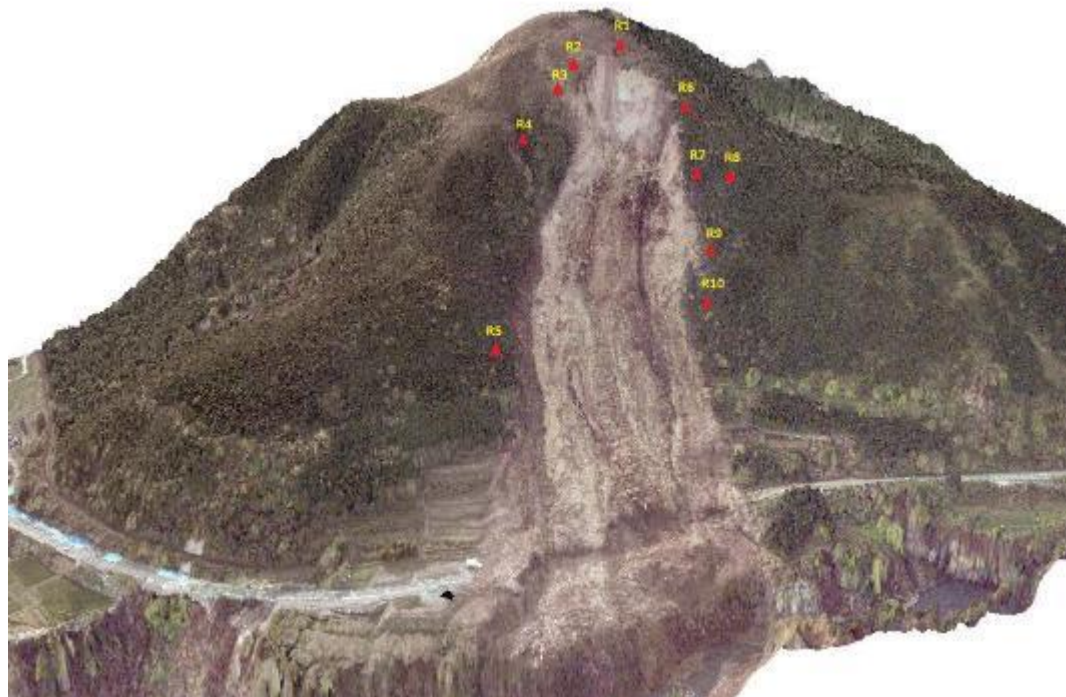
Figure 5.7 The location of the cornner reflectors

The proposed method was applied to real data set acquired by fully polarimetric GB-SAR which was deployed for the landslide early warning system Minami-Aso. The location of the corner reflectors was shown in Figure 5.7.

Figure 5.8 Images shown the installed places and orientation of
the cornner reflectors

5.3.3 Validation
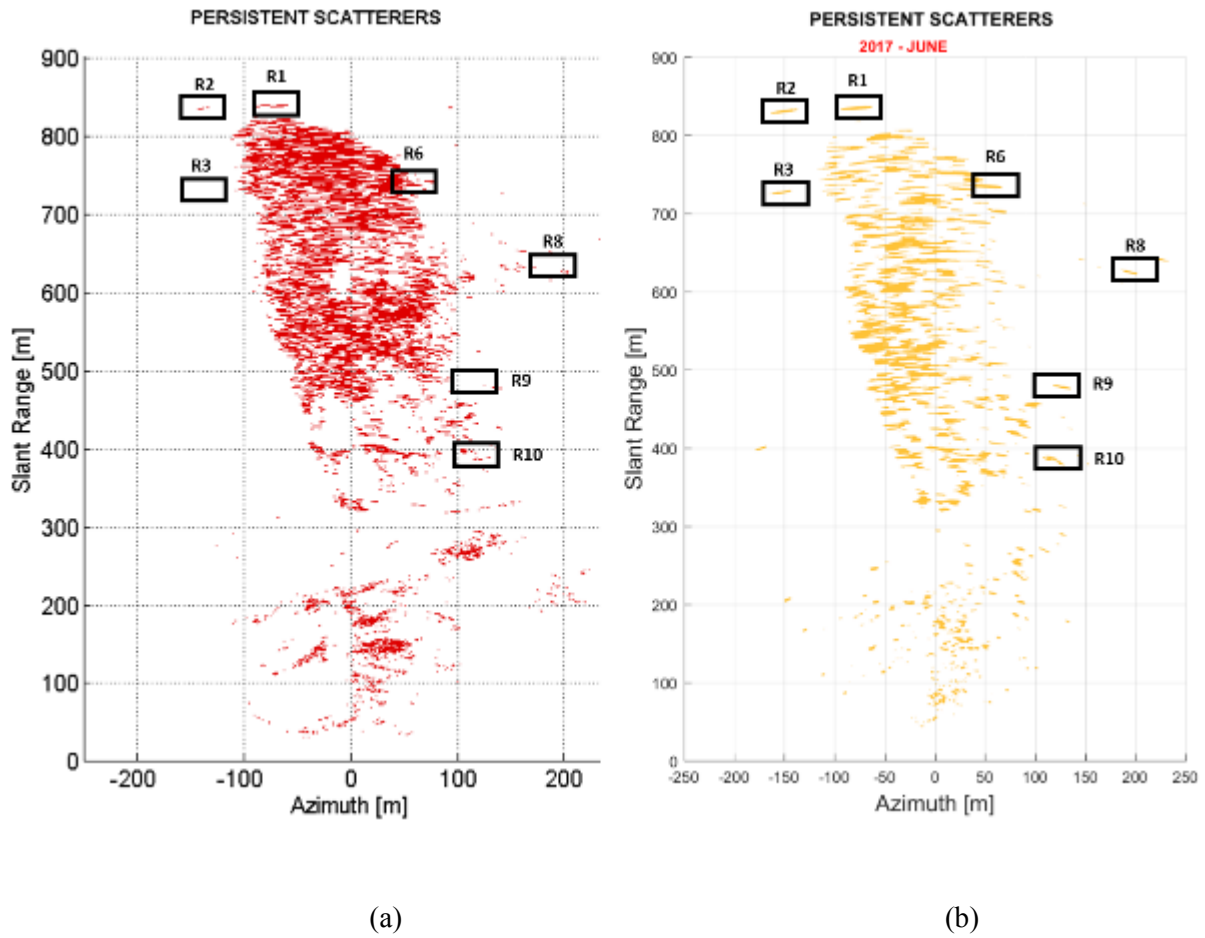
Figure 5.9 The estimated CS location by (a) conventional amplitude dispersion method (b) Proposed eigenbased method

The results show that the proposed method can be used to identify the CS location by a limited number of SAR scanning. Further, it gives a reliable estimation for far range objects, the Corner reflector R2, R3, which could not be clearly visible by conventional CS estimation method. Since the amplitude of the power image decrees with range direction, most of the power reflected over 1000m is happen to change eventually irrespective for their stability. This was adversely affected by conventional DA index method by addressing the estimated stability of far field objects.

5.4 References

[1] Lanari, R.; Mora, O.; Manunta, M.; Mallorqui, J.J.; Berardino, P.; Sansosti, E. A small-baseline approach for investigating deformations on full-resolution differential SAR interferograms. IEEE Trans. Geosci. Remote Sens. 2004, 42, 1377–1386.

[2] J.S. Lee and E. Pottier, Polarimetric radar imaging from basic to application, CRC Press, 2009.

[3] Ferretti, A.; Prati, C.; Rocca, F. Permanent Scatterers in SAR interferometry. IEEE Trans. Geosci. Remote Sens. 2001, 39, 8–20.

[4] J.S. Lee and E. Pottier, Polarimetric radar imaging from basic to application, CRC Press, 2009.

[5] J. Praks, E.C. koeniguer and M.T. Hallikainen, "Alternatives to target entropy and alpha angle in SAR polarimetry," IEEE Trans. Geosci. Remote Sens. 2009,47, 2262-2274.

[6] J. Von Neumann, Mathematische Grundlage der Quantenmechanik (Mathematical foundation of quantum mechanics). Berlin, Germany: Springer-Verlag, 1995

Chapter 6 GB-SAR Installation and configuration for continuous monitoring, Minami-Aso, Kumamoto, Japan

During the post-disaster period, sudden recovery projects were launch for Minami-Aso road reconstruction. Due to the instability of the top soil layer on the hillside of the main landslide area and number of the recorded earthquake in a fault zone, stability information of the open soil layer become significantly important for the workers who involve with daily road construction work. In this background, GB-SAR remote sensing technique notified as the best solution for retrieving the stability information of the total landslide area in order to give the landslide early warning for the workers for disaster prevention. This chapter describes the complete procedure of GB-SAR system installation. Furthermore, an establishment of landslide monitoring system and landslide early warning system will briefly discuss.

6.1 GB-SAR installation

Figure 6.1 GB-SAR system deploy in Minami-Aso

The GB-SAR system was installed (Figure 6.1) and data acquisition was started from mid of January 2017. The linear rail was mounted in 1.5 m rigid concrete blocks, in order to achieve estimated height for a stable platform.

Figure 6.2 GB-SAR system configuration

The system was aligned to 315° LOS with 23° views (tilt) angle. The system calibration was done and sudden atmospheric change is shown high influence for the interferometric phase which needs to be compensated in order to estimate the ground displacement accurately.

Differential SAR interferometry works under the coherent condition where the received waveforms correlate in the compared SAR pair. The One of the benefits of the GB-SAR sensor is the opportunity to gather zero-baseline repeated scans for differential measurements. Therefore terms usually affecting the differential coherence such as image co-registration approximation, baseline construction uncertainties, and digital elevation model removal residual errors become negligible [1].

However, the GB-SAR works on Ku band has high sensitivity for the small scale changes, which tends to decorrelate within the time frame and complicates the quantitative long term analysis. The problem of phase wrapping is one of the main issue observed in long range SAR interferograms. Typically, phase unwrapping is performed on data regularly sampled and stored in two-dimensional matrices [2]. Unwrapping the phase without ambiguity requires that the absolute phase gradient of the true phase between adjacent samples which less than π phase change along unwrapping path. Here we use multi-interferogram frame work to identify highly coherent targets along radar LOS, to overcome the most of the difficulties related to phase unwrapping and to discern the different signal that concur to the interferometric phase.
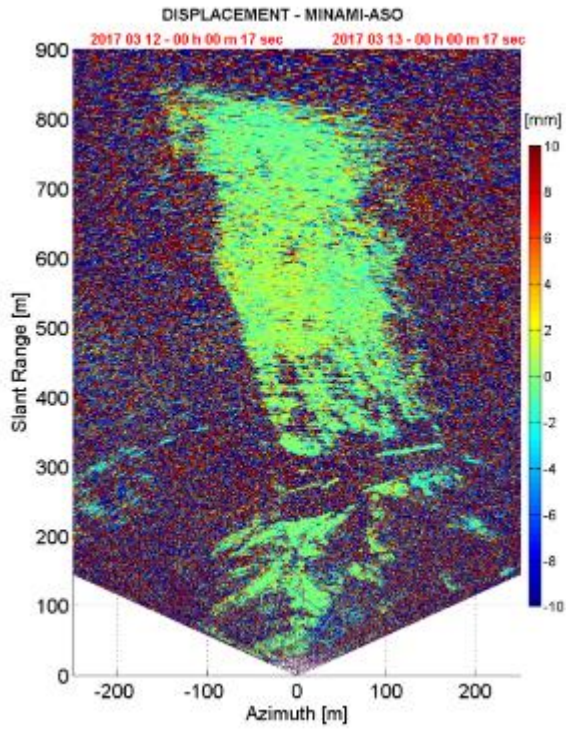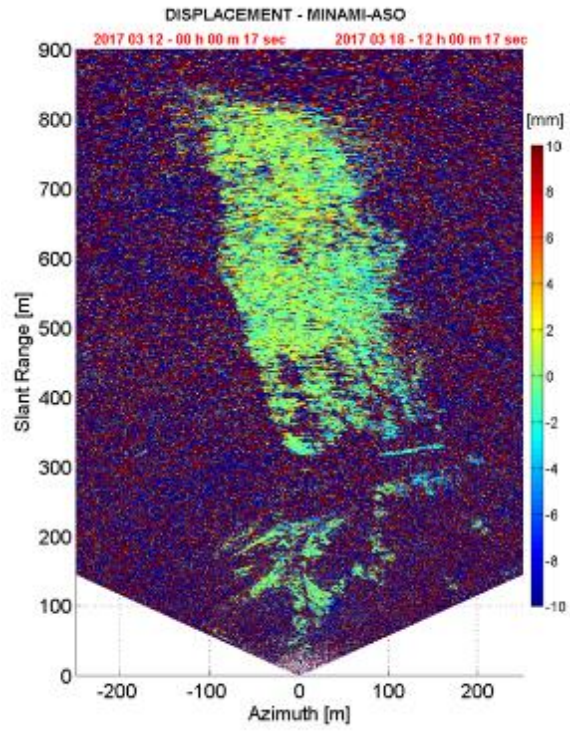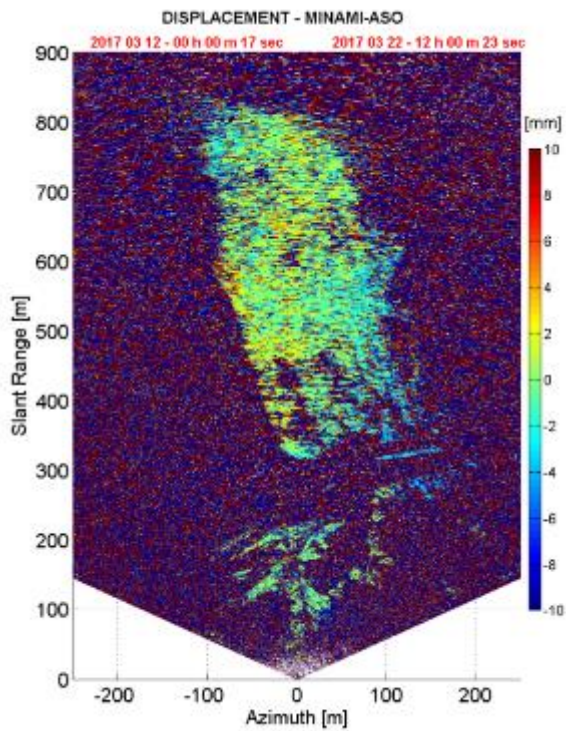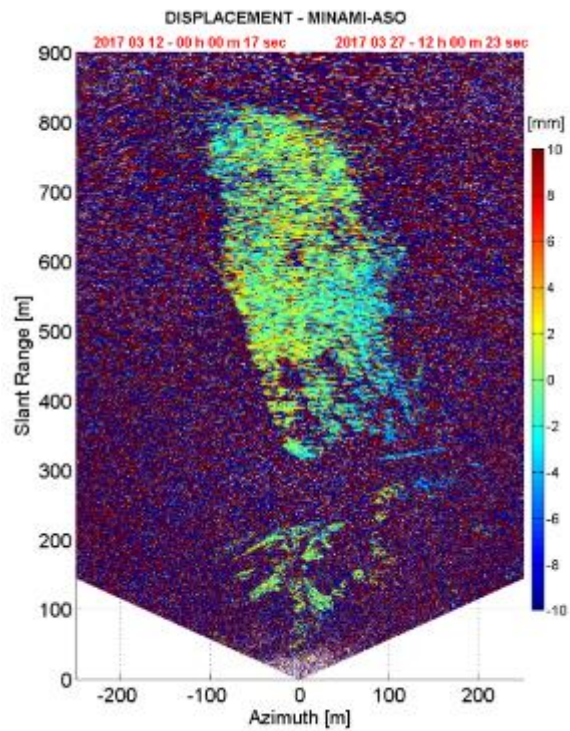
Figure 6.3 Interferograms of cumulative phase of (a) 1 day observation (b) 5 day observation (c) 10 day observation and (a) 15 day observation

6.2 Setting up the data acquisition interval

6.2.1 Interferometric phase quality estimation

The complex coherency of interferograms describe the correlation between consecutive data acquisitions and is a vital measurement of where the phase is exploitable. It should be emphasized that coherence serves as quality measurement both of the acquisitions. The complex coherence between two images is defined as [3],

$$\gamma_c = \frac{E\{M \cdot S^*\}}{\sqrt{E\{M \cdot M^*\} \cdot E\{S \cdot S^*\}}}$$
(6.1)

where $E\{.\}$ is the statistical expectation. The coherence is defined by $\hat{\gamma}$, and it estimates as [4],

$$\hat{\gamma} = \frac{\frac{1}{n}\sum_{i=1}^{n} M_i \cdot S_i^*}{\sqrt{\frac{1}{n}\sum_{i=0}^{n} M_i M_i^* \frac{1}{n}\sum_{i=0}^{n} S_i S_i^*}}$$
(6.2)

The coherence resides in the range [0, 1] with high values being coherent. The coherence decorrelates with time due to changes in the observed scene. The material and shape of the scene highly affect the coherence. The vegetation has low coherence due to its entropic nature while solid material such as rock and structure maintain high coherence for a longer period of time.

In this campaign, the observation area was ranged up to 800 m, contains the open soil layer which exposed after the landslide and the dense tree canopy spared besides the main observation area. The data acquisition interval of the remotely operate GB-SAR sensor notified as a considerable factor for,

  ➢ Temporal phase compensation,
  ➢ Decide data transfer rate,

For displacement estimation in real time operation. In advanced, this can be used to preserve coherency of the interferometric phase in order to minimize the temporal decorrelation. In the other hand, the problem of phase wrapping due to the wave propagation in range direction can be technically minimized by selecting the optimum data acquisition interval. It will improve the quality of the interferograms and render the reliable information for displacement monitoring.

6.2.2 Experimental results

(a)

(b)

(c)

(d)

(e)

(f)
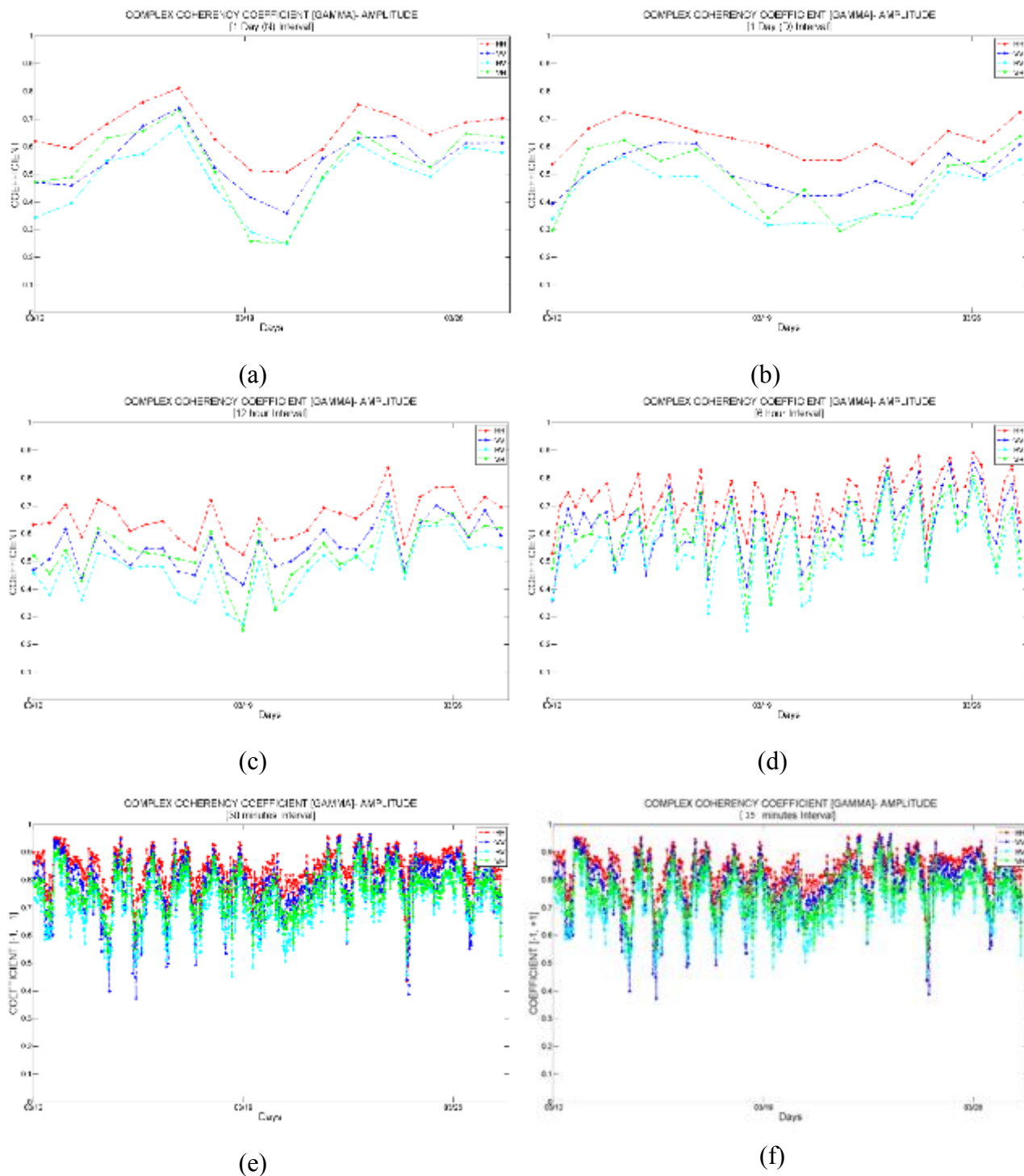
Figure 6.4 Estimated complex coherence for (a) 1 day data acqucitiion interval (Night time) (b) 1 day data acqucitiion interval (Day time) day observation (c) 12 hour data acqucitiion interval (d) 6 hour data acqucitiion interval (e) 30 minutes data acqucitiion interval (f) 15 minutes data acqucitiion interval

The location near to the GB-SAR monitoring station become a notable factor for the water vapour content of the atmosphere in low elevation area. The wind speed and the wind direction has high influence for the sudden change of the humidity measurement. This can be identified as a desirable factor, which affects for reflectivity due to highly dynamic weather conditions [5][6].

Due to the compatibility of the latest GB-SAR system, the data acquisition interval can speed up to 40 seconds. During the preliminary site observation, the fast data acquisition was not a necessity for real time manner, than appropriate. Therefore, the data acquisition interval was testified for 24 hours (both day time and night time) up to 1 minute of interval and complex coherency was estimated as a qualitative and the quantitative parameter for interferometric phase. The table 3 shows the estimated complex coherence coefficient for each data acquisition intervals in sample data set acquired from 12th March to 27th March. This statistical estimation depicts that the $\hat{\gamma}_{mean}$ has high fluctuation for long data acquisition interval. Apart from the number of data sets, the estimated $\hat{\gamma}_{mean}$ for day time has higher

Table 3. Estimated complex coherency coefficients

Date	Number of data sets	$\hat{\gamma}_{mean}$
1 Day (Night time)	16	0.6635
1 Day (Day time)	16	0.6021
12 hours	32	0.6540
6 hours	63	0.7209
3 hours	127	0.7663
1 hour	312	0.8102
30 minutes	616	0.8390
15 minutes	1231	0.8555
10 minutes	2251	0.8607
5 minutes	4501	0.8735
1 minute	9000	0.8980

value than estimated $\hat{\gamma}_{mean}$ during the night time. This emphasizes that the observed interferometric phase during the day time is inconsistent than night time in sample data set. Furthermore, the estimated interferometric phase distortion due to environmental change become more significant in day time than night time.

6.2.3 Optimum data acquisition interval
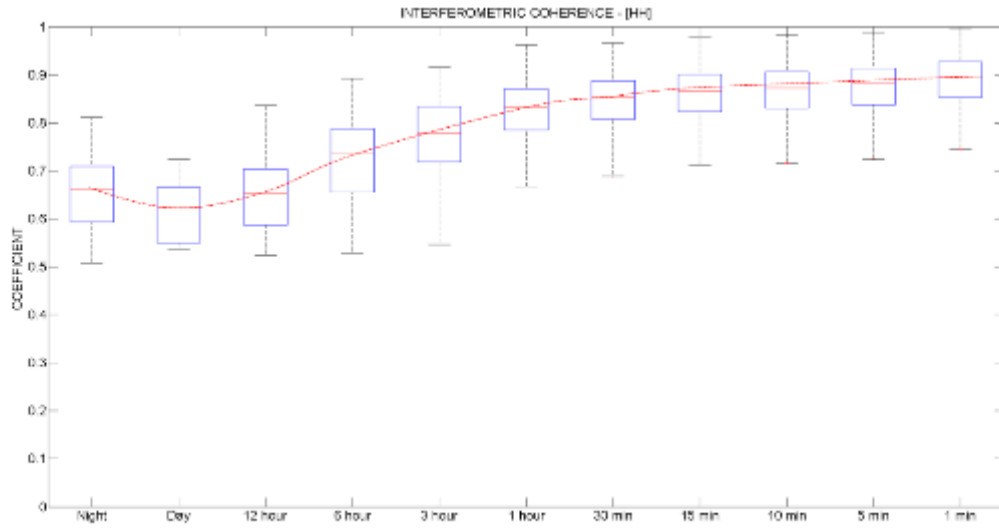
Figure 6.5 The interferometric phase quality estimation. The interferometric coherence coefficient change by temporal bassline 24 hours to 1 minutes of interval was summarized in the box plots.

The estimated $\hat{\gamma}_{mean}$ variation for data acquisition interval of 1 Day interval, 12 hours, 6 hours and up to 1 minutes was summarised in Figure 6.5. The higher coherency value (close to 1) was noticed for small data acquisition interval and the coherency become weaker (close 0.6) in larger data acquisition intervals. It depicts that the temporal decorrelation was significantly changed in 24 hours to 30 minutes time interval. The temporal decorrelation of interferometric phase shown high fluctuation in this region which advisedly effect for the reliability of the phase estimation. The estimated $\hat{\gamma}_{mean}$ in 15 minutes to 1 minute data acquisition interval has high coherency and it remained stable for 15 min, 10 min, 5 min and 1 min data acquisition interval. Thereby the 15 minutes data acquisition interval was fixed as an optimum data acquisition interval.

6.3 Development of displacement monitoring system
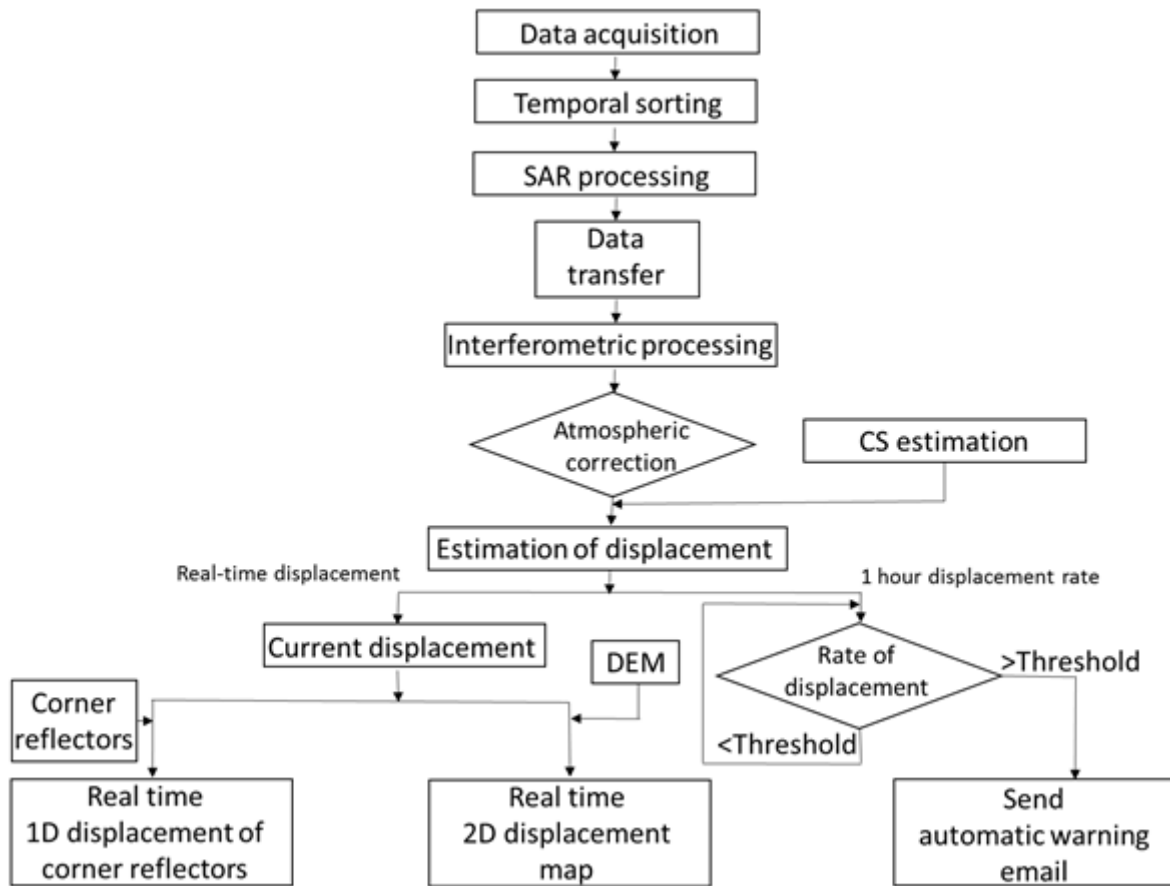
Figure 6.6 Data processing diagrame of real time landslide monitoring system

The flow chart shows the complete data processing steps and prototype of the develop landslide monitoring and early warning system. The preprocessing of the acquired data was done on the PC kept in the monitoring site and the after preliminary processing completed, it was transferred through to the Tohoku University through internet. This process was done automatically. In this experimental set-up, we have investigated several data transferring mechanisms. Finally, we used most cost efficient and secure Google sever system for data upload. We used fix Wi-Fi router with appropriate internet connection for data transferring. The operating PC was permanently connected to the internet and synchronized with the google server. So that the newly acquired data was automatically updated in the cloud data base. The same cloud server was shared by both Minami-Aso PC and the monitoring PC dedicated in Tohoku University for real time observation. It will minimize the data download time and make the complete data transfer process automated.

6.3.1 Automatic mapping system
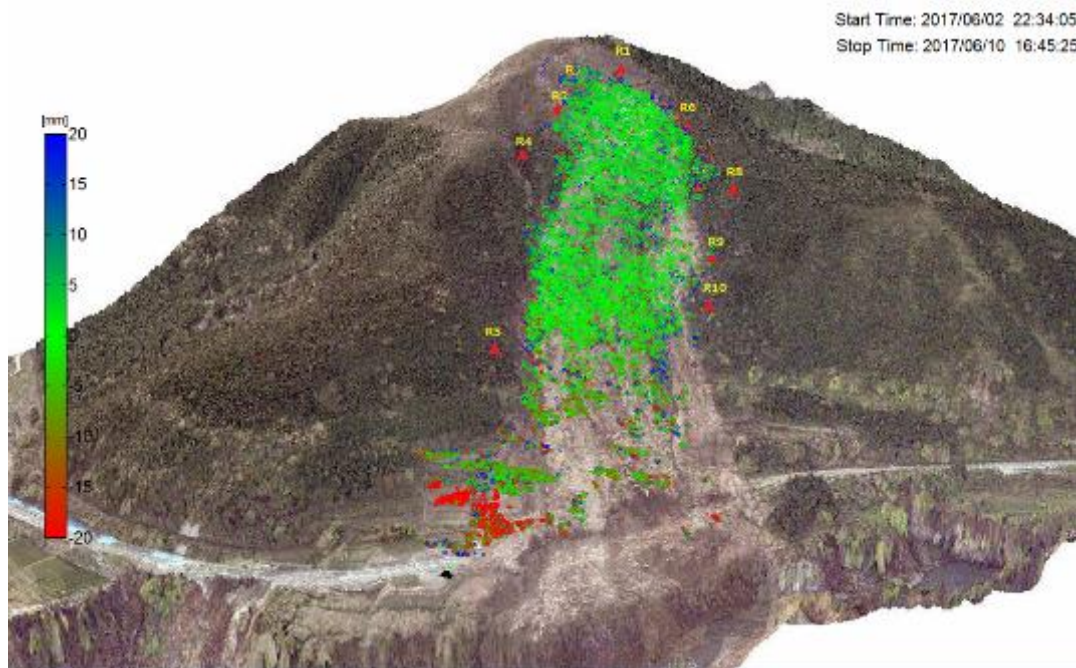
Figure 6.7 real time 2D Displacement map

After completing the secondary signal processing in the monitoring PC in Tohoku University, the estimated displacement was retrieved in two different ways. The first one is the 2D map projected to 3D DEM surface, which updates by every data acquisition. Figure 6.7 depicts the interface of the real time 3D displacement map in monitoring PC. The displacement of the estimated CS point locations were updated every 15 minutes of data acquisition completed by Minami-Aso GB-SAR. The colour scale shows the displacement of each CS points in two alternative directions. The Blue colour represents the movement towards the radar and red colour shows the movement in opposite direction. After road construction projects started, most of the CS points near to the radar has distorted by ongoing project work, which was neglected by known.

The displacement inside the forest canopy become considerable for the stability of untouched soil layer which has less coherency due to frequent movement of tree leaves. Therefore 10 corner reflectors were deployed and monitored remotely. Due to the fast moving tree canopy, three reflectors were loosed its coherency, which was not shown to any CS estimation method. But all other seven reflectors are remained stable and continuously monitored.
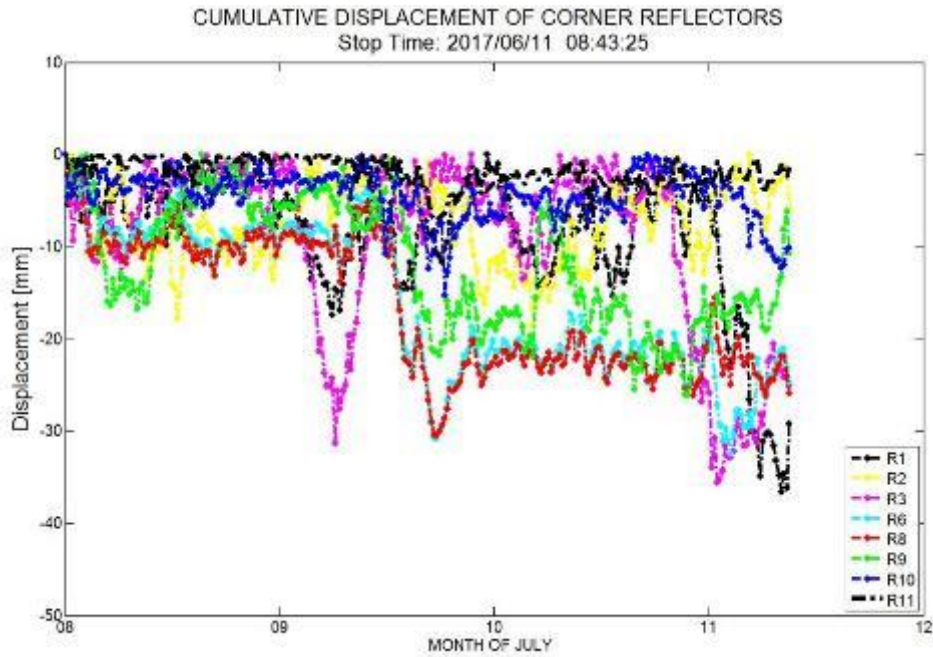
Figure 6.8 Displacement of the cornnerreflector befor rainning season (+10 to -50 mm scale)
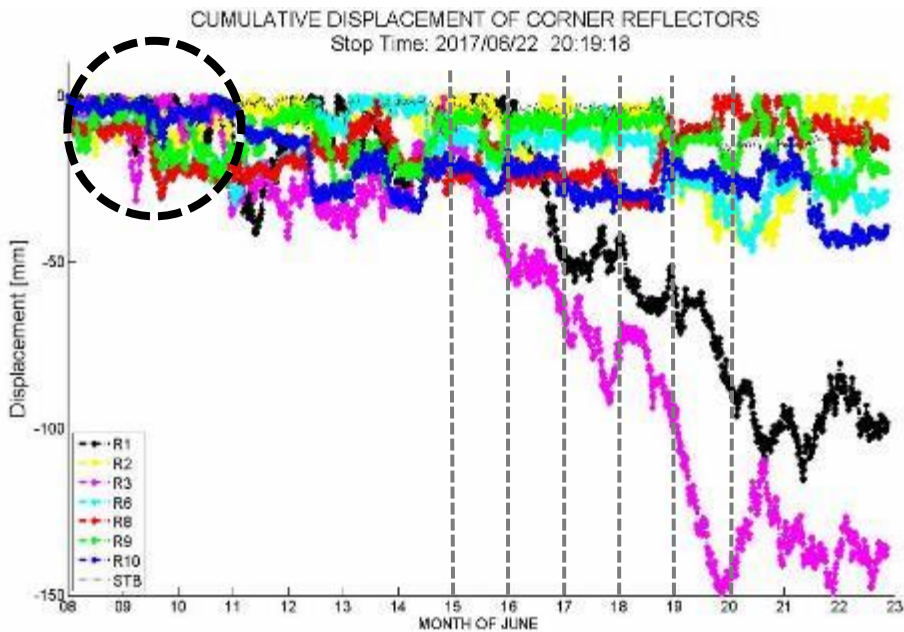
Figure 6.9 Displacement of the cornnerreflector during the rainning season

The real time displacement of the corner reflectors was retrieved in the secondary interface as shown in Figure 6.8. It shows real time monitoring results of 7 trihedral corner reflects out of 10. After starting the raining season in mid of June, R1 and R3 reflectors which locate inside the forest in show considerable movement starting from 15th June until 21st as shown in Figure 6.9.

6.4 Analysis of surface movement by continuous GB-SAR observation

As mention in Chapter 3, the main objective of implementing GB-SAR monitoring station in Kumamoto is to identify the locations which show abnormal displacement with in the landslide area and investigate high possible areas to trigger a sudden slope failure in near future. In Minami-Aso GB-SAR monitoring station, the total coverage area spread around $0.45 km^2$. Since this area is wider and it includes steep slope, dense forest canopy and it's impossible to capture the locations which have high potential to trigger a landslide within total observation area by conventional pinpoint measuring techniques. The GB-SAR has $4.5\,\text{m/rad} \times 0.5\,\text{m}$ ground patch resolution which covers total observation area by 2000 x 404 pixels within minimum 10 s time lag. This makes great advantage to monitor, detect and inform the locations which show abnormal displacement. After finding such location, more precise and accurate ground analysis of particular location can be done using non-remote sensing techniques such as extension meter, inclinometer to find the reason for the displacement in the geological background.

Estimation of displacement by GB-SAR

The theoretical explanation of displacement monitoring by GB-SAR differential interferograms is reminded in the Figure 6.10. The radar is mounted in the fixed position, the left side of the figure and target is located on the right side.
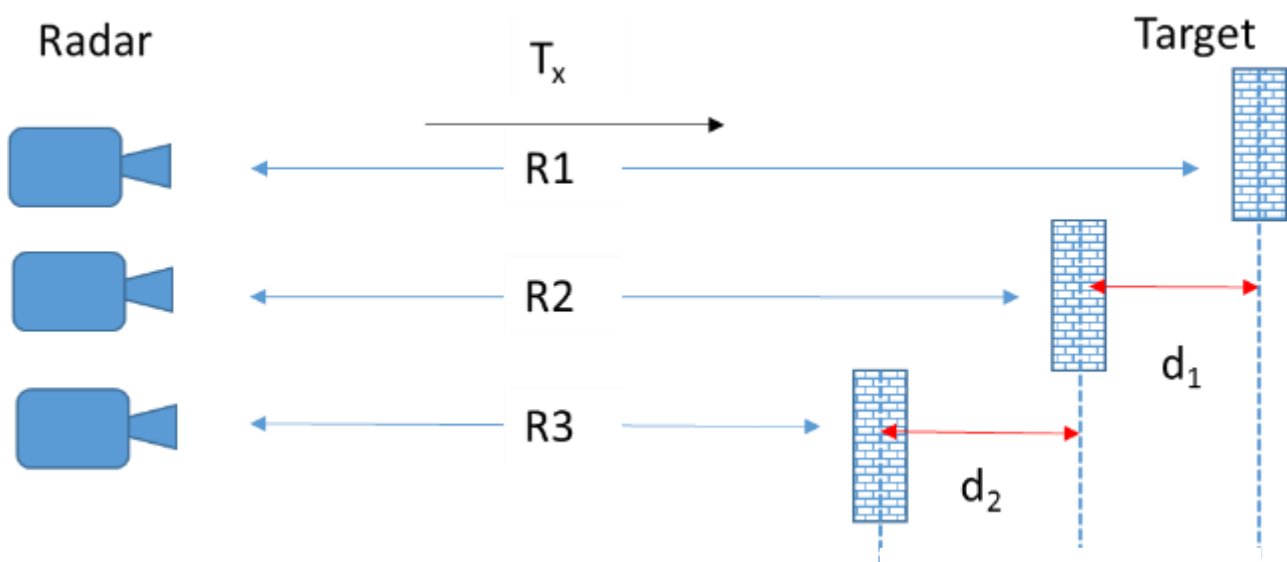

Figure 6.10 The schematic diagram of target monitoring by GB-SAR

where the ϕ_1 is the calculated phase in T_{R1} time and ϕ_2 is the calculated phase in T_{R2} time and ϕ_3 is the calculated phase in T_{R3} time. If we assume the target show random displacement in radar LOS direction, the estimated distance between radar and target is R1, R2 and R3. Therefore, the displacement of the target in the real world can be estimated as $d_1, d_2 \ldots \ldots$. In this derivation, we assumed that the target which moves toward the radar is a negative value (Blue colour scale in 2D maps), the target which moves far from the radar is a positive value (Red colour scale in 2D maps) and the target monitored as a stable in time in green colour scale. By considering the phase of the received EM wave towards the radar, ϕ_1, ϕ_1 and ϕ_3 can be written as,

$$\phi_1 = \frac{2\pi}{\lambda}(2R_1)$$

$$\phi_2 = \frac{2\pi}{\lambda}(2R_2)$$

$$\phi_3 = \frac{2\pi}{\lambda}(2R_3)$$

If we assume that the phase difference does not exceed the $\pm \pi$ (no phase wrapping), the true displacement during the consecutive acquisitions can be estimated as,

$$\phi_{21} = -\frac{4\pi}{\lambda}(R_2 - R_1) = -\frac{4\pi}{\lambda}d_1$$

$$\phi_{32} = -\frac{4\pi}{\lambda}(R_3 - R_2) = -\frac{4\pi}{\lambda}d_2$$

$$\phi_{31} = -\frac{4\pi}{\lambda}(R_3 - R_1) = -\frac{4\pi}{\lambda}(d_1 + d_2)$$

$$\ldots\ldots\ldots\ldots\ldots$$

$$\phi_{n\ldots1} = -\frac{4\pi}{\lambda}(R_n - R_{n-1}) = \frac{4\pi}{\lambda}\left|\sum_{r=1}^{n-1} d_r\right|$$

The total displacement of each CS point in the 2D InSAR image, during the time interval T_{d_1} and $T_{d_{n-1}}$ can be estimated by $\phi_{n\ldots1}$. But in the natural environmental monitoring, the phase change of the each and every pixel will not be considered as a reliable indication of the target movement due to the RCS, a number of noise pixel and the pixel suffered by atmospheric phase screen which describes in Chapter 4. The atmospheric phase screen can be removed by the method described in Chapter 4 and

the noise pixel locations can be removed by considering the relevant CS estimation method in as described in Chapter 5. Those models can be used to minimize observed phase distortions in InSAR pixels, but could not guarantee the 100 % phase compensation. Therefore, in order to enhance the reliability of the GB-SAR remote sensing technique, the acquired data was compared with non-remote sensing techniques for validation.

Estimation of 2D displacement - Spring season

The GB-SAR monitoring of Minami-Aso was started at the end of the winter season in January. In the begging of the measurement in January to mid of June, total monitoring area does not show critical displacement for the GB-SAR observation. During this time period, the few millimetre displacements were detected only in some temporary wall structures (Figure 6.11) in the bottom of the mountain and other places remain stable.
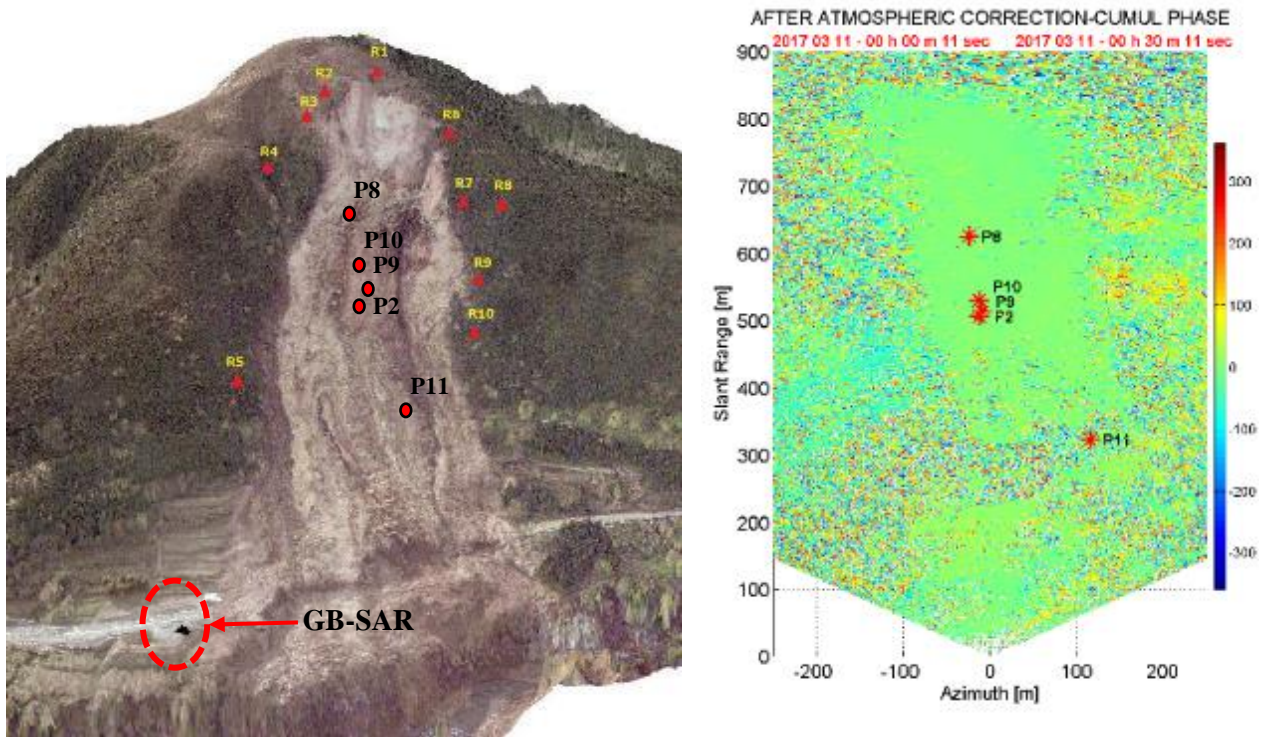
Figure 6.11 Schematic of target monitoring in GB-SAR

The point P2 and P8, P9, P11 were selected from the surface soil layer of the landslide area. Those points show high coherency in interferometric phase. In the 15 days sample data set, P2 and P10 show the similar displacement which was less than 4 mm. But the point P11 on the wall structure was bounded near to the temporary roads which construct to make access to the area in order to remove the deposited debris after the landslide. This process was done using heavy vehicles. Therefore small displacement was recorded from the wall, during the day time in point P11.

118
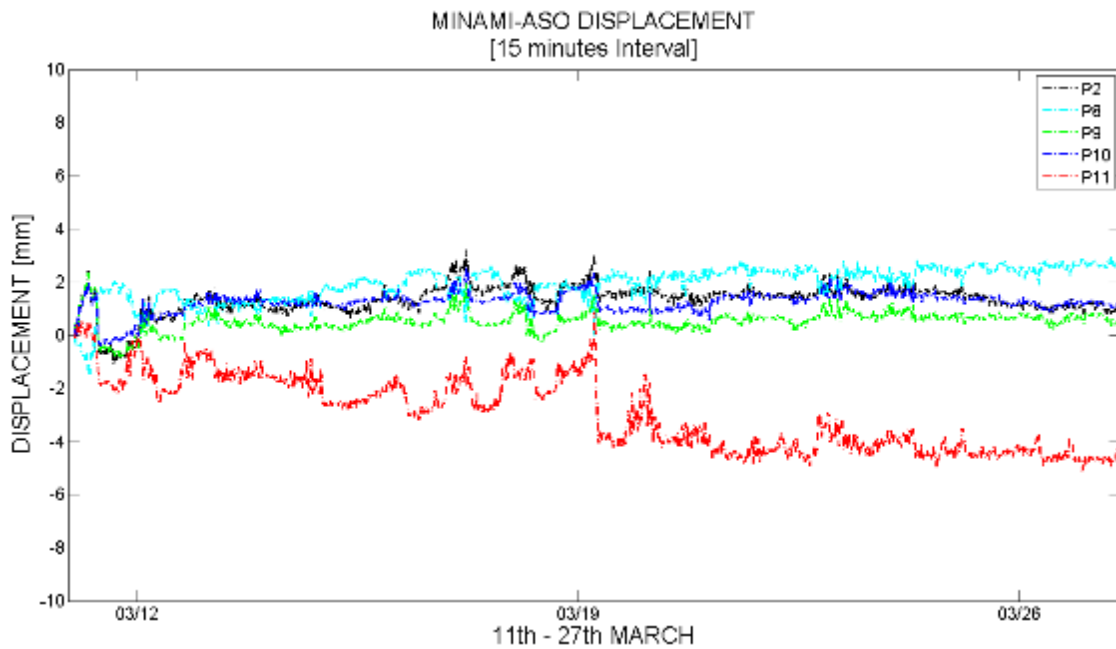
Figure 6.12 Recorded displacement of the coherence points during the 15 days of period

In the mid of June, the rainy season started in the south part of the Japan and it continuously affects for all island during the period of June to August. The Minami-Aso in Kumamoto prefecture, located in south Japan and reportedly start the rain after 15th of June. The continuous GB-SAR measurements were carried-out from the beginning of the year, including the raining season, both before and after. After the earthquake triggered the landslide in Kumamoto, the unstable soil layer was removed after the previous year rainy season in 2016. The stability of crown of the landslide, besides forest canopy during the rainy season was not confirmed by any kind of terrestrial field measurement, after completion of soil removal process. Therefore the GB-SAR monitoring results during the rainy season become a significantly important factor to confirm the stability of entire area for future construction plane. In the other hand, daily construction work continuously is done entire period including extreme weather condition. The access to the installed conventional displacement monitoring system was restricted during the rainy period due to the conditions of the site conditions. Therefore the GB-SAR stand as the only method which renders the reliable remote sensing information from the entire construction site as a real time displacement monitoring system.

As explained in Chapter 5, the displacement inside the forest canopy was monitored by estimating the movement of the trihedral corner reflects located within the GB-SAR illumination area. The reflected signal (Figure 6.10) from the trihedral corner reflector was observed before the raining season and during the rainy season.

Estimation of displacement – Before the raining season

The estimated movement of the corner reflectors was depicted in Figure 6.13 (a) and estimated displacement of the coherent scatters were shown in a green color layer in the 3D model of Minami-Aso area in Figure 6.13 (b). In the estimated movement of the corner reflectors of R1 to R10 does not show the continuous movement before starting the rainy season. They show some sudden fluctuation in displacement axis, which possible due to the sudden change of surrounding area of the corner reflector by movement of tree canopy due to the wind during the GB-SAR monitoring period.
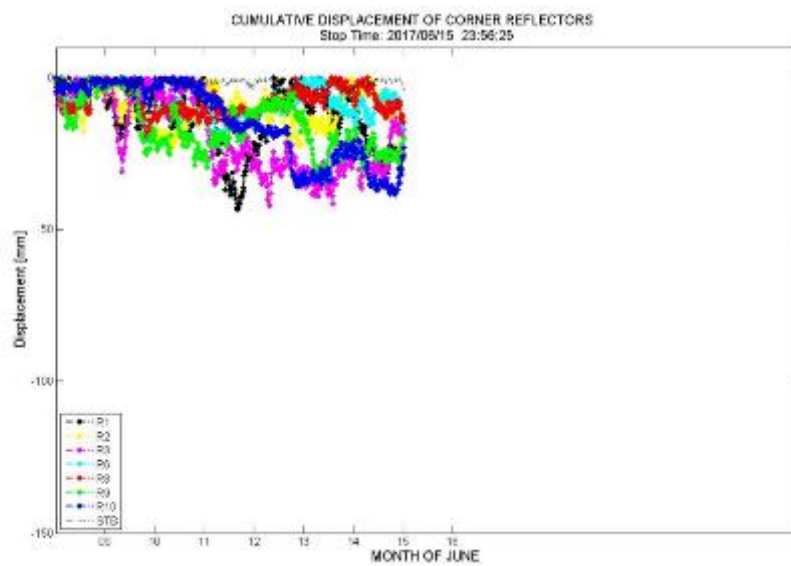
(a)
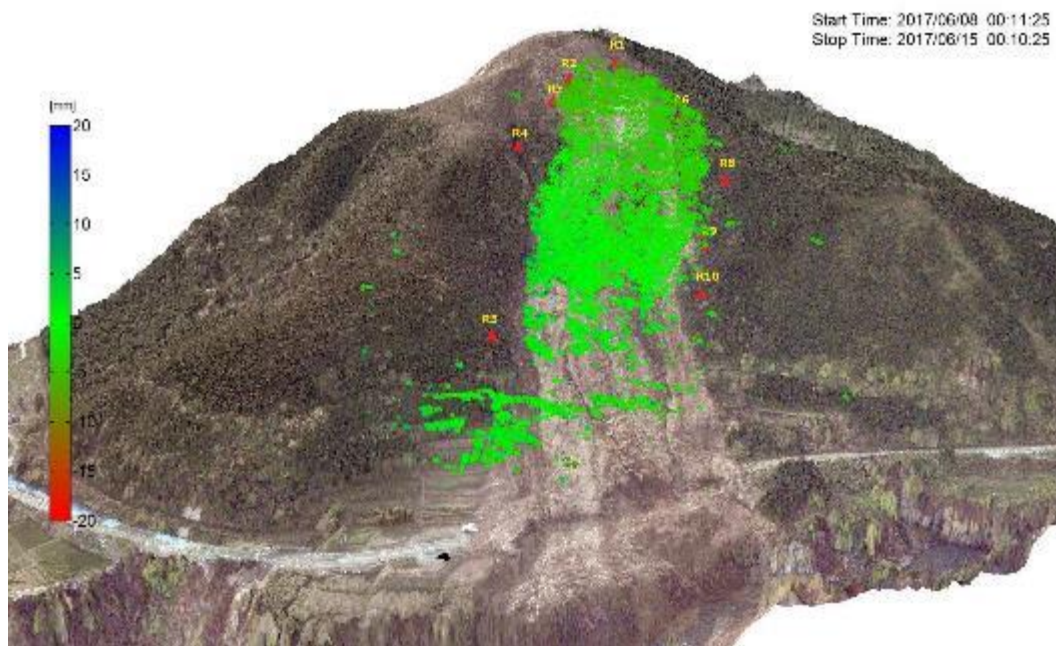
(b)

Figure 6.13 Recorded displacement during 8th to 15th June 2017 of (a) Corner reflectors (b) Coherent scatters

120

But 2D observation in the overall displacement of the coherent scatters in the 3D model (Figure 6.13 (b)) confirm that the no significant movement in particular part or region of the geological boundaries were recorded before starting the rainy season. It further confirms by the green color coded region (zero displacements) overlay on the 3D model in Figure 6.13 (b) which summarize the cumulative displacement from 8th to 15th July 2017 data sample.

Estimation of displacement – During the rainy season
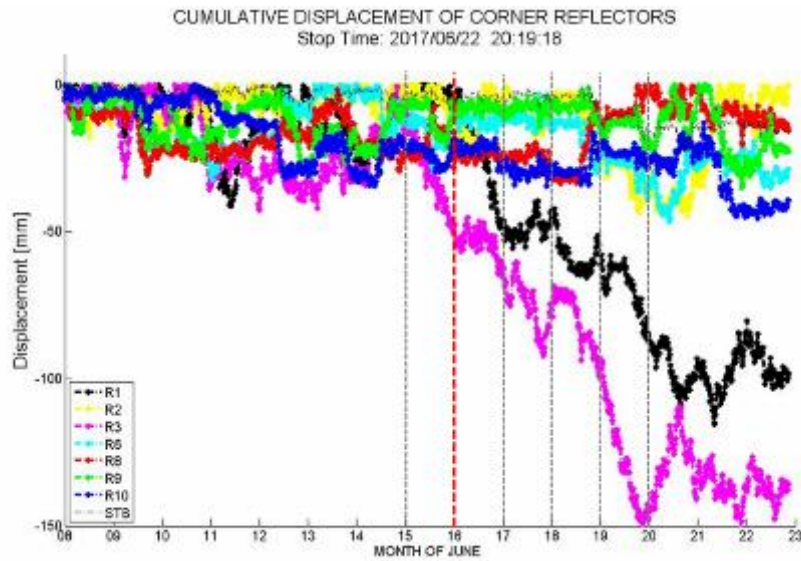
(a)
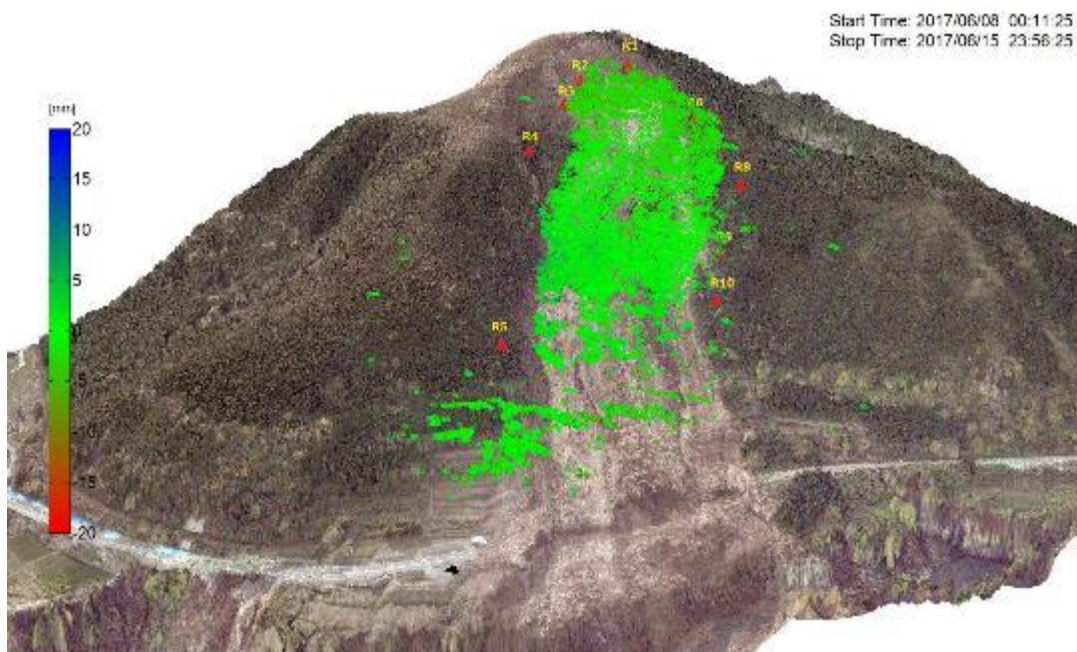
(b)

Figure 6.14 Recorded displacement during 8th to 16th June 2017 (a) Corner reflectors (b) Coherent scatters

The rainy season was started in June and the weather condition of the site was significantly change during the second week of the month. Figure 6.13 (a) shows that the 15th of June as a starting period of the movement in the corner reflector R1 to R10 (except R4, R5 and R7 which permanently loose there coherency due to random movement of surrounding tree clutter was not consider for displacement estimation) and STB coherent point pick from the open soil layer. The red dotted line is shown in the Figure 6.13 (a) to Figure 6.18 (a), indicates the corresponding monitoring time period of GB-SAR and Figure 6.13 (b) to Figure 6.18 (b) retrieve cumulative displacement of the coherent points in the 3D model.
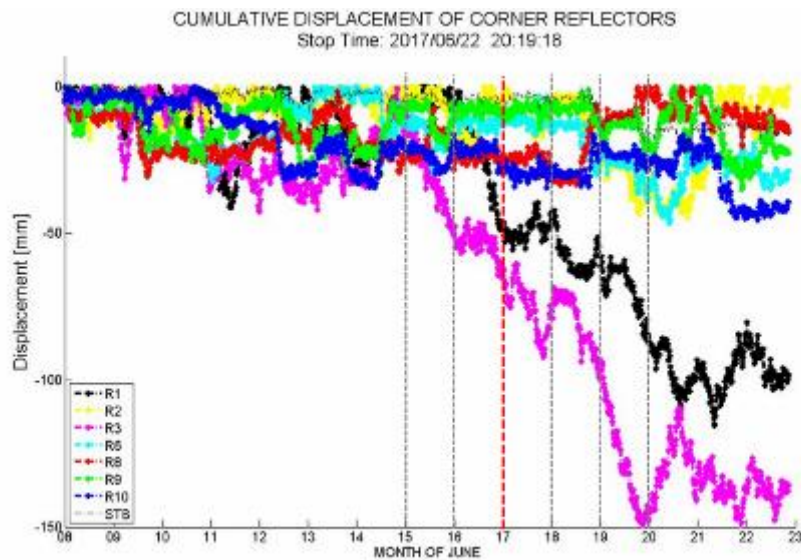
(a)
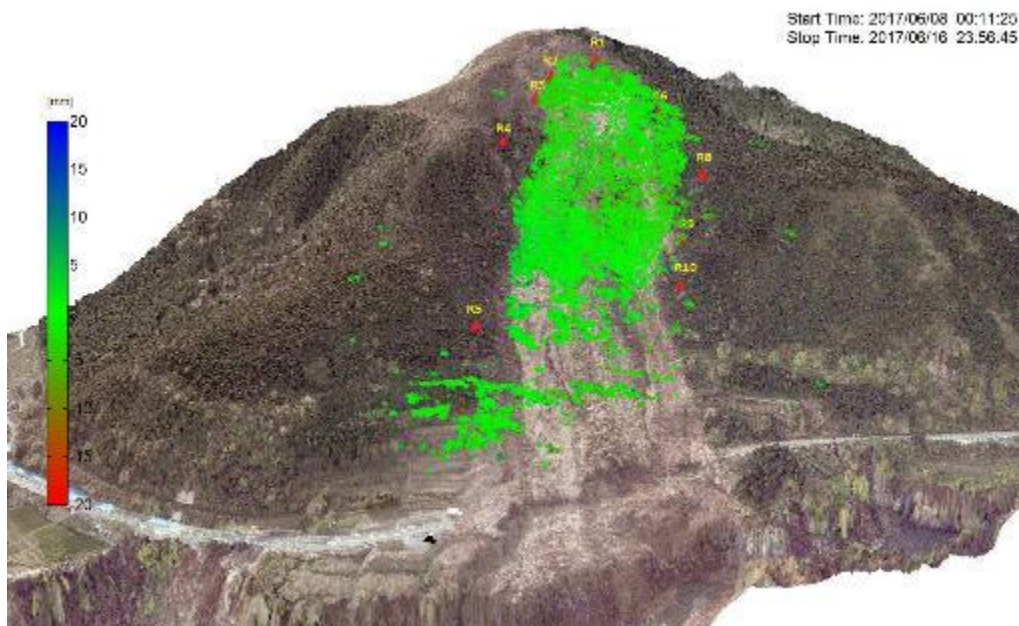

(b)

Figure 6.15 Recorded displacement during 8th to 17th June 2017 (a) Corner reflectors (b) Coherent scatters

122

After 15th of June, GB-SAR monitoring result indicates the considerable movement in corner reflectors. On 15th, the reflector R3 which located in left corner of the crown of the landslide was started to move and end of the day it shows 3.2 cm displacement towards radar LOS direction. But other reflectors which located in different spatial location and different angles towards the radar LOS, including the nearby reflectors R1, R4 and the coherent points were not shown any correlation or considerable indication about displacement during this time period. It concludes that directional movement of the reflector R3 is 308° and it shows 0.0003 m / minute movement. But next 24 hour time period (16th -


(a)
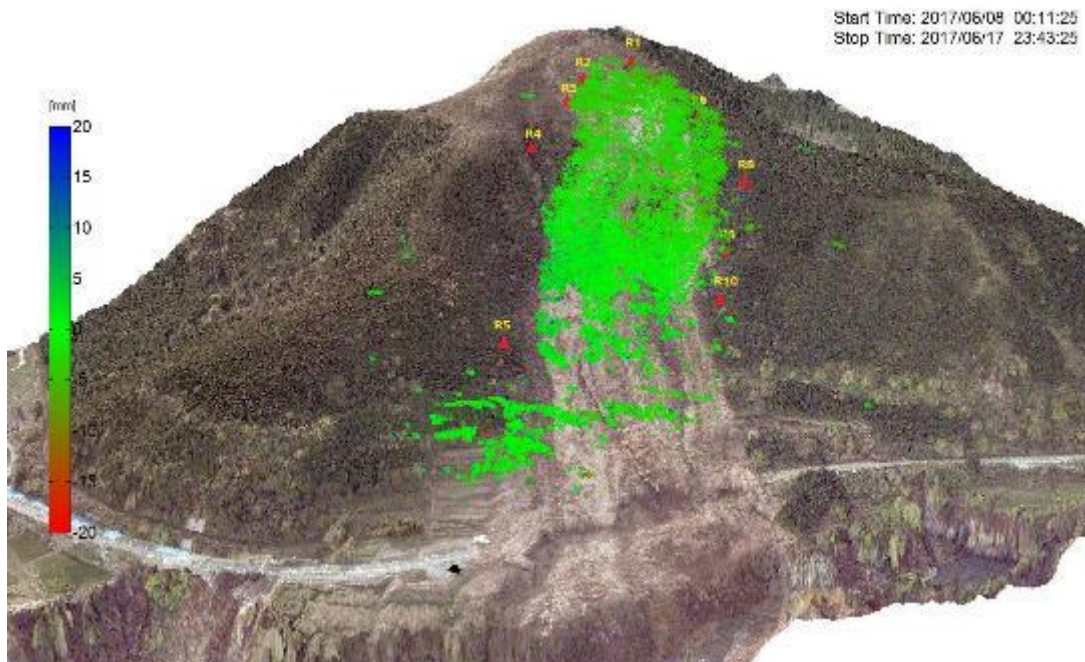
(b)

Figure 6.16 Recorded displacement during 8th – 18th June 2017 (a) Corner reflectors
(b) Coherent scatters

17th June), the R3 reflector moving tendency was dramatically reduced. The other reflectors R2 and R6 to R10 recorded the similar results. It indicates that the no continuous movement can be observed in particular location. In Figure 6.17 (a) shows that the beginning of the day 18th, R2 to R10 reflectors did not indicate any continuous movement. Moreover, the rain was not recorded in this day and weather conditions of the Minami-Aso area become stable. Figure 6.18 (b) depict the cumulative displacement of coherent scatters during 8th to 19th June, 2017. It confirms that the no significant displacement in particular part or region in the post-landslide area was recorded during the period.
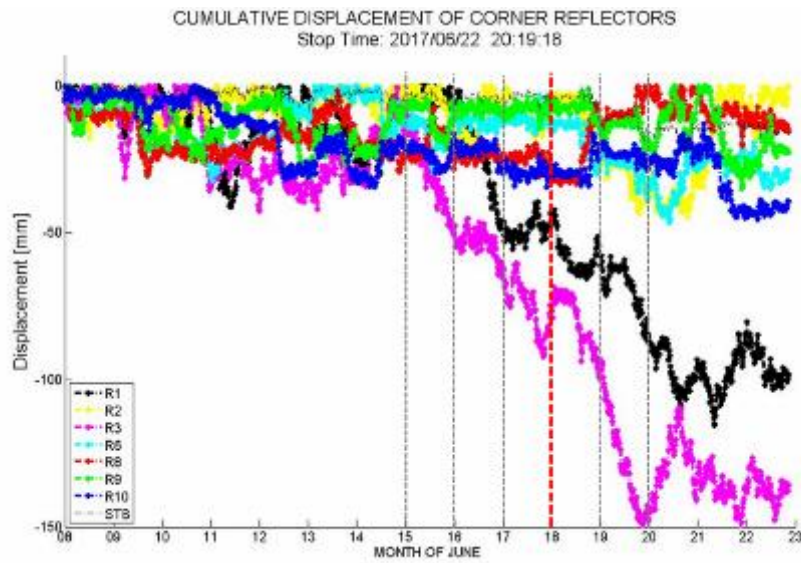

(a)
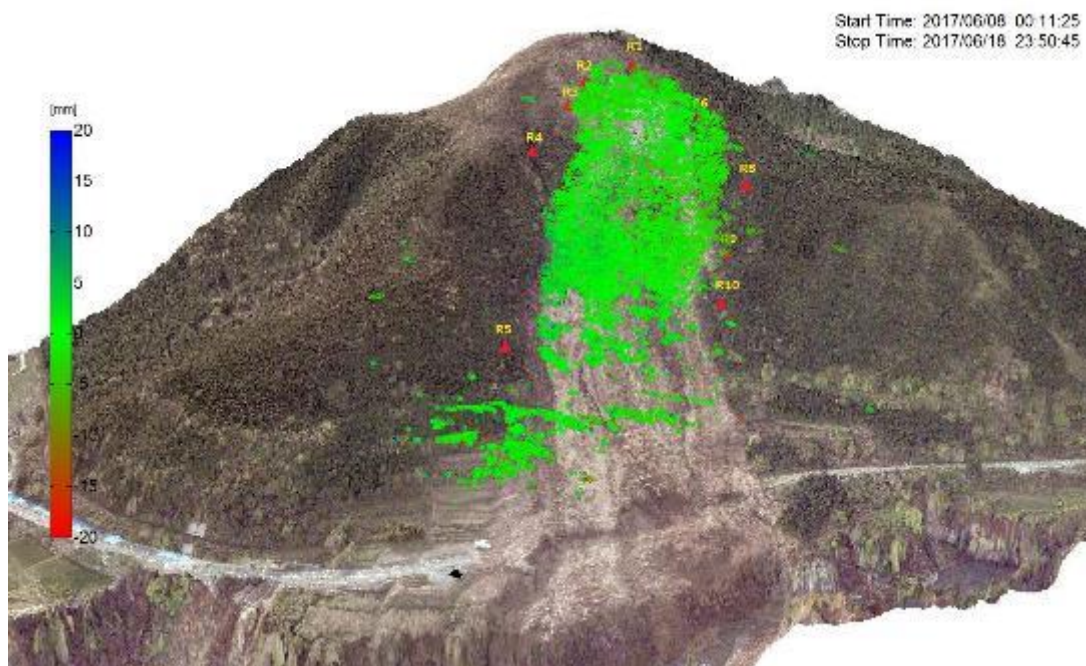
(b)

Figure 6.17 Recorded displacement during 8th – 19th June 2017 (a) Corner reflectors
(b) Coherent scatters

The coherent scatter were depicted in the Figure 6.18 (b) indicate the considerable displacement in the crown of the landslide at the end of the day 20th of June. The blue colour scale emprise that this area moved toward the GB-SAR sensor direction. The similar indication can be observed in the corner reflectors (Figure 6.18 (a)) inside the forest area. But the movement of the corner reflectors and estimated displacement of the coherent scatter show diverse scale for displacement measurements. Therefore, we compare this results with the field measurement in order to distinguish the factors which effect for movement of the corner reflectors and displacement of coherent scatters.
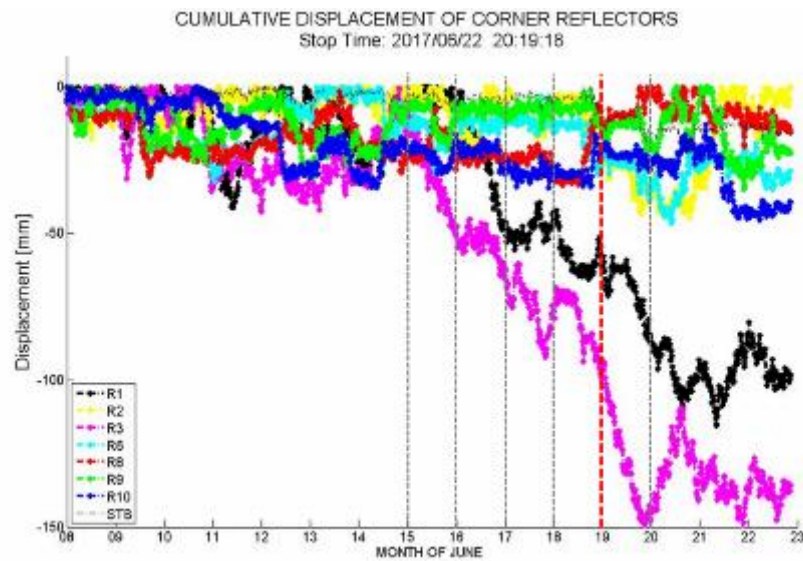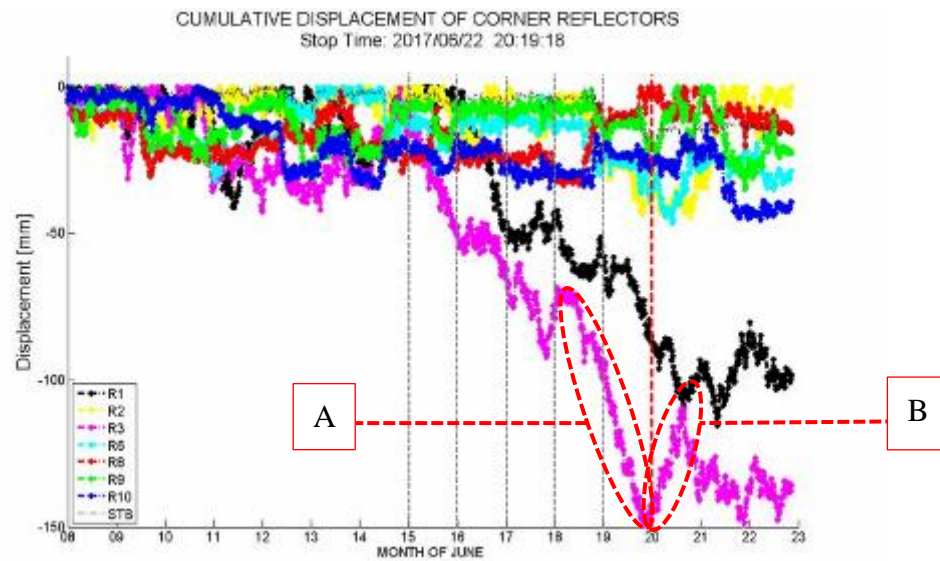

(a)
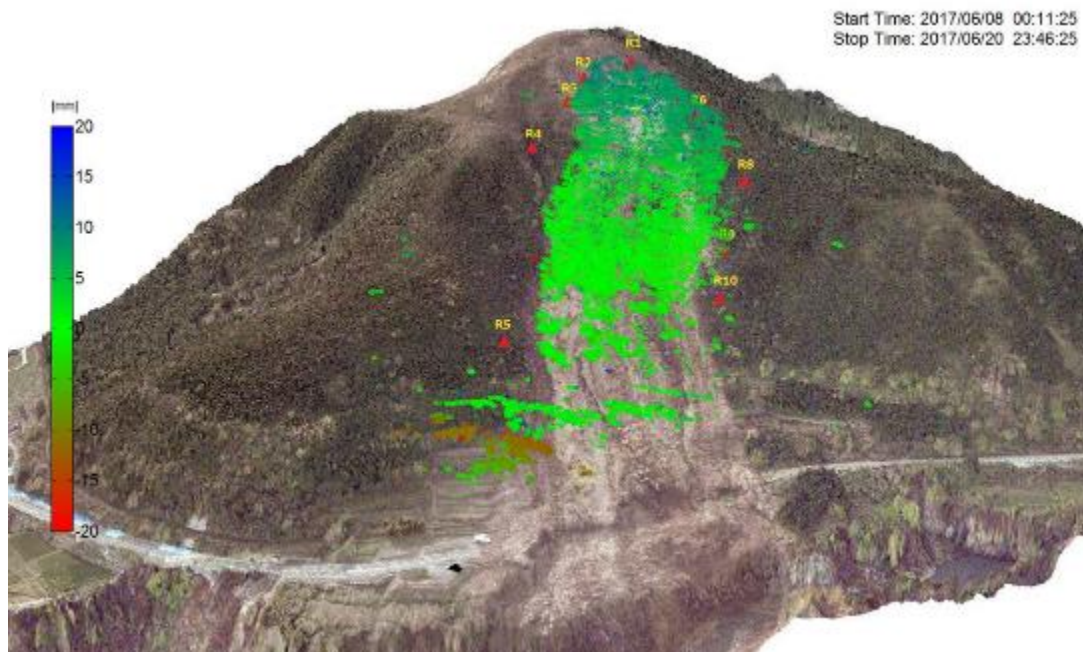
(b)

Figure 6.18 Recorded displacement during 8th – 20th June 2017 (a) Corner reflectors
(b) Coherent scatters
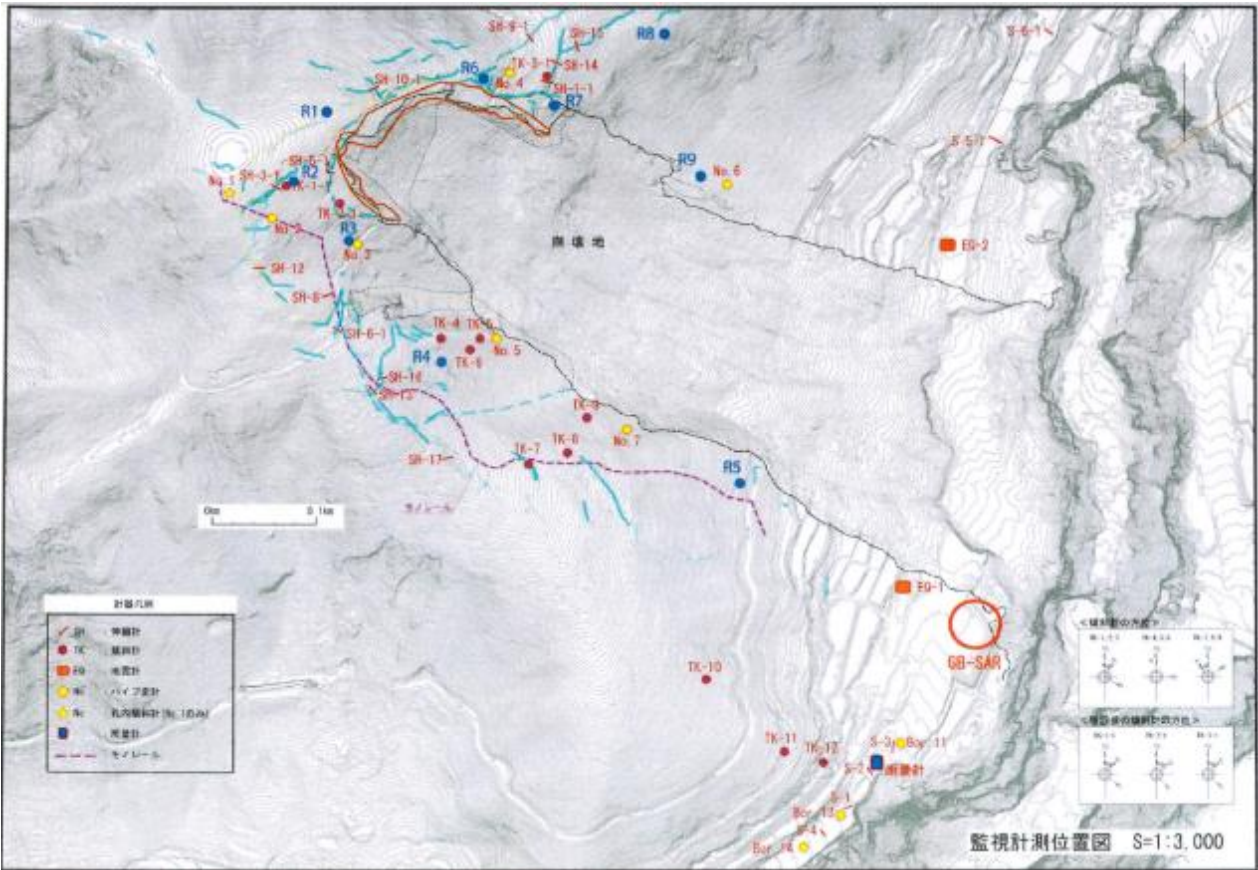
Figure 6.19 Locations of displacement measuring instruments

The terrain map of the main landslide and surrounding area depicted in Figure 6.19. Due to the instability of the top region of the mountain and newly created fractures (blue colour lines) zones, a number of surface movement measuring techniques were implemented in most critical locations. In order to observe lateral movement in fracture zones, the extensometer measurements were examined. The installed extensometer, inclinometer area are depicted in orange colour and red colour dots in the figure 6.19. The GB-SAR measurements show considerable displacement in the crown of the landslide during the rainy season during 15th to 21st July 2017 [8].

Table 4 Extensometer reading during 2017/06/08 to 2017/06/21

Reading #	Extensometer	Displacement (mm)	Nearby CS/corner reflector
1	SH-3-1	0.3	CR 2
2	SH-9-1	0.6	CR 6
3	SH-15	0.4	CS 1
4	SH-16	0.6	CR 3
5	SH-17	0.4	CS 2

Normalized value for observed displacement
2017/06/08 to 2016/06/21
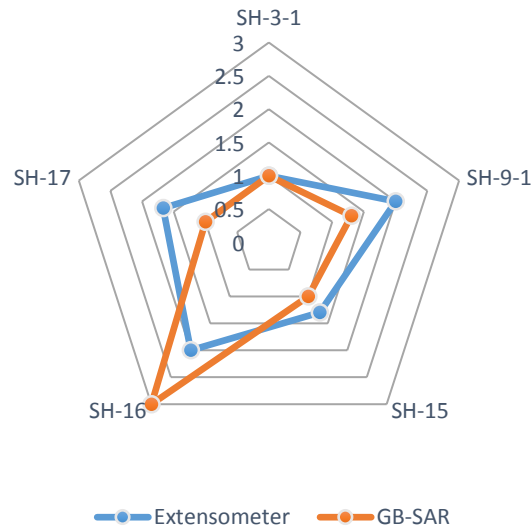
(a)

Figure 6.20 Comparison of Extensometer meter measurements and displacement of coherent scatters estimated by GB-SAR

In this campaign, GB-SAR was operated as a real-time remote landslide early warning system which monitors the large area with in short period of time. The main objective of implementing GB-SAR monitoring station in Kumamoto is to identify the locations which show abnormal displacement with in the post-landslide area and further investigate high possible areas which could trigger a sudden slope failure in order to prevent any deleterious situation to the people who actively involve with road reconstruction work in the bottom of the mountain. This situation quite similar to the GB-SAR deployment in Open-pit mining industry all over the world. There, the measurement accuracy of the each and every DInSAR image pixel and its movement was not considered as a critical issue since the overall 2D displacement image can distinguish the area which is stable and an area which has high potential to triggered slope failure.

But in the case of post-landslide monitoring sites like Minimi-Aso, the probability of trigging another landslide is minimum. Therefore the accuracy of the estimated displacement also important in order to estimate the long term stability of critical areas like fracture zones. Table 4 summarized the displacement data measured by extensometer [8]. Figure 6.20 depicts the comparison of extensometer measurement and estimated the movement of the nearby coherent point. The extensometer readings indicate the lateral movement between fracture locations which bound between lower scales.
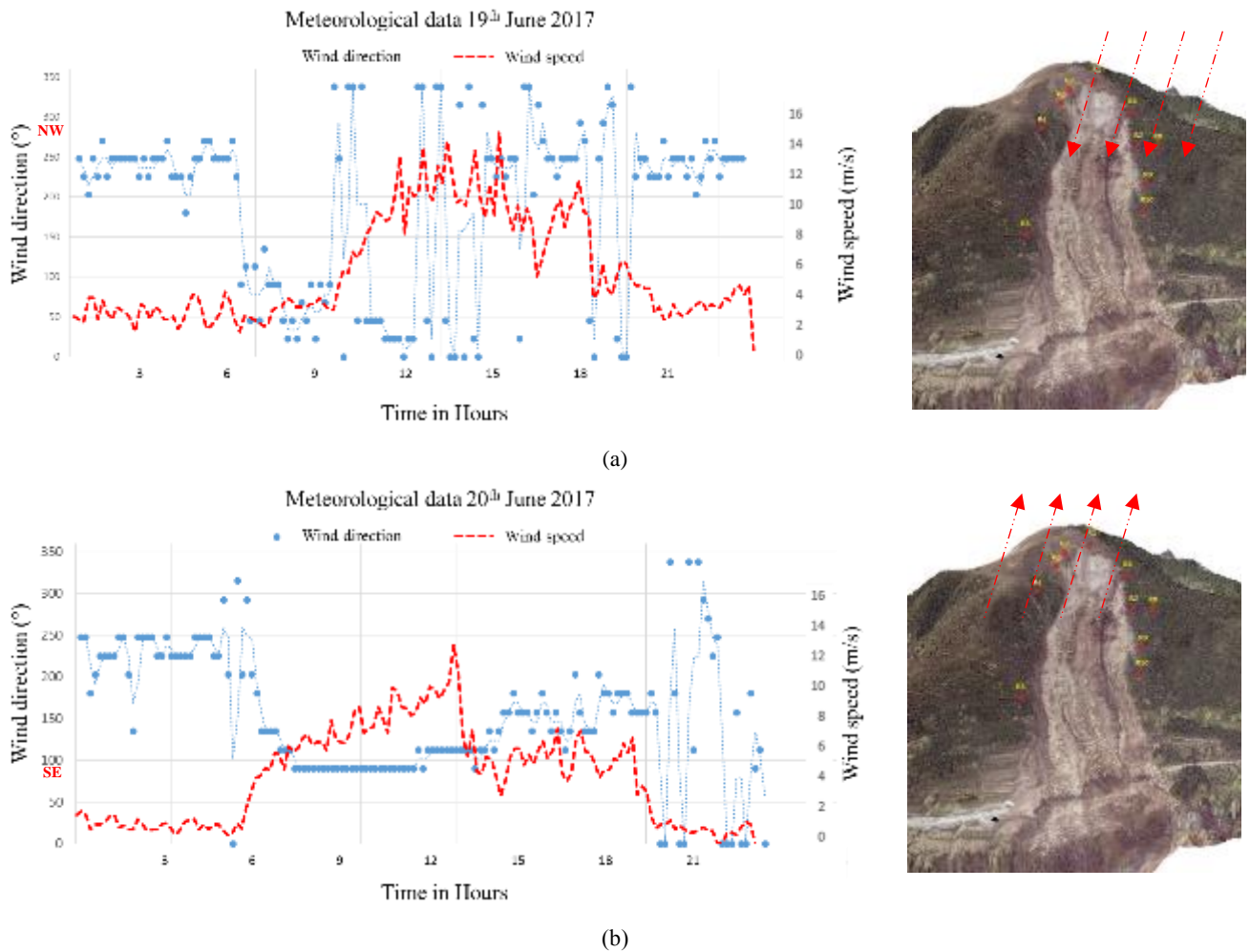
Figure 6.21 Meteorological data, wind speed and wind speed during (a)19th and (b) 20th June 2017

The displacement of nearby coherent points shows relatively high values by comparing with GB-SAR measurements. But the normalized values of both equipment show some correlation in Figure 6.20 SH-3-1, SH-9-1 and SH-15 for scaling factor 30. This could happen since the GB-SAR measure the displacement in radar LOS direction but field measurement has a slight deviation, which can be estimated by terrain slope information in future. But extensometer meter SH-16 and corner reflector point R3 show clear difference since the R3 show movement in alternative directions in Figure 6.18 (a) marked in A and B. This was not shown in interferometric results in Figure 6.18 (b) and only affect for the corner reflectors. Theoretically, this kind of phase accumulation could be occurred (Figure 6.10) if the corner reflector undergoes a vibration by an external force, such as strong wind. The meteorologically data in nearby weather station recorded that on 19th, the fast wind flow (Figure 6.21 (a) during 09:00-2100) move towards the radar by the direction North-West direction and 20th of June, the fast wind (Figure 6.21 (b) during 06:00-19:00) move outwards the radar by South-East direction. It adds additional phase error which does not relate to ground displacement. This kind of errors can be overcome by averaging the multiple CR phase components prior to estimate the displacement in future.

6.3.2 Automatic landslide early warning system

Automatic cluster movement tracking system

In practical manner, requirement of automatic early warning become highly necessity in order to send the message to the people who are involve in road construction work. In this automatic early warning system, the upper part of the radar illumination area in the landslide location was divided into 12 clusters and mean displacement of each cluster was dynamically calculated. If the displacement exceed the threshold level of 1 mm per hour, the monitoring PC generate automatic email and send to responsible parties to investigate the area by site inspection.
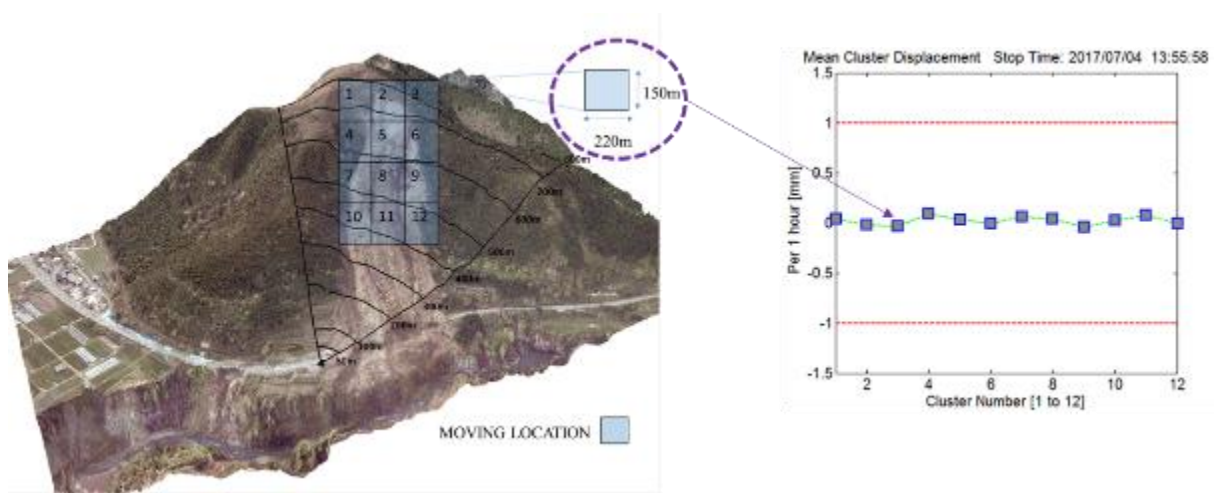

Figure 6.22 Autmatic cluster displacement tracking system

Automatic email system
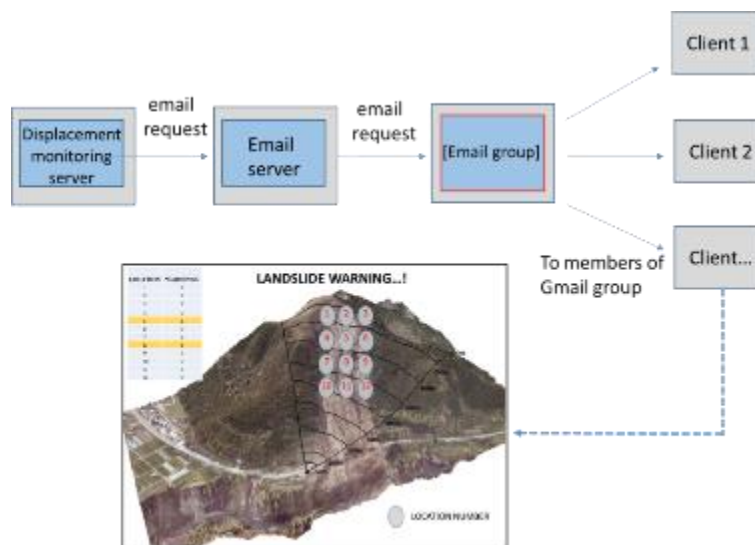
Figure 6.23 Autmatic warning system

129

6.5 References

[1] G. Luzi, M. Pieraccini, D. Mecatti, L. Noferini, G. Guidi, F. Moia and Carlo Atzeni, "Ground-based radar interferometry for landslides monitoring: Atmospheric and instrumental decorrelation source on experimental data," IEEE Trans. Geosci. Remote Sens., vol. 42, no. 11, pp 2454-2466, November 2004.

[2] G. Nico and J. Fortuny, "Using the matrix pencil method to solve phase unwrapping," in IEEE Transactions on Signal Processing, vol. 51, no. 3, pp. 886-888, March 2003.

[3] R. F. Hanssen, Radar Interferometry: Data Interpretation and Error Analysis. Dordrecht, The Netherlands: Kluwer, 2001.

[4] M. S. Seymour and I. G. Cumming, "Maximum likehood estimation for SAR interferometry," in Proc. IGARSS-Surface Atmospheric Remote Senseing: Technologies, Data Analysis Interpretation, Aug. 8-12, 1994, vol. 4, pp. 2272-2275.

[5] E. K. Smith Jr. and S. Weintraub, "The constant in the equation for atmospheric reflective index at Radio frequency," Proc. I. R. E, pp 1035-1037, October 1953.

[6] O. A. Alduchov and R. E. Eskridge, "Improved Magnus form approximation of saturation vapor pressure," Journel of applied meterology, vol. 35, pp. 601-609, April 1996.

[7] Real-Time Processing Within MATLAB, online help guide "https://www.mathworks.com/help/supportpkg/rtlsdrradio/ug/real-time-operation"

[8] M. Torii, field observation data, Graduate School of Science and Technology Kumamoto University, Implementation Research and Education System Center for Reducing Disaster Risk (IRESC).

[9] Online data achieve, Japan Meteorological Agency (JMA) http://www.jma.go.jp/en/warn/f_4343300.html

Chapter 7 Feasibility study report for GB-SAR operation in Sri Lanka

7.1 Inland Landslide problem

Human Settlement pattern of Sri Lanka has been evolved from the agriculture based on the lower elevation area in dry zone to a plantation based in hilly Figure 7.1 (a) and wet zone to urbanization based urban-rural co-existence. During the period of British rule (1815-1948 AC), the plantation economy dominated large sections in highlands which were the back bone of the country's economy until recent time. Meanwhile, in these periods central part of the country was considered safe for human settlement even though landslide events occurred. Due to the increase of a number of landslides and the higher number of landslide victims are considered as threatened to human settlement.

Most of the landslides, slope failures, rock fall and cutting failures reported in the elevation greater than 300 m which classified as a central hilly zone in basic geographical zone mapping. According to the government report, The ten main districts Badulla, Nuwara-eliya, Rathnapura, Kegalle, Kandy, Matale districts in the central hill zone and Kalutara, Matara, Galle and Hambantota districts in the southern part of the country identified as the area prone to landslides. Among those districts, the Kandy, Nuwara-eliya, Rathnapura, Kegalle, Kaluthara and Badulla identified as a most frequent landslide reported districts which depicted in below Figure 7.1 (b).

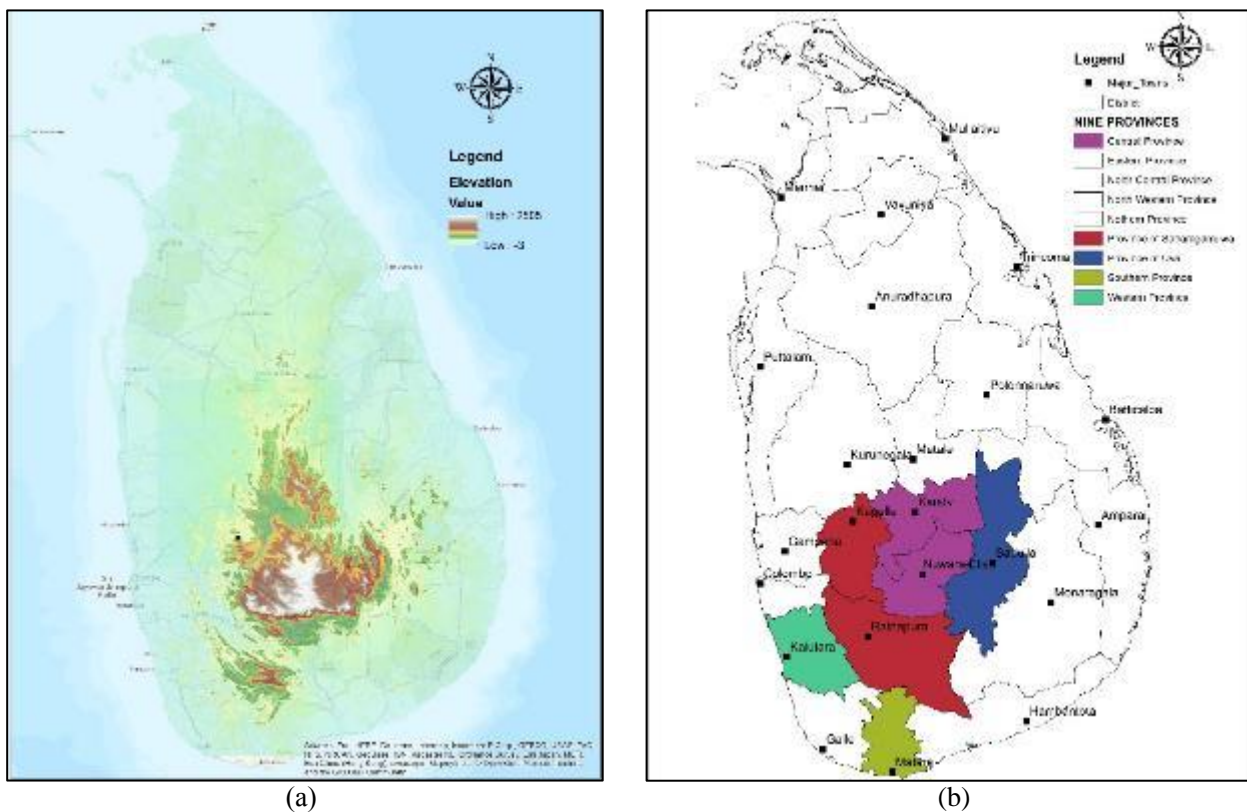|	
(a)	(b)

Figure 7.1   (a) The elevation profile of Sri Lanka (a) extensometer (b) stringauge

Landslides related to heavy rainfall caused widespread property damage and occasional loss of lives. During the last ten years it has become evident that the most devastating landslide events tend to occur as a result of comparatively short duration, high intense rainfall compared to the previously had lower intense prolonged rainfalls in Sri Lanka. Due to the relative location within the tropics and in the Asiatic monsoon region, the climate of the island could be characterized as both tropical as well as monsoonal. The monsoonal weather of Sri Lanka is dominated by the South-West and North-West monsoons. The South-West monsoons occur from May to September and North-West monsoons occur from December to February. The inter-monsoon periods are from March to April and from October to November. The annual rainfall of Sri Lanka also shows a remarkable spatial variation, ranging from 1000 mm in the driest parts to more than 5000 mm in the wettest parts.

The cost of rainfall triggered landslides are not well documented in early stages, but recently it has been increased rapidly due to change of climatic condition and weather pattern. Global climate change is possibly impacting the frequency of landslides in the world and will continue to do so in the future. Climatic conditions predicted from worldwide global warming involve new precipitation and wind conditions. These will significantly affect the amount and type of vegetation, groundwater levels and surface water levels. All these factors will affect the stability of certain natural slopes due to losses of soil suction, higher groundwater tables, and increase in seepage velocities, frequent occurrences of rapid drawdown conditions, losses of soil reinforcement contributed to roots and losses of stabilizing materials through erosion from flooding. In Sri Lanka, the background for a landslide to move down a slope is created by the action of various environmental factors and undue human activities persisting for long periods is finally triggered by intensive rainfall to a landslide. The heavy rainfall not only causes water penetration into the sub soil layers, thereby losing the interlayer cohesion but also increases the weight of soil mass. The penetrated water also acts as an easy lubricant flowing down the slope. The net effect of these processes is the sliding of the soil mass down the slope as a landslide. According to preliminary investigations carried out, it has been found, that if a hill slope receives continuous rainfall of about 200 mm within a period of 3 days, the susceptibility to land sliding in such an area increases. It has been observed that as a result of the current poor, ill-planned land use practices, even a rainfall of 75-100 mm for a 2 day period is sufficient to trigger a landslide.

According to the recent records, it is very seldom for a landslide to occur of a flat of a plain, the obvious reason is that there is no space of opportunity for any soil mass in the area to fall or slide anymore. However, landslides reported in such terrain too, but that can only happen due to an excessive weight or pressure placed on top of the hill slope, the tendency for landslide increase. The slope surface with

133

thick soil layers and slope angle between 15 and 45 have been identified as a greater preponderance for earth movement with the maximum tendency of hill slope of angle 26 to 35 to the horizon.

7.2 Catastrophic landslides recorded in past two decades

Diyanilla landslide

In January 2007 with the high intensity rainfall experienced by the central part of the country especially around the Nuwaraeliya district major scale landslide was occurred in Diyanilla area. Landslide area is belonging to 526-A Palalpathana GN divisions of Walapane divisional secretariat area. The inferred area of this landslide located at Lidesdale Estate (Longitude 800-52.053'E, Latitude 7002.207'N) belongs to Walapane DS division in Nuwaraeliya District. The average elevation of this location is about 1500m from the MSL

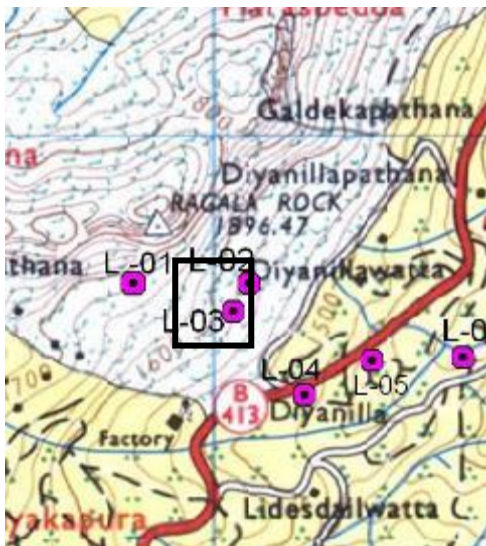Figure 7.2 View of the Mahawewa landslide, Srilanka

Mahawewa landslide

Landslide is located at Mahawewa belonging to Kubalgamuwa GS division of Walapane DS division in Nuwaraeliya District. The average elevation of this location is about 1000m from the MSL and it forms a steep scarp slope.

Figure 7.3 affected house during 2007 incident-crack develop arbitrary manner on loose old landslide, Srilanka

Aranayake landslide

Koslanda and Aranayake devastating landslide were identified as a most recently triggered large scale catastrophic landslides in recent history in Srilanka. The village of Koslanda in the Haldummulla division, 190 km from the capital, Colombo, the landslide was triggered on 29th of October 2014, by monsoon rains and was about 3 km long.
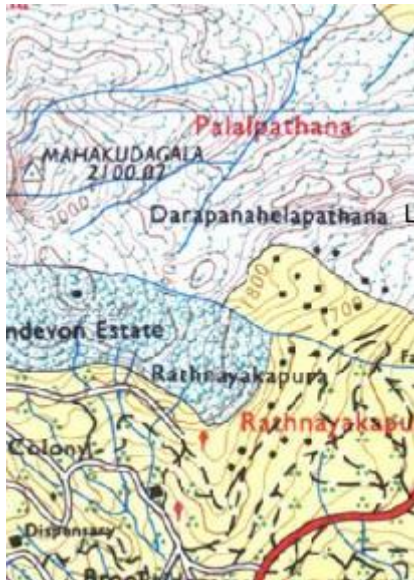

Figure 7.4 View of the Aranayake landslide, Srilanka

7.2 Challenges in existing landslide monitoring system

The rain was identified as critical condition for triggered landslide. Therefore, most of the probable landslide area equipped with range loggers. Apart from that, most critical landslide locations were erupted with extension meters and incliner meters as shown in the figure. Since all of this techniques are pin-point measurements, impossible to understand entries movement of the area by limited number of pin point measurements.

(a)   (b)

Figure 7.5   existing landslid monitoring method (a) extensometer (b) stringauge

135

7.3 Model survey for GB-SAR deployment

The field observation of resent landslide locations in Sri Lanka realized that conventional monitoring techniques has number of problems to react on growing land slide and sudden slope failures. Those problems are,

 ➢ Large number of equipment require to observe land moving pattern of small area,
 ➢ Impossible to deploy unstable steep terrain,
 ➢ Need to spend more time and manpower for daily site visit for data reading,
 ➢ Equipment location and land area cannot be used for secondary purpose,
 ➢ Trained manpower need for data interpretation
 ➢ Equipment are inaccessible for critical weather condition,
 ➢ Average re-usability of the equipment is lower,
 ➢ Far field observation is impossible,
 ➢ Imposable to operate as a real time early warning system.

All of those above problems can be overcome by the ground based remote sensing techniques. The system can obtain data up to 4 km distance in range direction in single SAR scan. Therefore we proposed GB-SAR for landslide monitoring is the most appropriate solution for landslide problem in Sri Lanka. It can use to monitor any type of terrain movement, especially in mountain areas. Figure 7.6 shows elevation profile of mountain area Sri Lanka.
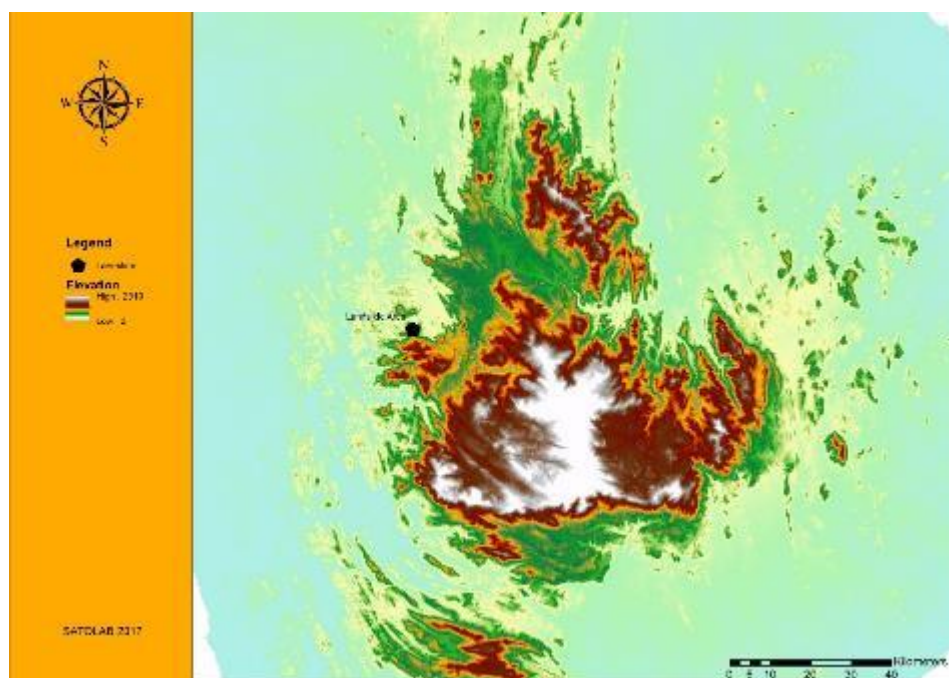

Figure 7.6 Central mountain region

We have conducted a model survey in order to check the system compatibility for real time monitoring. We selected the location in Aranayake divisional secretariat division, 'Samasara kanda' for the model survey. From long term GB-SAR monitoring experience in different areas in Japan, we have understood that success of real time landslide monitoring process and landslide early warning system implementation become more reliable on following background infrastructure,

➢ Clear visibility of monitoring area in LOS,
➢ Very stable horizontal ground platform for equipment installation,
➢ The data transfer rate > 5 Mbps for real time data transferring,
➢ Full time A/C power supply (In case of sudden power failure, system already contain battery power up to 8 hour),

In the model survey, we have testified above factors to find the appropriate location for GB-SAR installation. We locate the every cellular tower locations in Aranayake and nearby locations. Thereby we categorized places which has acceptable data transfer rate into -30 dB, -50 dB and -80 dB by considering the areal distance to the tower location. In this area, most of the houses near to the main road (Figure 7.7) available with the A/C power supply. This becomes positive factor to access very stable domestic power grid, which can further extent without any additional cost. Furthermore, geographically high elevation location leads to reduce the external cost for platform height. By considering those factors, we have proposed 3 locations; GBSARLc1, GBSARLc2, and GBSARLc3 for appropriate places for system installation as shown in Figure 7.7.
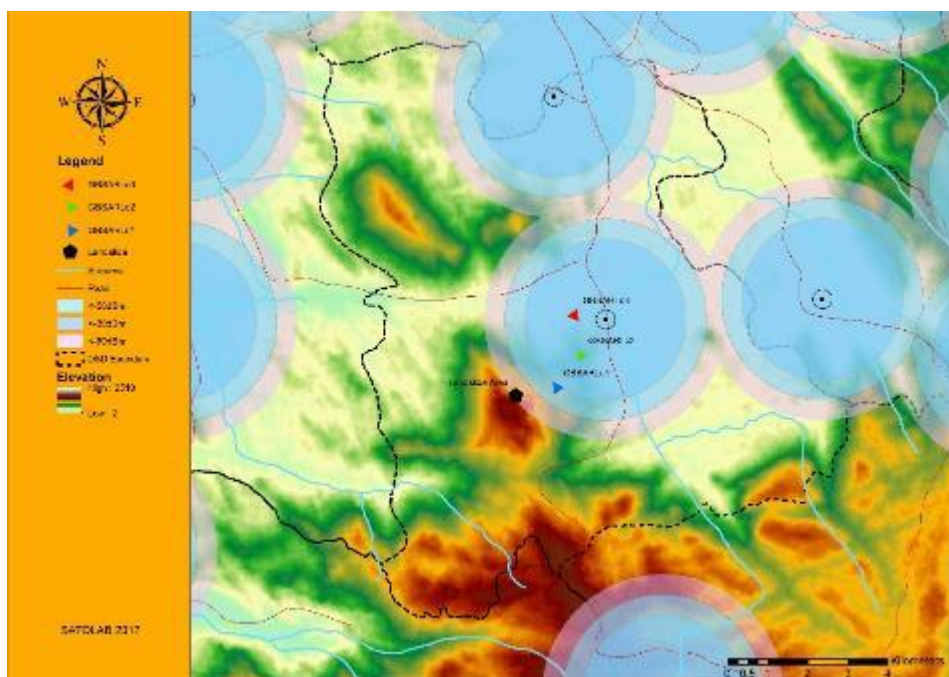

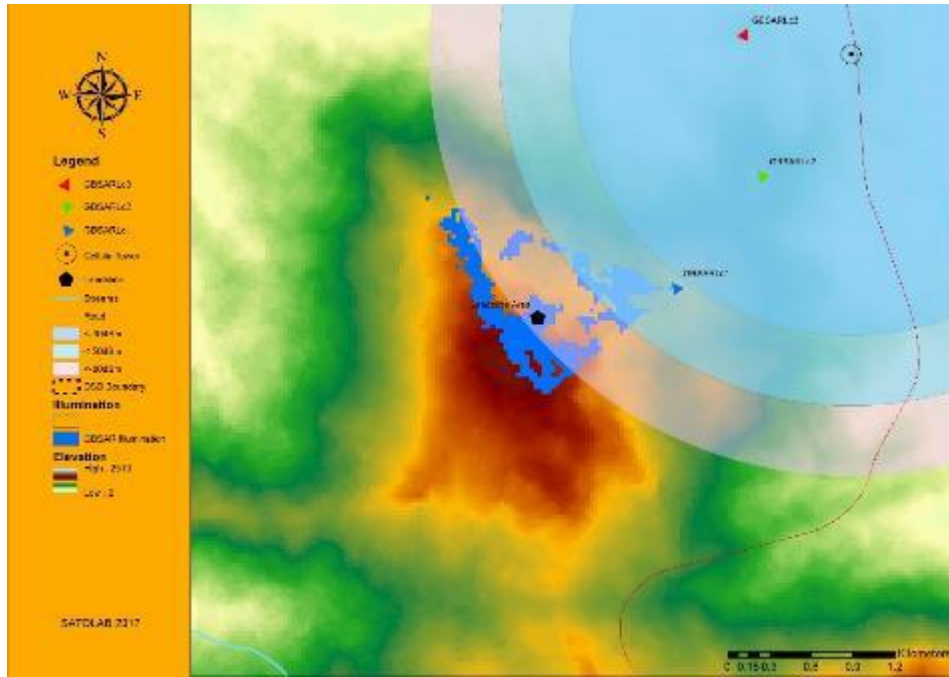Figure 7.7 Proposed location for GB-SAR installation

Figure 7.8 Expected illumination from GBSARLc1

The computer simulation method describes in Chapter 3 was used to estimate the expected illumination from in each location. Figure 7.8 shows the estimated GB-SAR illumination results for GBSARLc1 location. The expected illumination can be further optimized by increasing the platform height into 2 m and setting the azimuth angle into 260 degrees and view angle in 5 degrees. The table shows the summary of proposed GB-SAR hardware installation parameters based on this model assisted survey. In addition to those system installation parameters, the Frequency licenses for 17.1 GHz – 17.3 GHz range for GB-SAR has to apply.

Table 1. Proposed parameters for GB-SAR configuration

Installation location	Latitude	Longitude	Radar Range (m)	Base height (m)	Azimuth angle (°)	View angle (°)
Loc1	80.442°	7.153°	700	2	260	5
Loc2	80.448°	7.16°	1000	5	240	0
Loc3	80.447°	7.169°	1200	2	225	0

7.4 Reference

[*] Department Geology, Faculty of Science, University of Peradeniya, Sri Lanka collaborative field survey with National building research organization (NBRO), Sri Lanka and Japan International Cooperation Agency (JICA), Sri Lanka.

Chapter 8 Conclusions

The environmental monitoring by GB-SAR is relatively new and fast developing field due to a number of reasons. Most of the existing research work mainly focus on the estimation of sub-millimeter level displacement of both natural as well as manmade structures which is practically difficult to achieve. Since the overall GB-SAR operating, monitoring steps done by the human insolvent, the complete monitoring process can be improved by systematically. The main goal of this research work is to incorporate those relevant methodologies to enhance the existing GB-SAR monitoring process. In this thesis, we proposed and practically used new methodologies for; feasibility survey in Chapter 3; Atmospheric phase screen removal method in Chapter 4 and CS estimation method in Chapter 5. Furthermore, we had been developed most efficient and landslide monitoring system and early warning system. The following are the summary and conclusions of the each chapter.

Chapter 2 describe the principal of the GB-SAR system and its operation methods and signal processing. The fully polarimetric calibration was done and complete signal processing results were presented in each processing step. The cross calibration coefficients were estimated and validated. These results were used for GB-SAR signal processing in discuss in Chapters.

Chapter 3 proposed 3D GIS model assisted survey in order to find the best location for GB-SAR installation and estimate the best GB-SAR configuration prior to site installation. The new software tools were designed in order to estimate optimum radar illumination. The developed technique was successfully used for feasibility survey in large scale landslide location in Minami-Aso, Kumamoto. The simulation result shows the expected illumination from different installation location in the designed 3D model. This becomes more convenient not only for electrical engineers, but also for people who work in cross-platforms subject area such as construction, civil engineering, geology, environmental science..etc. Further, it can improve the efficiency of the total GB-SAR monitoring process by saving system calibration time and cost. The software tools were validated by real GB-SAR monitoring result. This tools can further improve by adding received back scattering power wrt to the roughness of the monitoring surface.

Chapter 4 proposed new Atmospheric phase compensation algorithm (TSSA) for DInSAR. In this chapter, atmospheric phase problem, especially observed in montantainous sites was discuss by addressing real experimental site in Minami-Aso, Kumamoto. The results of conventional atmospheric removal method was shown and erroneous estimation was discuss by the theoretical explanation. By considering the spatial ergodicity of CS points, the TSSA algorithm was proposed. It can used for extreme weather conditions in mountatanous area as well as normal weather condition. Since this

proposed atmospheric phase compensation method based on a statistical model, it can be used in the field experiment in GB-SAR, without practically measuring any meteorological parameters such as atmospheric pressure, atmospheric temperature or humidity. The proposed method has been successfully used for real time landslide early warning station since January 2017 to date.

Chapter 5 proposed new method for CS estimation for fully polarimetric GB-SAR experiment. The conventional CD estimation method was discuss and problem of CS estimation by limited number of data acquisition was highlighted. Moreover, due to the long range observation of reflected GB-SAR signal make instability in amplitude component of the existing method, so it is not sensitive for very stable scatters such as trihedral corner reflected. The proposed method estimate both amplitude and phase stability of the reflected signal by estimating the eigenvalue and eigenvector. Therefore it shows the better result in CS estimation and method can be used to extract the PS pixels in a complicated urban environment such as construction site which highly correlated with random movements of man and unmanned vehicle and equipment with in short period of time.

Chapter 6 landslide monitoring of interferometric GB-SAR was presented. The method discuss in Chapter 3, Chapter 4 and Chapter 6 was utilized. Meantime, a more realistic method was used to decide optimum data acquisition interval for particular GB-SAR monitoring campaign, based on complex coherence coefficient. It was practically applied for real time landslide monitoring site in Minami-Aso and show reliable results for displacement measurement. The new landslide early warning system was design and complete operational flow chart was discuss. This system can further develop to estimate the landslide moving direction and moving speed.

Chapter 7 summarized background and the future plane of the establishment of landslide monitoring station in Sri Lanka. Due to the tropical weather and geomorphology of the country, landslide problem becomes a major issue in the country. Since the existing landslide hazard monitoring system based on pinpoint measurement, requirement of more practical remote sensing method need to be established. The model survey results was presented and need to be discuss further.

GB-SAR has a great potential for render real time and reliable information of submillimeter level displacement in the 2D plain which no other sensor can obtain so far. Currently, the interferometric GB-SAR is utilized for the real time monitoring of the open pit mining and landslide monitoring. This system proposed as a safety tool in future for a large scale construction site. By different operation modes, a system also deployed as quality estimation tool by vibration monitoring, structural health estimation so on. Prior to those field deployments, Estimation of incident angle, incident power, can be optimized by computer simulation model in future. Furthermore, there is not many research work based on fully polarimetric GB-SAR sensor. Fully polarimetric radar signal can use to estimate soil condition such as soil moisture. This would be very interesting research area in future to predict most probable area to trigged land slide within the range illumination

Appendix

Introduction

This appendix addresses result of feasibility survey conducted for GB-SAR installation in bridge construction site. As mention in Chapter 3, the Kumamoto earthquake destroys the Aso-Ohahi Bridge. The new bridge construction work was started in May 2017. The new bridge was proposed 300m south to the old bridge. This location was in the margin area of fault-zone so that the stability information of the area near to the foot of the bridge was highly prioritized. The GB-SAR was proposed as a most appropriate remote sensing technique for stability estimation. We have conducted the feasibility study to find the most appropriate location for GB-SAR installation and optimum GB-SAR configuration.

Results
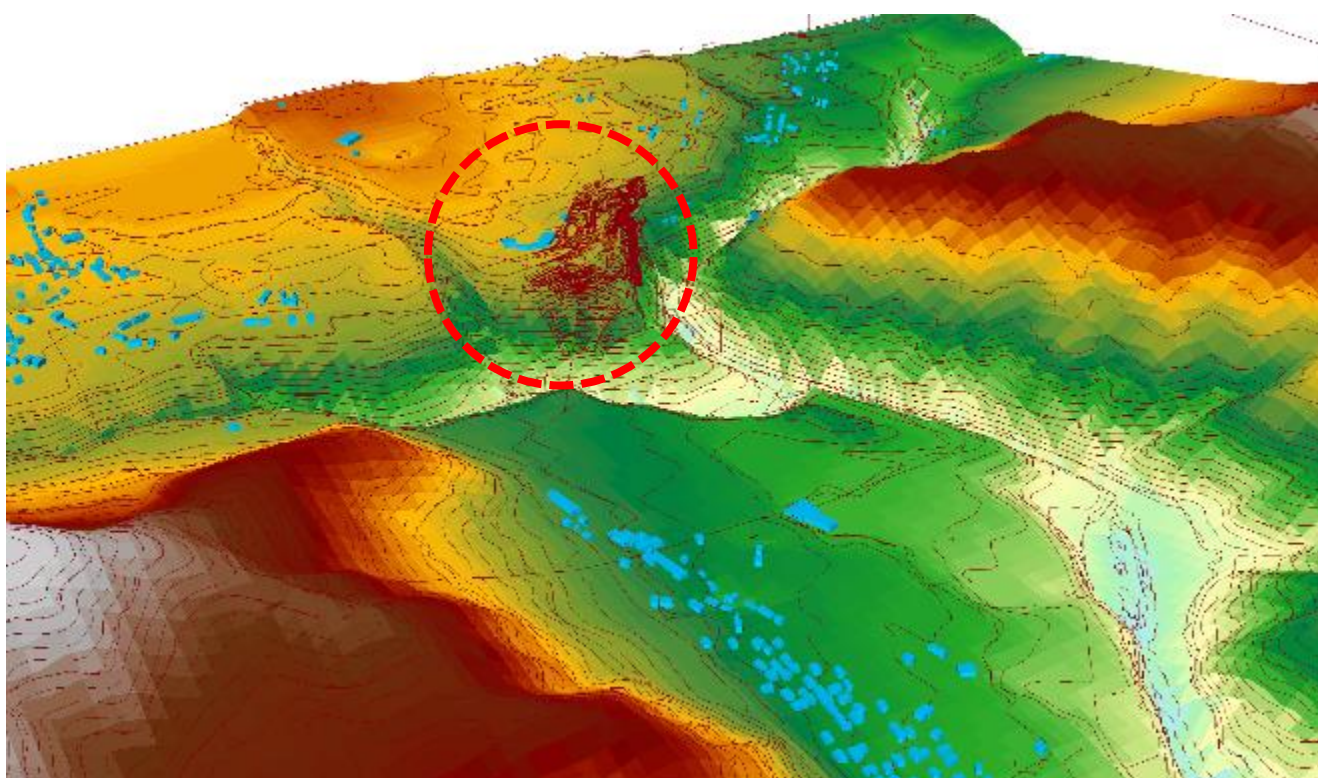
Figure A.1   3D model design for the new bridge construction site
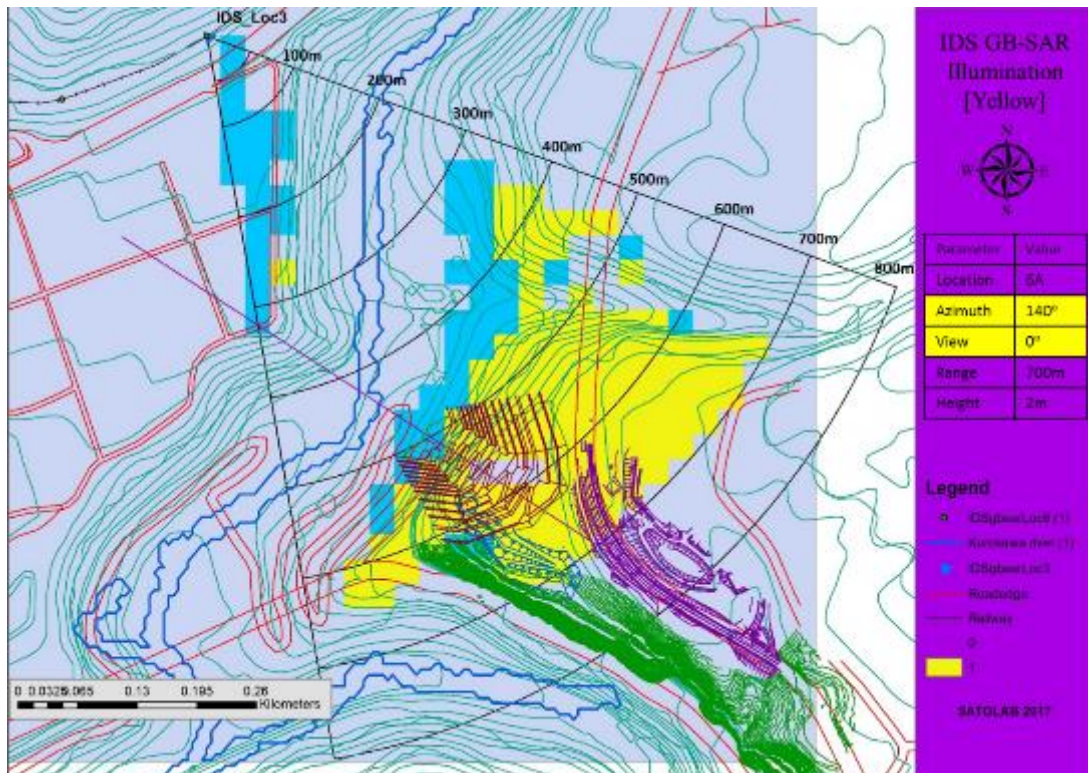
Figure A.2   Proposed GB-SAR configuration 1
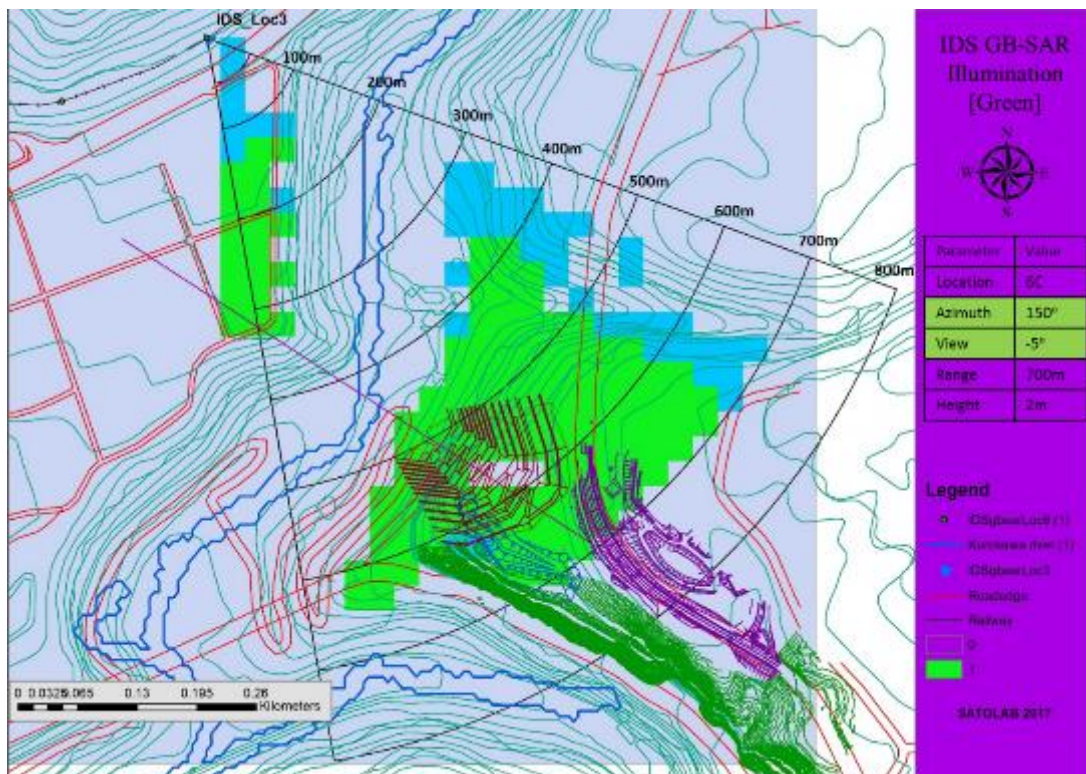
Figure A.3   Proposed GB-SAR configuration 2

Publications and Awards

Journals Papers

[1] A. Karunathilake and M. Sato, "Atmospheric phase compensation in extreme weather condition for Ground-Based SAR," IEEE Geoscience and remote sensing 2017 (on processing) from (Chap 4)

[2] A. Karunathilake and M. Sato, "Eigen vector based model for persistent scatter estimation in time variant surfaces using fully polarimetric GB-SAR (on processing) from (Chap 5)

[3] A. Karunathilake, L. Zou, K. Kikuta, M. Nishimoto and M. Sato, "An implementation and configuration of GB-SAR for landslide monitoring in sub-urban environment, Case study: Minami-Aso, Kumamoto," SEGJ (on processing) from (Chap 3 and   Chap 6)

Conference Papers

[1] A. Karunathilake and M. Sato, "3D Model assisted survey to design and estimate ground based SAR illumination," in 第42回リモートセンシングシンポジウム., Chiba. 2017, pp. 35-38.

[2] M. Sato, A. Karunathilake and J. Gunathilake, "Radar technology against natural disasters and manmade hazards," in Science council of Asia annual meeting 2016., Colombo, Srilanka, pp. 202.

[3] A. Karunathilake, C. Koyama and M. Sato, "The effect of the polarization rotation angle in understanding polarimetric SAR data for land cover classification," 電子情報通信学会(IEICE), 2015年電子情報通信学会 ソサイエティ大会, 9月8日（火）〜11日（金）, 東北大学　川内北キャンパス（仙台市）.

Award and Scholarship

- IEEE Geoscience and remote sensing – Japan Chapter, **"Young Researcher Award 2017"**.

- Japan student service organization (JASSO) Honor Scholarship for Post Graduate Studies, Scholarship (10/2014–04/2015)

- Japanese Government Scholarship MEXT (Monbukagakusho) Super global university (SGU) Scholarship (04/2015–04/2016)

- Japanese Government Scholarship MEXT (Monbukagakusho) Super global university (SGU) Scholarship (04/2016–04/2017)

- Japanese Government Scholarship MEXT (Monbukagakusho) Super global university (SGU) Scholarship (04/2017–09/2017)

Acknowledgement

I would like to express my deep gratitude to my supervisor, Prof. Dr. Motoyuki Sato, for accepting me as a doctoral student in his laboratory and give me a chance to learn about radar from very basic level to more advanced systems. Also, I greatly appreciate his infinite enthusiasm on research and education inspired me during the past three years. "Try to find your own way to solve the problem !" these words change my entire mind to investigate and deeply understand any problem and find the appropriate solution using existing resources. Also, the core value of Sato laboratory on academic work always motivates me to be more creative and pushes me with a moderate feeling of tension in daily life. Meantime, I am very grateful for not only his instruction on research but also his concern for my life in Japan as an international student, especially by recommend me for MEXT scholarship in each academic year, it helps me to strictly focus my mind only to the everyday laboratory research work during the period of stay. Also, I greatly appreciate for providing me many precious chances to participate in many collaborative research activities in GB-SAR as well as GPR all over the Japan and exchange professional knowledge and experience to improve my future career.

I would like to thank my dissertation committee, Prof. Dr. Hiroshi Takahashi with Graduate School of Environmental Studies, Prof. Dr. Shunichi Koshimura with International Research Institute of Disaster Science and Prof. Dr. Masahiko Nishimoto with Computer Science and Electrical Engineering, Graduate School of Science and Technology with Kumamoto University, for their constructive suggestions and comments.

I am also deeply indebted to Prof. Magaly Koch with Boston University, USA, for her kind advice and instructive discussions during her stay at Tohoku University as a visiting professor. It helps me to combine my early academic knowledge and ideas in the field of radar remote sensing. Also I would like to thank Prof. Giovanni Nico with Consiglio Nazionale delle Ricerche (CNR), Istituto per le Applicazioni del Calcolo (IAC), Bari, Italy for shear his advanced problem solving method, skills and signal processing techniques, strong academic advice and patient guidance by daily discussions, during his stay at Tohoku University as a visiting professor.

During my attendances in presentations at conferences and workshops, I also got many encouragements and valuable suggestions. Here I should express my special thanks to Prof. Yoshio Yamaguchi with Niigata University, had many personal discussions which greatly extended my knowledge on related topics, Dr. Simone Atzori, National Institute of Geophysics and Volcanology, National Earthquake Centre, Rome, Lazio, Italy for appreciation and suggestion which greatly extended my knowledge on related topics.

<div align="right">
Amila Thilanka Karunathilake

August 2017, in Sendai
</div>